5-1-2012

Chemical Weathering of the Mafic Minerals Serpentine and Olivine in Natural Environments

Julie Lynn Baumeister
University of Nevada, Las Vegas, jbaumeister1217@gmail.com

CHEMICAL WEATHERING OF THE MAFIC MINERALS SERPENTINE AND OLIVINE IN NATURAL ENVIRONMENTS

by

Julie L. Baumeister

Bachelor of Arts
University of Minnesota, Morris
2009

A thesis submitted in partial fulfillment
of the requirements for the

Master of Science in Geoscience

Department of Geoscience
College of Science
The Graduate College

University of Nevada, Las Vegas
May 2012

THE GRADUATE COLLEGE

We recommend the thesis prepared under our supervision by

Julie L. Baumeister

entitled

Chemical Weathering of the Mafic Minerals Serpentine and Olivine in Natural Environments

be accepted in partial fulfillment of the requirements for the degree of

Master of Science in Geoscience
Department of Geoscience

Elisabeth Hausrath, Committee Chair

Zhongbo Yu, Committee Member

Rodney V. Metcalf, Committee Member

Brian Hedlund, Graduate College Representative

Ronald Smith, Ph. D., Vice President for Research and Graduate Studies
and Dean of the Graduate College

May 2012

ABSTRACT

Chemical Weathering of the Mafic Minerals Serpentine and Olivine in Natural Environments

by

Julie L. Baumeister

Dr. Elisabeth Hausrath, Examination Committee Chair
Assistant Professor of Geoscience
University of Nevada, Las Vegas

Chemical weathering is a critical process that plays a key role in controlling the chemistry of natural waters, the cycling of atmospheric carbon dioxide, and the formation of soil. The weathering of silicate minerals is important because the Earth's crust is composed of approximately 92 weight percent silicate minerals. Despite an extensive literature on mineral dissolution and kinetics, relatively few studies have examined weathering of the mafic minerals serpentine and olivine, especially in a natural environment. The first chapter of this thesis provides an introduction to the minerals serpentine and olivine. The second chapter of this thesis examines the important factors affecting incipient weathering of serpentinite at two sites in the Klamath Mountains, California. Serpentinite rock cores and serpentinite-derived soils from each site tested positive for iron-oxidizing bacteria, and mineral dissolution in weathered samples appeared to follow the order (from first to dissolve to last): pyroxene > iron-rich serpentine > magnesium-rich serpentine > aluminum-rich serpentine. The third chapter of this thesis examines the natural dissolution of olivine in an arid environment at Black Rock Flow, Nevada. Etch pits, an apparent dissolution feature, were observed and used to measure a surface-area normalized rate of olivine dissolution (3.48×10^{-15} mol forsterite/m^2s). These findings help quantify the incipient processes affecting serpentine

soil formation and provide the first known dissolution rate for naturally-weathered olivine in an arid environment.

ACKNOWLEDGEMENTS

There are many people that I would like to thank for their help over the years I spent at UNLV. First of all, I would like to thank my advisor and committee chair, Elisabeth Hausrath, for all of her help and guidance with field work, lab work, and writing throughout the course of my master's studies. She introduced me to the field of chemical weathering studies, and helped me learn more than I ever expected about geochemistry. Thank you also to my graduate advisory committee, Rodney Metcalf, Zhongbo Yu, and Brian Hedlund, for their suggestions and encouragement.

I would like to thank the UNLV Department of Geoscience for financial help in the form of scholarships and teaching assistantships, and to the Geological Society of Nevada for a scholarship. Thank you also to the UNLV Graduate and Professional Student Association and the Geological Society of America for travel grants which have allowed me to attend conferences and present research. For allowing us access and the ability to sample in the Klamath Mountains, I want to thank the U.S. Forest Service.

For his expertise about the Klamath Mountains and for being a great guide in the field, I want to thank Rodney Metcalf again. The idea to sample at Black Rock Flow was a helpful suggestion from Eugene Smith to my advisor. Collaborators from the University of Maine, Amanda Olsen and her students, provided helpful insight and information about serpentine laboratory studies.

Many people have assisted with this project, including two wonderful students who were undergraduates at the time, Valerie Tu and Mary Evert who were able to take part in this research through NSF-EPSCoR and NSF-REU grants, respectively. Without the help of Jason Cornell, I would have been completely lost when it came to using the

rock saws. For their amazing help in running EMiL, I need to thank Sean Mulcahy, Christopher Adcock, and Minghua Ren. Many thanks go to Oliver Tschauner and Racheal Johnson for running XRD samples, and again to Racheal Johnson for her skills in prepping and running samples for XRF. Kirellos Sefein was also a great help in the Geochemistry Lab.

I had the wonderful opportunity to share an office with many people including Brittany Myers, Valerie Tu, Christopher Adcock, Seth Gainey, Amanda Williams, Mengesha Beyene, and Colin Robins. Thank you for listening to many practice presentations, for offering advice, and for just being fun people to work with. I am very thankful, also, for the support of my family. I also want to thank my fiancé, Erik Baker, for his support through the years and for help with editing. Many people have played a large part in being supportive, and to anyone I may have forgotten: thank you!

TABLE OF CONTENTS

LIST OF TABLES

LIST OF FIGURES

CHAPTER 1

INTRODUCTION

The process of chemical weathering is critical in controlling the chemistry of natural waters, global biogeochemical cycles, and soil formation. Weathering of silicates, in particular, is an important process because the Earth's crust is composed of approximately 92 weight percent silicate minerals. Many dissolution studies have focused on granitic and basaltic rocks, as reviewed in White and Brantley (2003) and Navarre-Sitchler and Brantley (2007), due to the abundance of granite in Earth's crust and due to the interactions between oceanic waters and basalt. However, within the extensive body of research on mineral dissolution and kinetics, relatively few studies have focused on characterizing mafic mineral dissolution. This is especially true when it comes to natural weathering studies of the mafic minerals serpentine and olivine under arid conditions.

The dissolution of mafic minerals is a growing area of interest due to their potential uses in the field of mineral carbonation. Carbon sequestration techniques such as mineral carbonation react carbon dioxide with calcium-, magnesium-, or iron-bearing minerals in order to form a stable carbonate mineral, which stores the carbon dioxide in an unavailable form. Carbon dioxide is consumed in significant amounts during the dissolution, or weathering, of mafic minerals (Dessert et al., 2003). Tropical ophiolites, which consist of mafic minerals such as olivine and serpentine, and volcanic rocks, for example, account for only about 1% of the Earth's surface; however, up to 15-20% of all the atmospheric carbon sequestered by silicate weathering is due to the weathering of tropical ophiolites and volcanic rocks (Shopka et al., 2011). It is because of this

disproportionate uptake of carbon through mafic mineral dissolution that ultramafic rocks have been proposed for use in industrial-scale mineral carbonation (Goff and Lackner, 1998; Kelemen and Matter, 2008), and serpentine and olivine are being explored as potential candidate minerals for such mineral carbonation methods (Guthrie et al., 2001; Carey et al., 2003; Béarat et al., 2006).

Serpentine weathering in natural environments is also of interest due to its unique chemistry which strongly impacts the surrounding biota. Soils that develop on serpentine are typically depleted in the nutrients Ca, K, and P, and contain enriched levels of Mg, Fe and trace elements such as Ni, Cr, Cd, Co, Cu, and Mn (Wildman et al., 1968; Shallari et al., 1998; Lee et al., 2001; Harris et al., 2007). Plant communities that grow on serpentine soil have developed adaptations in order to adjust to the stresses posed by the unique chemistry of the bedrock (Kruckeberg, 2004; Brady et al., 2005). While studies show the effects serpentine has on biota, few studies have investigated the role that biological impacts have on the weathering of serpentine.

The serpentine group of minerals consists of the three polymorphs lizardite, antigorite, and chrysotile. The serpentine minerals are phyllosilcates, or sheet silicates, and share the general formula $Mg_3Si_2O_5(OH)_4$. Serpentine minerals are formed through serpentinization when mafic and ultramafic rocks are hydrothermally altered in the following reaction (Wegner and Ernst, 1983)

$$2Mg_2SiO_4 + 3H_2O = Mg_3Si_2O_5(OH)_4 + Mg(OH)_2 \qquad (\textit{Equation 1.1}).$$

Serpentinite, a rock with a composition dominated by one or more of the serpentine minerals, is formed when these minerals combine. Serpentine dissolves and carbon dioxide is consumed by the reaction (Park and Fan, 2004)

$$Mg_3Si_2O_5(OH)_4 + 3CO_2 + 2H_2O \rightarrow 3MgCO_3 + 2SiO_2 + 4H_2O$$ (*Equation 1.2*).

Olivine is a nesosilicate, or orthosilcate, mineral with the general formula $(Mg,Fe)_2SiO_4$. The olivine group is a solid solution set existing between forsterite (Mg_2SiO_4) and fayalite (Fe_2SiO_4). Olivine dissolves quickly in comparison to other silicate minerals and has a relatively simple mineral structure that contains isolated silica tetrahedra (Goldich, 1938; Schott & Berner 1983; Pokrovsky & Schott, 2000). At Earth surface temperatures, olivine dissolution usually occurs stoichiometrically and few weathering products are formed. The general reaction for olivine, specifically forsterite, dissolution is

$$Mg_2SiO_4 + 4H_2CO_3 = 2Mg^{2+} + H_4SiO_4 + 4HCO_3^-$$ (*Equation 1.3*).

At higher pressures and temperatures, serpentinization of olivine can occur following the reaction in Equation 1.1. Iddingsite is another possible alteration product of olivine when it is exposed to higher temperature aqueous alteration (Velbel, 2009).

Mineral dissolution can be observed in laboratory and/or field settings. Dissolution experiments in a laboratory setting often use batch reactors or flow through columns to measure dissolution rates far from equilibrium (e.g. Olsen and Rimstidt, 2008; Rosso and Rimstidt, 2000). In the field, mineral dissolution rates can be quantified by analyzing river water chemistry in a watershed (e.g. April et al., 1986), studying weathering rinds (e.g. Sak et al., 2004), or by determining a mineral or chemical depletion profile throughout a soil column (e.g. White, 2002). However, there is generally a discrepancy of two to four orders of magnitude between rates measured in the laboratory and rates measured in the field (White and Brantley, 2003). This discrepancy is likely due to a combination of factors including, but not limited to: temperature,

mineral surface area, mineral composition, solute composition, mineral coatings, and the duration of weathering (Velbel, 1993; White and Brantley, 2003). Despite the laboratory-field discrepancy in absolute rates of mineral dissolution, relative mineral dissolution rates appear to remain constant between the field and laboratory (Velbel, 1993; Hausrath et al., 2008).

Serpentine dissolution studies performed at temperatures and pH ranges relevant to the natural environment are limited. Bales and Morgan (1985) and Hume and Rimstidt (1992) studied chrysotile dissolution in the context of health risks associated with asbestos. Antigorite dissolution at a starting pH of 4 was studied by Lin and Clemency (1981). Lizardite dissolution rates have been measured in a laboratory setting at 25°C by Luce et al. (1972), Carey et al. (2003), and Yardley (2011). A serpentine dissolution rate was measured in a natural setting using catchment hydrochemical data by Freyssinet and Farah (2000) which was orders of magnitude slower than published laboratory rates. Most studies of serpentine in a natural setting have focused on soil and secondary mineral formation (Cleaves et al., 1974; Pavich et al., 1989; Lee et al., 2003; Caillaud et al., 2004, 2006, 2009).

Olivine dissolution has been widely studied in a laboratory setting (Blum and Lasaga, 1988; Brady and Walther, 1989; Grandstaff, 1980; Grandstaff, 1986; Oelkers, 2001; Pokrovsky and Schott, 2000; Rosso and Rimstidt, 2000; Siegel and Pfannkuch, 1984; Wogelius and Walther, 1991; Wogelius and Walther, 1992) because it dissolves quickly in comparison to other silicate minerals, and has a relatively simple mineral structure. Despite the many dissolution kinetics studies on olivine in the laboratory, few studies exist that have examined olivine dissolution rates in the field (e.g. Schnoor,

1990). Chemical weathering features such as dissolution pits, or etch pits, have been thoroughly characterized on naturally-weathered olivine (Velbel and Ranck, 2008; Velbel, 2009; Nowicki and Velbel, 2011). However, these studies did not measure rates of dissolution.

The second chapter of this thesis characterizes serpentinite weathering from the unweathered parent rock to the soil surface at two sites in the Klamath Mountains of northern California. The effects of allochthonous inputs, biological influences, and chemical weathering were evaluated for their importance in the incipient weathering of serpentine in a natural environment, which is a relatively under-explored niche in the field of chemical weathering studies. Samples of both soils and rock cores from each study site tested positive for iron-oxidizing bacteria, and signs of oxidized iron were observed on weathering rinds in the soil and rock cores. In the weathered samples, mineral dissolution appears to follow a specific order (from first to dissolve to most resistant): pyroxene > iron-rich serpentine > magnesium-rich serpentine > aluminum-rich serpentine. This mineral order is likely based on mineral dissolution kinetics, possible effects of biological iron-oxidation, and cation substitutions that can act to stabilize the mineral structure.

In the third chapter of this thesis, the dissolution of olivine in a natural environment was observed at Black Rock Flow, in central Nevada. Diamond-shaped etch pits, a characteristic of chemical weathering, were observed through scanning electron microscopy on the surfaces of dunite xenoliths sampled from the basalt flow. Based on comparisons to etch pits formed on naturally-weathered olivine in humid environments (Velbel, 2009; Nowicki and Velbel, 2011), it appears as though etch pit formation in an

arid environment follows a similar process. Using an equation derived from Gordon and Brady (2002), an olivine dissolution rate was calculated using etch pit geometries and the exposure age of the weathered surface. The dissolution rate was, as predicted, several orders of magnitude slower than published laboratory rates for forsterite.

Overall, this thesis aims to characterize the natural weathering of the mafic minerals serpentine and olivine under arid conditions, an area in which few studies currently exist. Incipient weathering processes for serpentine were explored, including the potential impacts of allochthonous inputs, biological influences, and chemical weathering. Few studies have measured olivine dissolution rates in a natural environment (e.g. Schnoor, 1990), and no one, to the author's knowledge, has previously measured a dissolution rate for olivine in the field under arid conditions. In this thesis, a rate of olivine dissolution was measured in an arid climate that is within reason given the laboratory-field discrepancy, climate, and assumed pH conditions.

CHAPTER 2

CHEMICAL WEATHERING OF SERPENTINITE IN THE KLAMATH MOUNTAINS, CALIFORNIA

Introduction

The process of chemical weathering is a critical component in controlling the chemistry of natural waters, global biogeochemical cycles, and in soil formation. Many studies have measured the dissolution rates of granites and basalts, as reviewed by White and Brantley (2003) and Navarre-Sitchler and Brantley (2007), due to the abundance of granite in the crust and the interactions of basalt with the oceans. However, relatively few studies have examined weathering of ultramafic rocks, such as serpentinites.

Mafic minerals, including serpentine, are of growing interest due to the potential for their use in carbon sequestration. Serpentine is the general name for a group of three polymorph minerals, antigorite, chrysotile, and lizardite, that are formed when olivine is hydrothermally altered in the reaction

$$2Mg_2SiO_4 + 3H_2O = Mg_3Si_2O_5(OH)_4 + Mg(OH)_2 \qquad (\textit{Equation 2.1}).$$

Significant amounts of carbon dioxide are consumed during the natural weathering process, or dissolution, of mafic minerals (Dessert et al., 2003). Shopka et al. (2011) estimates that up to 15-20% of all the atmospheric carbon sequestered by silicate weathering is due to the weathering of tropical ophiolites, which consist of mafic minerals such as olivine and serpentine, and volcanic rocks. This value is significant because tropical ophiolites and volcanics only make up about 1% of Earth's surface, which suggests a disproportionate uptake of carbon through ultramafic rock dissolution. Due to this consumption of carbon dioxide, ultramafic rocks have been proposed for use

in industrial-scale carbon sequestration and mineral carbonation (Goff and Lackner, 1998; Kelemen and Matter, 2008). Mineral carbonation is a carbon sequestration method in which carbon dioxide is reacted with minerals containing calcium, magnesium, or iron to form stable carbonate minerals, thereby storing the carbon dioxide in an unavailable form. Attempts to determine a viable method for mineral carbonation are currently being tested on basalts (Oelkers et al., 2008; Gudbrandsson et al., 2011), serpentine (Guthrie et al., 2001; Carey et al., 2003), and serpentinite (Teir et al., 2007a; Orlando et al., 2011).

In addition to potential mineral carbonation, further characterization of serpentinite weathering may prove useful in the study of landslide hazard assessment. In the Klamath Mountains, large landslides were found to be more common in areas of serpentinite terrain compared to areas of peridotite terrain (Alexander and DuShey, 2011). Peridotite undergoes a 33% expansion during serpentinization as well as fracturing and shearing. The shearing causes a reduction in the shear strength of serpentinite, which makes it more prone to mass failure (Alexander and DuShey, 2011).

Serpentinite-derived soils are also of interest due to the impact that their unusual chemistry has on the surrounding biota. Serpentinite-derived soils are typically depleted in essential nutrients such as Ca, K, and P and contain high levels of Mg, Fe and trace elements such as Ni, Cr, Cd, Co, Cu, and Mn (Wildman et al., 1968; Shallari et al., 1998; Lee et al., 2001; Harris et al., 2007). According to Jenny (1980), plant communities over serpentine bedrock have developed "serpentine syndrome," which allows them to adapt to the stresses associated with serpentine soils. Examples of such adaptations include plants with reduced stature, increased tolerances to elevated Mg and Ni, and more developed root systems compared to closely related plants species not on serpentine soils

(Kruckeberg, 2004; Brady et al., 2005). While these serpentinite-derived soils strongly affect the surrounding organisms, biota can also impact mineral weathering. Such impacts can include iron oxidation and release of organic compounds, but few studies have examined biological impacts on serpentinite weathering (Daghino et al., 2006, 2008, 2009).

The impact of parent material (e.g. serpentinite) on the characteristics of the soils that form upon them is most important in young soils. Therefore, young soils represent the best environment to examine the interrelationships between serpentine soils and the unusual biota that grow on them, as well as the incipient weathering processes converting serpentinite rock to soil. Particularly important in the formation of serpentine soils may be the first dissolution reactions that increase porosity in the parent rock, and therefore allow additional weathering to occur within the parent rock. This first mineral to dissolve within the rock has been termed the "profile-controlling mineral" (Brantley and White, 2009), and therefore, even if present in small concentrations, may play a critical role in future soil formation. However, few studies have examined incipient field weathering of serpentinite rocks, or attempted to quantify the initial processes controlling soil formation.

Previous studies of serpentine weathering have focused on laboratory dissolution of chrysotile and antigorite. Bales and Morgan (1985) performed batch experiments at 25°C dissolving chrysotile from pH 7 to 10. Antigorite dissolution was studied by Lin and Clemency (1981) in batch experiments at 25°C with a starting pH of 4. Lizardite dissolution rates were measured by Luce et al. (1972) over a range of pH from 1.5 to 9.6 at 25°C (Figure 2.1). Yardley (2011) measured lizardite dissolution rates at 25°C over a

pH range from 3 to 6 (Figure 2.1). Freyssinet and Farah (2000) measured a serpentine dissolution rate using hydrochemical data from a catchment in French Guiana that is orders of magnitude slower than laboratory serpentine dissolution rates (Freyssinet and Farah, 2000; Figure 2.1).

Field studies of serpentine weathering generally, however, have focused on soil and secondary mineral formation, with little emphasis on the initial reactions affecting incipient soil formation. Pavich et al. (1989) studied soil cores of serpentinite regolith in Virginia and documented a thin soil and thin massive subsoil overlying weathered serpentinite with no saprolite present. Cleaves et al. (1974) also noted shallow depths to the serpentinite bedrock (typically < 1 m) and a lack of saprolite and secondary minerals overlying serpentinite in Maryland. The lack of secondary minerals was attributed to low concentrations of aluminum available in the bedrock with which to form clay minerals (Cleaves et al., 1974). In contrast, other studies have noted the formation of secondary minerals during serpentinite weathering. Serpentine minerals have been shown to alter to smectites (Lee et al., 2003) including saponite, Fe-rich montmorillonite, and nontronite (Caillaud et al., 2006). Chlorite and magnetite can also be present as accessory minerals in the serpentinite bedrock (Lee et al., 2003; Caillaud et al., 2004, 2006, 2009). Chlorite has been observed to alter to vermiculite and interlayered chlorite and vermiculite (Lee et al., 2003) and magnetite can alter to maghemite, goethite, and hematite (Caillaud et al., 2004, 2006). Although early iron-staining has been documented (Caillaud et al., 2006, 2009), none of these studies have explicitly tried to determine the first reactions controlling the formation of soils on serpentinite.

This study, therefore, aims to determine the important factors affecting incipient serpentinite weathering at two field sites in the Klamath Mountains of northern California. More specifically, the effects of allochthonous inputs, such as dust and past glacial deposits, biological influences, and chemical weathering are examined for their importance in affecting incipient soil formation. To assess the importance of these three factors, serpentinite weathering was examined from the unweathered parent rock to the soil surface. These results will help to better understand the first reactions by which serpentinite rock becomes serpentine soil, which is important in order to obtain a better understanding of these extreme soils.

Geologic Setting

The Klamath Mountains in northern California are an ideal locale in which to study serpentinite weathering because they contain the largest exposed ultramafic body in North America (Irwin, 1966). The Trinity ultramafic body of the Klamath Mountains covers roughly 2000 km^2 and is comprised of peridotite, gabbro, and diabase (Alexander et al., 2007). The Trinity peridotite is composed of partially serpentinized harzburgite (olivine + orthopyroxene), lherzolite (olivine + clinopyroxene + orthopyroxene), and dunite (>90% olivine) (Alexander et al., 2007). Harzburgite and lherzolite make up roughly 60-70% of the Trinity peridotite (Quick, 1981). Dunite and plagioclase lherzolite account for 15-20% and 10-15%, respectively, and clinopyroxene-rich dikes account for 1-2% (Quick, 1981). Based on radiometric dating, the Trinity peridotite is thought to have crystallized during the Ordovician (Peacock, 1987).

The Trinity Alps experienced three periods of Wisconsin glaciation (Sharp, 1960). The approximate date of the most recent deglaciation provides a constraint on the amount of time the serpentinite has been exposed to weathering. Pollen records and radiocarbon dates from a sediment core from Mumbo Lake, in the Trinity Mountains, indicate a switch from a cold and dry climate to a cool and moist climate ~12,100 years before present (Daniels et al., 2005). The lowest terminal elevation reached by glaciers was 3350 ft during the late-Wisconsin glaciation (Sharp, 1960). Sharp (1960) also observed evidence for more recent glaciation in the Trinity Alps. This neoglaciation, or post-Hypsithermal glaciation, produced glaciers with a minimum terminal elevation of 6800 ft (Sharp, 1960). This study, therefore, assumes that elevations between ~3350 ft and ~6800 ft have been exposed to weathering for approximately 12,100 years. Because these soils are relatively young, it should be possible to analyze the incipient processes acting on soil formation, which could be difficult to discern in older soils.

In present day, the Klamath Mountains region can be described as having a Mediterranean climate; however, it is locally variable due to the effects of elevation gradients and the orographic effect (Skinner et al., 2006). More specifically, the Trinity locality receives 50-175 cm of mean annual precipitation, much of which is snow (Alexander et al., 2007). The frost-free period for this region is less than 25 days per year for higher elevations and over 100 days per year for lower elevations (Alexander et al., 2007). The temperate climate, as well as the short duration since deglaciation, facilitates examination of incipient weathering.

Methods

Sample Collection and Preparation

Sampling sites were chosen based on parent rock, elevation, and landscape. Two sites, which will be referred to as Scorpion Creek and Kangaroo Lake, containing serpentinite-derived soils within the Trinity ultramafic body were selected. Both sites are located at elevations between 4500 ft and 6000 ft. This elevation interval was chosen to ensure that sites were glaciated ~12,100 years before present (Sharp, 1960; Daniels et al., 2005), thus providing a constraint on weathering time. Both sites are located on ridgetops or relatively flat areas in order to avoid effects from downslope migration of soil material.

The first sampling locality, Scorpion Creek, is located east of Highway 3 on Forest Road 38N85 at lat. 41°05'08" N and long. 122°39'54" W (Figure 2.2). The serpentinite outcrop is visible from the road, and the samples were collected from a meadow-like area above the outcrop. The second sampling locality, Kangaroo Lake, is located north of Kangaroo Lake Campground on Forest Road 40N18 at lat. 41°21'08" N and long. 122°38'00" W (Figure 2.2). A short uphill hike to the south of the road was needed to reach the outcrop. Samples were collected roughly five feet away from the nearest trees and outcrops.

Soil pits were dug at the Scorpion Creek and Kangaroo Lake sites to the point of refusal, depths of 40 cm and 56 cm, respectively (Figure 2.3). Soil samples were collected at depth intervals of 10 cm and placed into sterile plastic bags and stored in a cooler with ice for the duration of field work. Careful measures were taken to avoid contamination by cleaning the spatulas used for sampling with ethanol between each

sampling interval. Back at the lab, samples were stored at 4°C until analysis was completed.

In the same locations, rock core samples were collected to depths of 76 cm and 135 cm at Scorpion Creek and Kangaroo Lake, respectively, using a 1" handheld drill (Shaw Backpack Drill; Figure 2.4). Rock core samples were placed into sterile plastic bags and stored in a cooler with ice. In the lab, samples were rinsed with filter-sterilized deionized water in a 75 µm sieve to remove rock powdered during drilling and air-dried overnight then stored in sterile plastic bags at 4°C until analysis was completed.

Soil Characteristics

Soil color, field wet and dried, were determined using a Munsell color chart. Soil texture was determined using the texture-by-feel method (Brady and Weil, 2002). Field wet soil samples from each soil sampling depth were weighed, and then oven-dried at 50°C for 48 hours. After drying, samples were re-weighed. Water content, in kg water per kg dry soil, was calculated as the wet weight minus the dry weight, divided by the dry weight. Soil bulk density samples were collected in the field using a bulk density sampler (Soil Moisture Sampler, Soil Moisture Equipment). Field wet soil samples collected with the bulk density sampler were weighed, oven-dried at 50°C for 48 to 70 hours until dry and then re-weighed. Bulk density was calculated by dividing the dry weight of the sample by the volume of the sampler (229 cm^3). Bulk density of the rock cores obtained with the backpack drill was obtained by weighing the rock core and determining volume by water displacement (Jin et al., 2010), and dividing the weight of the rock core by the volume of the rock core. The pH of the soil pore waters was

determined by adding 2 ml of deionized water to 1 g of soil, and then the slurry pH was measured with a pH probe (Brady and Weil, 2002).

Scanning Electron Microscopy

Soils from both sites contained abundant rock fragments. A weathered rock fragment from each depth interval was embedded in epoxy, cut, and polished to allow for a cross-sectional view of the weathered surface of the rock. Similarly, pieces of rock cores collected from each site were vacuum-impregnated in epoxy, cut, and polished. While preparing these samples, reddish staining was observed on the edges of rock fragments both from the soils and from rock cores. In order to protect potentially fragile secondary minerals, samples of soil rock fragments and rock cores were sent to Spectrum Petrographics Inc. (Vancouver, WA) where they were prepared as surface-impregnated thin sections with a water-sensitive polish. All samples were then carbon-coated and analyzed using scanning electron microscopy (SEM) in backscatter mode to assess composition, and energy dispersive spectroscopy (EDS) was used to measure chemical composition at the UNLV Electron Microanalysis and Imaging Laboratory (EMiL) using a JEOL scanning electron microscope model JSM-5610.

Soil Particle Size Separation

In order to determine the effects of dust input on incipient soil formation, the silt- and clay-sized fractions, 63-2 μm and < 2 μm, respectively, for soil samples were separated using a method similar to Stemmer et al. (1998). First, 100 ml of deionized water was added to approximately 35 g of soil in a beaker. Samples were then dispersed

ultrasonically using a Branson Ultrasonic Cleaner (Model 2510) for 15-20 minutes. Rock fragments and sand-sized particles were removed by wet sieving through 2-mm and 63-μm sieves.

The remaining slurry containing the < 63 μm fraction was poured into 50-ml centrifuge tubes and centrifuged at 150 g for 2 minutes. Pellets containing the silt fraction (63-2 μm) were re-suspended and combined. The supernatants containing the clay fraction (< 2 μm) were collected. This process of centrifuging and combining was repeated three times, following Stemmer et al. (1998), in order to remove more clay-sized particles from the silt fraction. The pellet containing the silt fraction was then air-dried and re-weighed. Percent silt fraction of the soil was calculated by dividing weight of the dried silt-sized fraction by the total weight of the dry soil, as calculated from measured water content values. The supernatants remaining after removal of the silt fraction were then centrifuged once at 9860 rpm (12,500 g) for 3 minutes to obtain the clay-sized fraction. The pellet containing the clay fraction was air-dried and re-weighed. Percent clay fraction of the soil was calculated in the same manner as that of the silt fraction.

X-Ray Diffraction and X-Ray Fluorescence

Minerals in the soil samples, both bulk and separate size fractions, and rock cores were identified using X-ray diffraction (XRD) on a PANalytical X'PERT Pro X-ray diffraction spectrometer at the UNLV Geoscience XRD Laboratory. Dried soil samples were powdered using an agate mortar and pestle. Rock core samples were crushed and then powdered by first using a diamondite mortar and pestle followed by an agate mortar and pestle. Random powder mounts were analyzed for bulk mineralogy of the bulk soil,

silt- and clay-sized fractions of soil, and rock core samples using Cu $K\alpha_{1,2}$ radiation operated at 45 kV and 40 mA current over the range of 5-75° 2θ.

Bulk chemistry of major elements (Si, Al, Ti, Fe, Mg, Na, K, Mn, Ca, P, as well as LOI) and trace elements (Sc, V, Ni, Cu, Ga, Rb, Sr, Y, Zr, Nb, Ba, La, Hf, Pb, Th, and U) of the soil samples and rock cores was determined using X-ray fluorescence (XRF) at the UNLV Geoscience XRF Laboratory on a PANalytical Axios Advanced sequential X-ray fluorescence spectrometer.

Biological Activity Reaction Tests

In order to test for the presence of iron-oxidizing bacteria in the weathering profile, soil samples were analyzed using biological activity reaction tests (BARTs™, Droycon Bioconcepts Inc., Regina, SK, Canada) in the same manner as Buss et al. (2005). The iron-related bacteria tester (IRB-BART™) contains a nutrient pellet at the base of the tube, and a floating ball near the top of the tube. This floating ball slows oxygen diffusion from the headspace down into the solution, thus creating oxygen gradients where aerobic growth can occur near the top and anaerobic growth can occur near the bottom of the tube (Droycon Bioconcepts Inc., 2004). To prepare the soil samples for analysis in the BART™, 0.5 g of soil from each sampling depth was added to a sterile centrifuge tube containing 15 ml of filtered (0.2 μm filter) phosphate-buffered saline solution (0.05 M Na_2HPO_4, 0.85% NaCl; pH was adjusted using ultrapure HNO_3 to within 0.03 pH units of the average soil pH of 6.85). Samples were capped and shaken to homogenize the slurry, and then added to the IRB-BART™ testers. Rock core samples were similarly tested by adding approximately 0.5 g of rock fragments in each tester.

The testers were stored in a dark cabinet at room temperature for 10 days, and were observed and photographed once per day. After 10 days, the frequency of observation decreased to weekly, bi-weekly, and then monthly. Three control testers were prepared containing only phosphate-buffered saline and duplicate testers were prepared for the deepest sample from each site to determine if results were reproducible.

Pore Water Extraction

Pore waters were extracted from the soil samples at each site in order to test for the presence of siderophores and organic content. The pore water samples were prepared similarly to Hausrath et al. (2011) by adding 10 ml of deionized water to 30 g of field wet soil (water and soil amounts were halved if there was not enough sample available). Samples were equilibrated at ~4°C for approximately 48 hours, and centrifuged at 4500 rpm at 5°C until supernatants were clear (35-160 minutes). The pore waters were then decanted, syringe filtered (0.2 μm), and frozen in sterile centrifuge tubes until siderophore and organic analyses were performed.

Siderophores

A chrome azurol S (CAS) assay solution was prepared according to the methods of Schwyn & Neilands (1987). In a cuvette, 0.5 ml of soil pore water was mixed with 0.5 ml of CAS assay solution. If siderophores are present the siderophore will complex the iron and CAS dye is released. As a result of this reaction, the solution will undergo a color change from blue to orange. The absorbance of each sample was then measured at 630 nm on a Thermo Scientific Genesys 10S UV-Vis spectrophotometer at 2-hour

intervals for 6 hours. Absorbance was measured for known concentrations of a commercially available siderophore, deferoxamine mesylate (DFAM; VWR, Calbiochem), in order to make a standard curve for comparison to absorbance of the pore waters. Siderophore standards were made for the following concentrations of DFAM: 0, 1, 5, 10, 15, and 20 µM.

Organic Constituents

The presence of organic constituents in the soil pore waters was tested using methods similar to that of American Public Health Association (1998), Strauss and Lamberti (2002), and Weishaar et al. (2003). This method cannot confirm concentrations of specific organic acids, but is used rather to estimate the presence of UV-absorbing organic constituents, or aromaticity of dissolved organic matter. Ultraviolet absorbance of the pore water samples were measured at 253.7 nm on a Thermo Scientific Genesys 10S UV-Vis spectrophotometer.

Results

Soil Characteristics

The field wet Scorpion Creek soil was dark yellowish brown (10 YR 3/4) to very dark gray (10 YR 3/1). The field wet Kangaroo Lake soil was dark brown (7.5 YR 3/4) to very dark brown (7.5 YR 2.5/2). The top-most Scorpion Creek sample had a loamy sand texture, but deeper samples were too rocky to describe a texture. The Kangaroo Lake soil had a loamy sand texture at the top of the profile and a clay loam texture towards the bottom (Table 2.1). At Scorpion Creek, water content decreased with depth

(Figure 2.5; Table 2.1). At the Kangaroo Lake site, water content markedly decreased from the surface to the second interval, but then gradually increased with depth to the bottom of the profile (Figure 2.5; Table 2.1). Bulk density of the three soil samples ranged from 0.65 to 1.16 g/cm^3, and the average soil bulk density for the Scorpion Creek and Kangaroo Lake sites is 0.96 g/cm^3 (Figure 2.6; Table 2.2). Bulk density of the 21 rock cores ranged from 2.34 to 3.86 g/cm^3, and the average rock core bulk density is 2.67 g/cm^3 (Figure 2.6; Table 2.3). The pH of the soil pore waters are near neutral ranging from 5.81 to 7.34 (Table 2.1), and the average pH of all of the soil samples is 6.85. The most acidic sample at each sampling site was the top-most sample (Figure 2.7). Both the Scorpion Creek and Kangaroo Lake could be described as rocky soils (Figure 2.3). Roots from surrounding vegetation were also abundant in both soils, though they were more prevalent at Kangaroo Lake (Figure 2.3).

Scanning Electron Microscopy

According to EDS analysis of the Scorpion Creek samples (Appendix A), the dominant parent mineral composition is serpentine, with iron- and chromium-bearing oxides as accessory minerals (Figure 2.8a). Rock fragments from the Scorpion Creek soil as well as rock core samples displayed two characteristic edges: 1) unweathered and 2) physically weathered. Backscattered electron (BSE) micrographs of rock fragments within the Scorpion Creek soil and rock cores show minimal signs of chemical alteration of the serpentine from the interior to the surface of the samples (Figure 2.9). The mesh of particles accumulated on the surface of the rock fragments from the soil is most likely soil accumulated on the surface rather than alteration, because the rock fragments from

the soil were not rinsed prior to observation (Figure 2.9). Such surface accumulation is not observed on the surfaces of the rock core samples, which were rinsed prior to observation. Cracking and apparent disaggregation were observed on the surfaces of rock fragments from the soil and rock cores (Figure 2.10), however it is not an extensive feature.

The Kangaroo Lake samples, according to EDS analysis (Appendix A), are composed mainly of serpentine with accessory orthopyroxene and iron- and chrome-bearing oxides (Figure 2.8b). The soil rock fragments and rock cores from Kangaroo Lake displayed three characteristic dissolution features occurring from deepest within the sample to closest to the surface as follows: 1) pyroxene dissolution, 2) dissolution of iron-rich serpentine, and 3) dissolution/fracturing along edges. The order of dissolution was determined based on the amount of apparent dissolution, or void space, and how far the apparent chemical weathering front had penetrated the cross section of the rock. BSE micrographs of rock fragments both from the soil profile and rock cores contain orthopyroxene surrounded by serpentine, in which the orthopyroxene appears to have been partially dissolved out of the sample (Figure 2.11). BSE micrographs of rock core fragments also show what appears to be preferential dissolution of veins of iron-rich serpentine (Figure 2.12). Lastly, dissolution or fracturing of the serpentine near the edges of the sample was observed in both the rock fragments from the soil profile and rock cores (Figure 2.13).

Soil Particle Size Separation

At Scorpion Creek, both the percent of silt- and clay-sized fractions from the soils collected decreased with increasing depth (Figures 2.14 and 2.15; Table 2.4). At Kangaroo Lake, the percent of silt-sized fraction increased slightly and then continued to decrease with increasing depth (Figure 2.14; Table 2.4). The percent clay-sized fraction, however, from Kangaroo Lake showed a steady increase with increasing depth (Figure 2.15; Table 2.4). Overall, the soils collected from Kangaroo Lake contained a higher percent of silt- and clay-sized particles compared to those from Scorpion Creek. The percent clay fraction values appear to be consistent with soil texture results from the texture-by-feel method (Tables 2.1 and 2.4).

X-Ray Diffraction and X-Ray Fluorescence

X-ray diffractograms of the Scorpion Creek bulk soil samples indicate that lizardite, magnetite, and clinochlore are present at each depth interval (Table 2.5). Quartz was identified in the top-most Scorpion Creek soil sample (0-10 cm). The silt-sized fraction of Scorpion Creek soil contains lizardite, magnetite, clinochlore, and quartz; however, quartz was not present in the deepest sample (Table 2.5). The clay-sized fraction of Scorpion Creek soil contains lizardite and clinochlore; quartz was only present in the top-most sample (Table 2.5). Lizardite and magnetite were identified in the Scorpion Creek rock cores in all four samples that were run over the depth interval of 30-76 cm (Table 2.5). Clinochlore is also present in each of those rock core samples, except for the 47-57 cm interval.

The X-ray diffractograms of the Kangaroo Lake bulk soil samples indicate that lizardite, clinochlore, tremolite, talc, plagioclase, and quartz are present at each depth

interval (Table 2.5). Magnetite was also observed in the deepest Kangaroo Lake soil interval (below 41 cm). The silt-sized fraction of Kangaroo Lake soil contains lizardite, clinochlore, tremolite, talc, plagioclase, and quartz; however, quartz was not present in the deepest sample (Table 2.5). The clay-sized fraction of Kangaroo Lake soil contains lizardite, clinochlore, tremolite, talc, and quartz (Table 2.5). The Kangaroo Lake rock cores contain lizardite in all four samples that were run over the depth interval of 27-153 cm (Table 2.5). Clinochlore was also identified in two of the rock core samples (20-27 cm and 57-66 cm). Metal oxides were identified in the 20-27 cm interval. The 86-109 cm interval contains brucite, and tremolite was identified in the deepest rock core (122-135 cm).

The dominant parent mineral at both Scorpion Creek and Kangaroo Lake appears to be lizardite rather than antigorite. This was determined based on Peacock (1987), which provides detailed characteristics of XRD peaks for lizardite versus antigorite (Figure 2.16).

Bulk chemistry of major elements (Si, Al, Ti, Fe, Mg, Na, K, Mn, Ca, P, as well as LOI) and trace elements (Sc, V, Ni, Cu, Ga, Rb, Sr, Y, Zr, Nb, Ba, La, Hf, Pb, Th, and U) of the soil samples and rock cores was determined (Tables 2.6-2.9). Common nutrients, including calcium, potassium, and phosphorus, were observed in low concentrations (Tables 2.6 and 2.8). Nickel was observed in high concentrations ranging from 988-2832 ppm (Tables 2.7 and 2.9). Aluminum was observed in higher concentrations in the Scorpion Creek rock cores compared to those from Kangaroo Lake (Figures 2.17 and 2.18; Tables 2.6 and 2.8).

Biological Activity Reaction Tests

After 10 days of observation, none of the IRB-BART™ testers containing soil samples showed a definitive sign of iron-oxidizing bacteria, such as the formation of brown rings, brown gel and/or brown clouds. Control testers remained a translucent yellow color indicating the absence of bacterial growth (Figure 2.19a). On Day 24, however, the BARTs for Scorpion Creek 0-10 cm and Kangaroo Lake 8-18 cm tested positive for iron-oxidizing bacteria by the presence of a brown ring on the ball (Figure 2.19b). Between Days 10-30, the two bottom-most samples from Kangaroo Lake (28-38 cm and below 41 cm) began to develop a greenish tint throughout the tester and a yellow-green residue began to form on the ball (Figure 2.19d).

After 10 days of observation, none of the IRB-BART™ testers containing rock core samples showed signs of IRB. However, foam formed around the ball in two samples from Scorpion Creek (13-15 cm and 76 cm) and in one Kangaroo Lake sample (76-86 cm) by days Day 7-9 (Figure 2.19c). Foam, or gas bubbles nucleating on the ball, is an indication of the possible presence of anaerobic bacteria. One Scorpion Creek sample (13-15 cm) and one Kangaroo Lake sample (76-86 cm) developed a brown ring around the ball by Days 52 and 73, respectively, which may indicate the possible presence of iron-related bacteria (Figure 2.19b). The control testers remained a translucent yellow color throughout the course of observation which indicates a negative reaction to iron-oxidizing bacteria. A summary of all IRB-BART™ results can be found in Table 2.10.

Pore Waters, Siderophores, and Organic Constituents

Pore waters were extracted from the Scorpion Creek and Kangaroo Lake soils (~1.5- to 4.5-ml samples) to be tested for the presence of siderophores and organic constituents.

The CAS universal assay for siderophores showed maximum siderophore concentrations of 5.9 μM and 3.9 μM in the soil pore waters extracted from Scorpion Creek and Kangaroo Lake soils, respectively, based on the standard curve (Table 2.11; Appendix B). These concentrations were estimated assuming a siderophore similar in affinity to that of DFAM. In the context of siderophore content in the soil, maximum siderophore concentrations are 2.302 μmol dm^{-3} and 1.575 μmol dm^{-3} for Scorpion Creek and Kangaroo Lake, respectively (Table 2.11). Half of the pore water samples tested yielded siderophore concentrations that were below detection (Figure 2.20; Table 2.11).

Ultraviolet absorbance of the soil pore waters was measured at 253.7 nm (see Appendix C for more information) to estimate the presence of UV-absorbing organic constituents. The measured absorbance for soil pore waters from Scorpion Creek increase and then decrease slightly with depth (Figure 2.21; Table 2.12). The absorbance for the Kangaroo Lake pore waters is greatest for the topmost samples and is significantly less for the deeper samples with a slight increase at the deepest sample (Figure 2.21; Table 2.12). The Kangaroo Lake pore waters display greater absorbance than the Scorpion Creek samples. This is especially evident at the surface, where the Kangaroo Lake absorbance is approximately eight times greater than the Scorpion Creek absorbance.

Discussion

In order to determine the most important processes controlling incipient soil formation on serpentinite bedrock, the effects of allochthonous inputs, biological influences, and chemical weathering were examined. The young soils and temperate climate allow for the examination of the very early processes acting on soil formation, which would be more difficult to distinguish in older soils.

The input of allochthonous material, such as the deposition of atmospheric dust or other material from a different origin than the bedrock, appears to play a minimal role in soil formation at Scorpion Creek. The similarities between soil and parent rock mineralogy as measured by XRD (Figure 2.16; Table 2.5) at Scorpion Creek suggest that the weathering process at this location occurred as physical disaggregation of the parent rock to saprolite with little chemical alteration to secondary minerals. Because no minerals were found in the soil that were not found in the parent material below 10 cm depth, atmospheric dust deposition at Scorpion Creek is therefore assumed to be minimal.

At the Kangaroo Lake site, however, the input of allochthonous material may play a more important role in soil formation. The large number of angular rock clasts present in the soil and the higher content of clay-sized particles (Figures 2.3b and 2.15) do not seem to be consistent with the physical disaggregation of rock to saprolite as observed at Scorpion Creek. Given the glacial history of the region and the presence of larger angular rock clasts, the soil profile may be derived from glacial till deposited on serpentinite bedrock. The presence of plagioclase and quartz throughout the entire soil profile may be due to their presence in till or through deposition of dust; neither mineral was detected in the rock core samples (Table 2.5). Approximately 10-15% of the Trinity peridotite consists of plagioclase lherzolite (Quick, 1981), which could be a source of the

plagioclase found in the soil. The high clay content at Kangaroo Lake is consistent with the dust input scenario and may be the result of translocation of clay-sized dust particles throughout the profile. The higher clay content, which contributes to the water-holding capacity, and therefore the higher water content at Kangaroo Lake may allow for an environment more conducive to chemical weathering.

Serpentinites, due to their unusual chemistry, strongly control the composition and evolution of the biota that develop on them. However, the role that these biota play in the development of serpentine soils has not been examined. In order to assess some potential biological impacts on serpentinite weathering, pore water samples, soil, and rock fragments were analyzed to test for siderophores, organic constituents, and iron-oxidizing bacteria.

Iron is an important nutrient for microorganisms in aerobic environments. Iron is needed to reduce oxygen for the production of adenosine triphosphate (ATP), and it is also needed to form heme (Neilands, 1995). In oxic conditions Fe(III) is nearly insoluble, making the iron unavailable to microorganisms (Schwyn and Neilands, 1987). Some microorganisms including aerobic and facultative anaerobic bacteria and mycorrhizal fungi excrete siderophores, or low molecular mass, Fe(III)-specific ligands (Neilands, 1993; Haselwandter, 1995). These siderophores can play a significant role in Fe(III)-mineral weathering (Hersman et al., 1995). Siderophore-promoted dissolution has been documented in hematite (Hersman et al., 1995), and in hornblende and hornblende glass (Liermann et al., 2000; Kalinowski et al., 2000; Buss et al., 2007). Interactions between siderophores and mineral surfaces have been observed in the formation of iron-leached layers (Kalinowski et al., 2000) and etch pits in hornblende (Buss et al., 2007).

In addition, fungal species found in serpentine soils have been shown to release siderophores and preferentially remove ions from chrysotile (Daghino et al., 2006, 2008, 2009).

In this study, measurements of siderophores in the soil pore waters did not exceed concentrations of 5.9 μM (Table 2.11), assuming a siderophore similar to DFAM. These results can also be an indication that weaker iron-binding ligands, like citrate, are not present in high concentrations (Hausrath et al., 2007). A typical soil is estimated to contain an aqueous concentration of siderophores ranging from ~10 to ~2000 μmol per liter (Hersman et al., 1995). The unique chemistry of serpentinite-derived soils, including high iron concentrations, may account for why the observed siderophore concentrations in this study are below the expected siderophore concentrations of typical soils. These concentrations are far below those used the hematite dissolution experiments of Hersman et al. (1995), 240 μmol dm^{-3}. In addition, no other siderophore-related effects were observed such as leached layers or etch pits, which have been observed previously by Kalinowski et al. (2000) and Buss et al. (2007), respectively, on the mineral hornblende. The high concentrations of iron present in the serpentine soils may therefore result in minimal use of siderophores by the local biota.

Organic constituents, such as organic acids are of interest in mineral studies because they can affect mineral weathering rates (Drever and Stillings, 1997). The presence of oxalic acid ($H_2C_2O_4$) has been shown to enhance dissolution rates of feldspar up to a factor of 15 (Drever and Stillings, 1997). Drever and Stillings (1997) also note that the concentration of oxalic acid generally must be on the order of 1 mM in order to cause a significant effect on feldspar dissolution. Hausrath et al. (2009) observed

enhanced dissolution in both granite and basalt in the presence of citrate ($C_3H_5O(COO)_3^{3-}$) compared to organic-free experiments. Formic (HCOOH) and acetic acid (CH_3COOH) have been observed to cause enhanced extraction of Mg and Fe in serpentinite dissolution, though not to same extent as sulfuric, hydrochloric, and nitric acids (Teir et al., 2007b). Oxalate has also been shown to enhance the dissolution of lizardite in laboratory batch reactor experiments (Yardley, 2011).

Absorbance at 253.7 nm wavelength was measured on the soil pore waters to estimate organic contributions. Although this method does not yield concentrations of specific organic acids, it does allow for observation of relative changes in either total or UV-absorbing organic matter as a function of depth. In both profiles, the highest absorbances are observed at the surface. Additionally, there is an increase in absorbance at the lowest measured depth at Kangaroo Lake. This is consistent with the most intense biological impacts on weathering at the soil surface, as well as at the soil-rock interface. Previous studies have postulated communities of iron-oxidizing bacteria at the soil-rock interface (Buss et al., 2005; Hausrath et al., 2011), and therefore the soils and rock cores in this study were tested for those communities.

Iron-related bacteria were tested for using BARTs™, a method previously used to analyze for iron-oxidizing bacteria (Buss et al., 2005). Iron-oxidizing bacteria were observed in both the rock cores and soils, with more active communities present in the soils. This suggests that iron oxidation is being mediated by iron-oxidizing bacteria in the transition from rock to soil. In addition, reddish staining was observed on the edges of rock fragments from the soils and from rock cores, which is likely the result of oxidation of the iron from magnetite, serpentine, or pyroxene present in the parent rock to

hematite. Extensive cracking near the surface of soil and rock core cross sections was also observed in SEM (Figures 2.10 and 2.13) at Kangaroo Lake, and to a lesser extent at Scorpion Creek. The oxidation of ferrous minerals and precipitation of ferric oxides can cause cracking due to an increase in molar volume (Fletcher et al., 2006). Iron-oxidizing bacteria are present in both the soil and rock cores, and may therefore be important in the weathering of ferrous iron-containing minerals within serpentinite rock to serpentine soil.

The role of iron oxidation in iron-silicate weathering is complicated and has been shown to either inhibit or enhance mineral dissolution (see Welch and Banfield, 2002, and references therein). Iron-oxidizing bacteria, specifically *Acidithiobacillus ferrooxidans,* have been shown to inhibit fayalite dissolution rates by 50-98% in batch reactors under acidic conditions (Santelli et al., 2001) due to the release of ferric iron and its interactions with mineral surface sites (Welch and Banfield, 2002). In contrast, Buss et al. (2005) found that iron-oxidizing bacteria may facilitate the disaggregation of quartz diorite through spheroidal weathering at the saprolite-bedrock interface by consuming Fe(II) and O_2. In a spheroidal weathering model, Fletcher et al. (2006) noted that the oxidation of ferrous minerals and precipitation of ferric oxides results in an increase in molar volume, thereby causing cracking or fracturing within the rock. Iron-oxidation within the serpentinite rock and serpentine soil may therefore be an integral part of the chemical weathering process.

Chemical weathering of minerals within the weathered rinds of the serpentinite is observed to follow the order (from least resistant to most resistant): pyroxene > iron-rich serpentine > magnesium-rich serpentine > aluminum-rich serpentine. Pyroxene is observed to be the first mineral to dissolve out of the serpentinite rock (Figure 2.11),

consistent with laboratory experiments (Figure 2.1), which indicated that at the pH measured in these soils (pH 5.81-7.34), pyroxene dissolves more rapidly than lizardite. It is anticipated that pyroxenes in general would dissolve more rapidly than layer silicate minerals, due to the larger number of bridging oxygens per tetrahedron in layer silicates relative to inosilicate, or chain silicate, minerals (Brantley, 2003).

Iron-rich veins of serpentine were observed to dissolve more rapidly than the surrounding magnesium-rich serpentine (Figure 2.12), but less rapidly than the pyroxene (i.e. dissolution of iron-rich serpentine occurred closer to the surface than the pyroxene, but within apparently unaltered magnesium-rich serpentine). Measurement of the rates of water exchange from the solvent to the hydration sphere of the metal ion suggest that iron-containing minerals should dissolve more rapidly than the corresponding magnesium-rich mineral (Casey and Westrich, 1992), which is consistent with these observations as well as with the measured dissolution rate for antigorite (Figure 2.1). The use of ferrous iron by iron-oxidizing bacteria could also contribute to the preferential dissolution of ferrous iron-rich minerals, and enhanced weathering, as has previously been observed in granites (Buss et al., 2005).

Lastly, the aluminum-rich serpentinite at Scorpion Creek is observed to be much less weathered than the less aluminum-rich serpentinite at Kangaroo Lake. Although this is likely due to multiple factors, including clay content of the soils, pyroxene content of the parent rock, and iron content, it may also be due to stabilizing effect of aluminum within the serpentine structure. The high aluminum concentration within serpentine can result in stronger interactions and increased stability within the mineral lizardite (O'Hanley and Dyar, 1993). Therefore, aluminum-rich serpentinite is expected to

weather less rapidly than less-serpentinized counterparts, both because the pyroxene is no longer present within the rock causing increased porosity, and also because the aluminum acts to stabilize the lizardite structure.

The first mineral to dissolve within a parent rock has been termed the "profile-controlling mineral" due to its importance in porosity generation in facilitating the weathering of additional minerals (Brantley and White, 2009). In these serpentinite rocks, pyroxene dissolution appears to be the first mineral to dissolve, generating additional porosity to allow first iron-rich serpentine minerals, and then magnesium- and aluminum-rich serpentine to dissolve. Incipient weathering of serpentinites may, therefore, be controlled by a trace, non-serpentine mineral within the rock.

Conclusions

Two sites in the Klamath Mountains of northern California, Scorpion Creek and Kangaroo Lake, were sampled in order to analyze serpentinite from the unweathered parent rock to the soil surface. Iron-oxidizing bacteria were found to be present in both the soils and the rock cores at each sampling location. Oxidized iron was also found to be present on weathering rinds in the soil and rock cores. Mineral dissolution in the weathered samples appears to follow a specific order: pyroxene > iron-rich serpentine > magnesium-rich serpentine > aluminum-rich serpentine. This mineral order is likely based on mineral dissolution kinetics where pyroxene tends to dissolve faster than serpentine (Bandstra and Brantley, 2008;Chen and Brantley, 1998; Eggleston et al, 1989; Hoch et al., 1996; Knauss et al., 1993; Schott et al., 1981; Golubev et al., 2005), and also the fact that iron-containing minerals tend to dissolve faster than magnesium-containing

minerals (Casey and Westrich, 1992). However, this may also be influenced by the use of ferrous iron by iron-oxidizing bacteria. The observation that aluminum-rich serpentine is the slowest to dissolve is likely influenced by all of these factors, but is probably also due to the stabilizing effect that aluminum has on the lizardite mineral structure (O'Hanley and Dyar, 1993). These findings help quantify the incipient processes affecting serpentine soil formation, which are important to the further development of the soil and the biota that grow on them, and have important implications for the chemical compositions of serpentinites used in mineral carbonation.

Figures

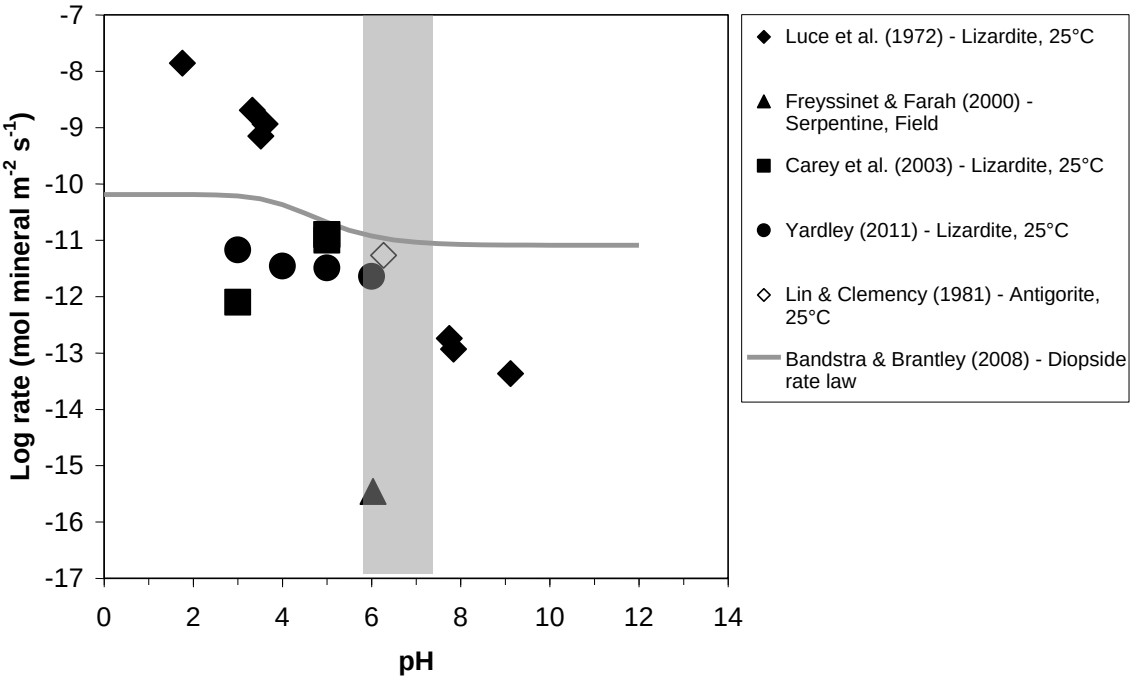

Figure 2.1. Compilation of lizardite, antigorite, and diopside dissolution rates from the literature showing the log of the mineral dissolution rate versus pH. The gray shaded box represents the pH range (5.81-7.34) measured from Scorpion Creek and Kangaroo Lake soil samples. Freyssinet and Farah (2000) is a rate of serpentine dissolution measured in the field (average pH of water samples is shown) which estimated surface area using BET. Note the discrepancy between laboratory lizardite rates and the field measured rate for serpentine. Diopside has been shown to dissolve more quickly than lizardite within the shaded pH range denoted above. The diopside rate law was calculated by Bandstra and Brantley (2008) from previously published diopside dissolution rates (Chen and Brantley, 1998; Eggleston et al, 1989; Hoch et al., 1996; Knauss et al., 1993; Schott et al., 1981; Golubev et al., 2005). Rates from Luce et al. (1972) were obtained from Sverdrup (1990), and rates from Carey et al. (2003) and Lin and Clemency (1981) were obtained from Orlando et al. (2011).

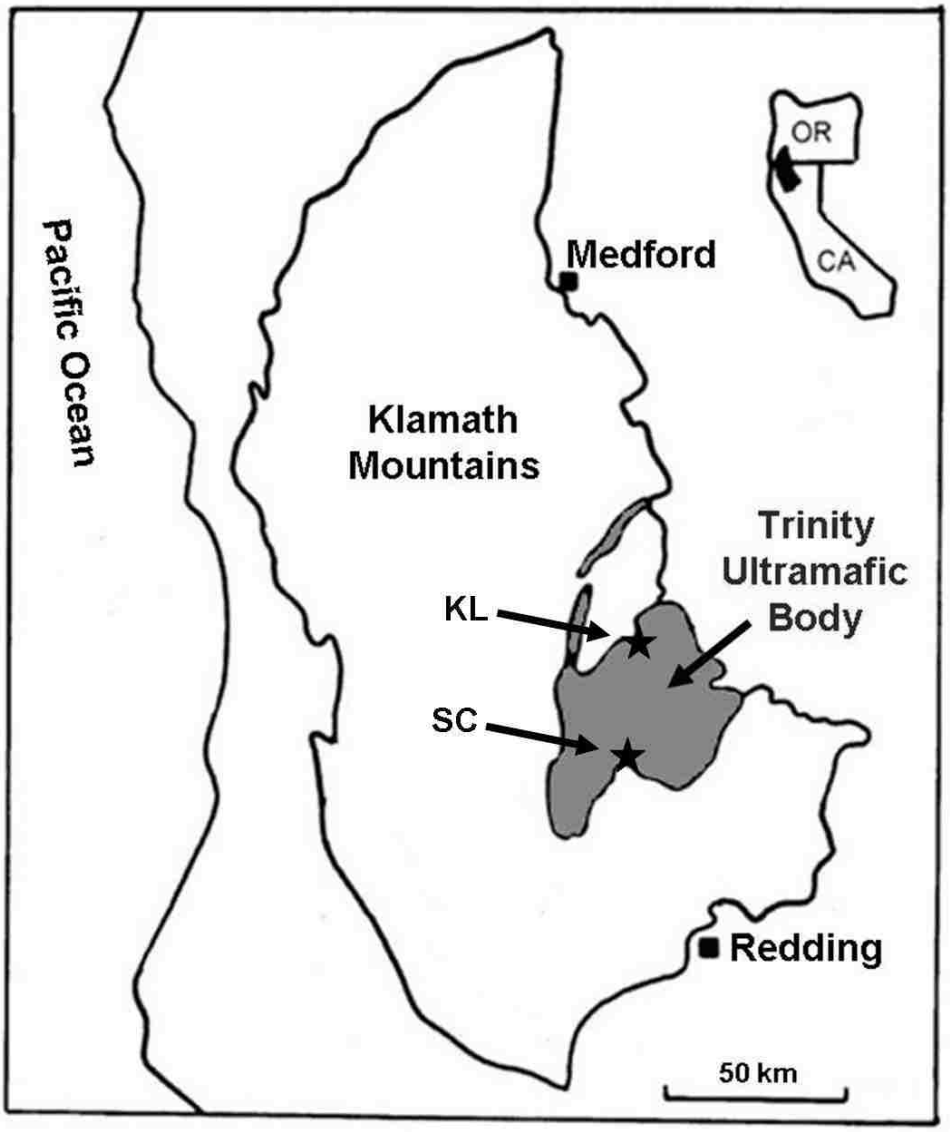

Figure 2.2. Map showing the approximate sampling localities of Scorpion Creek (SC) and Kangaroo Lake in the Klamath Mountains of northern California. Gray shaded areas indicate the Trinity ultramafic body (modified from Alexander, 2004).

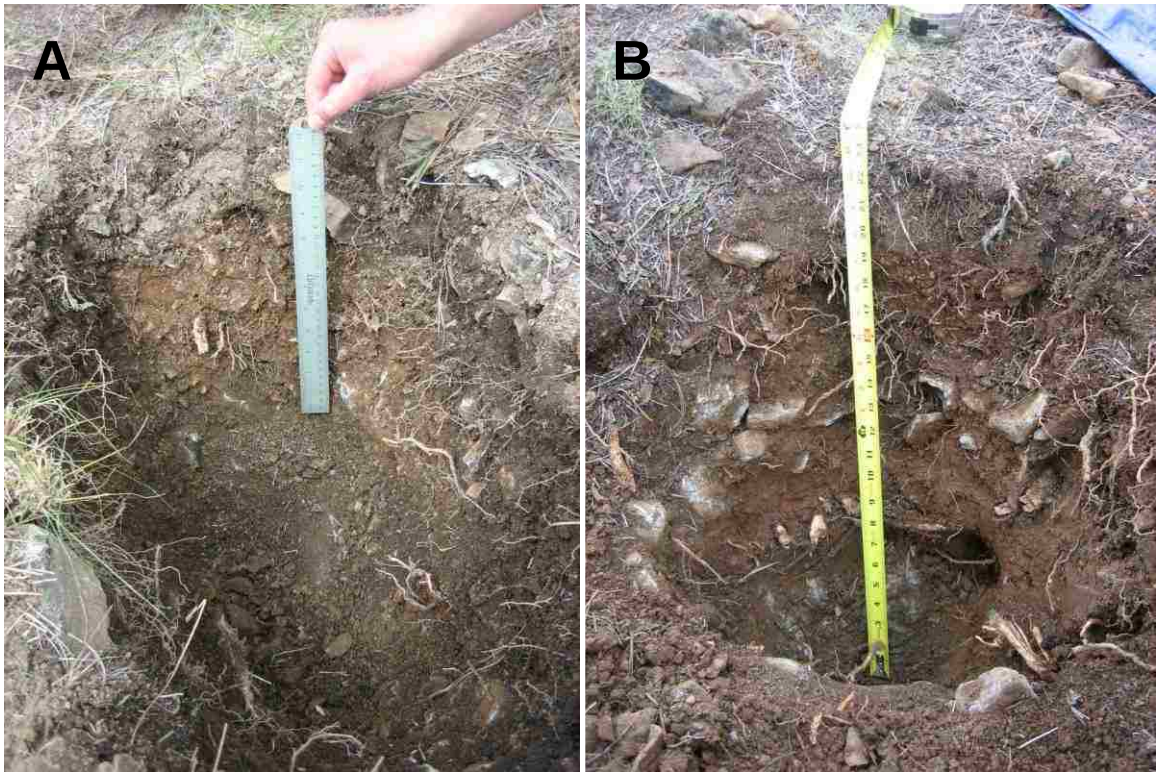

Figure 2.3. Photographs of soil pits sampled to depth of refusal at A) Scorpion Creek (40 cm) and B) Kangaroo Lake (56 cm). Note the reddish color of the soils, abundance of rock fragments, and the presence of roots in these soils, especially at Kangaroo Lake.

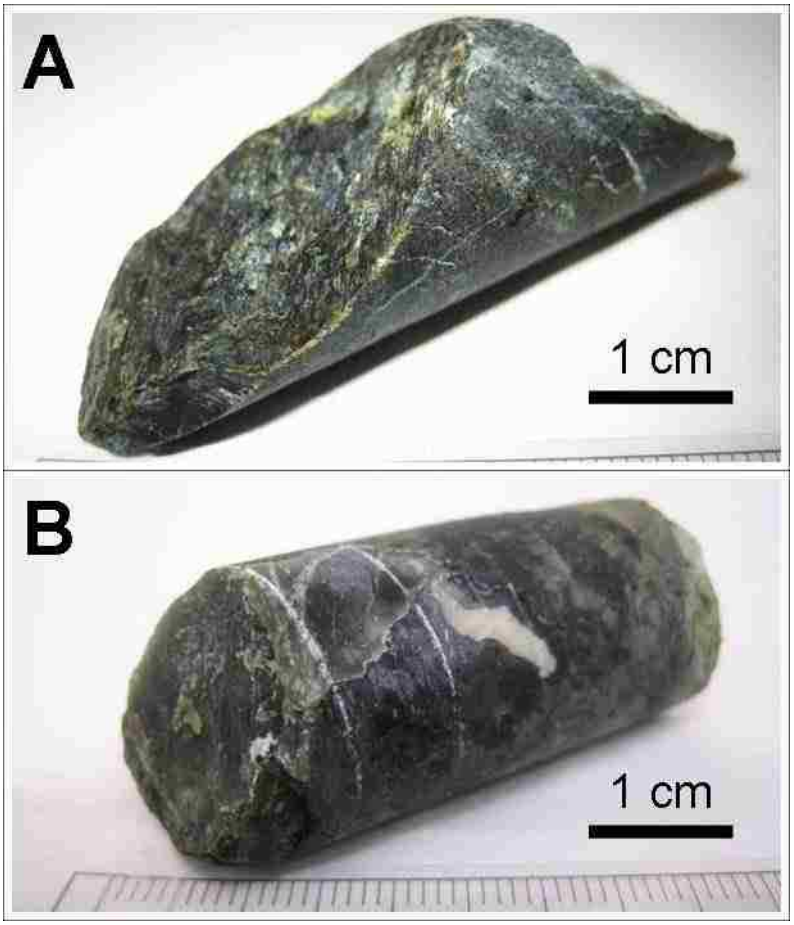

Figure 2.4. Photographs of rock cores collected with a backpack drill from A) Scorpion Creek (76 cm) and B) Kangaroo Lake (135 cm).

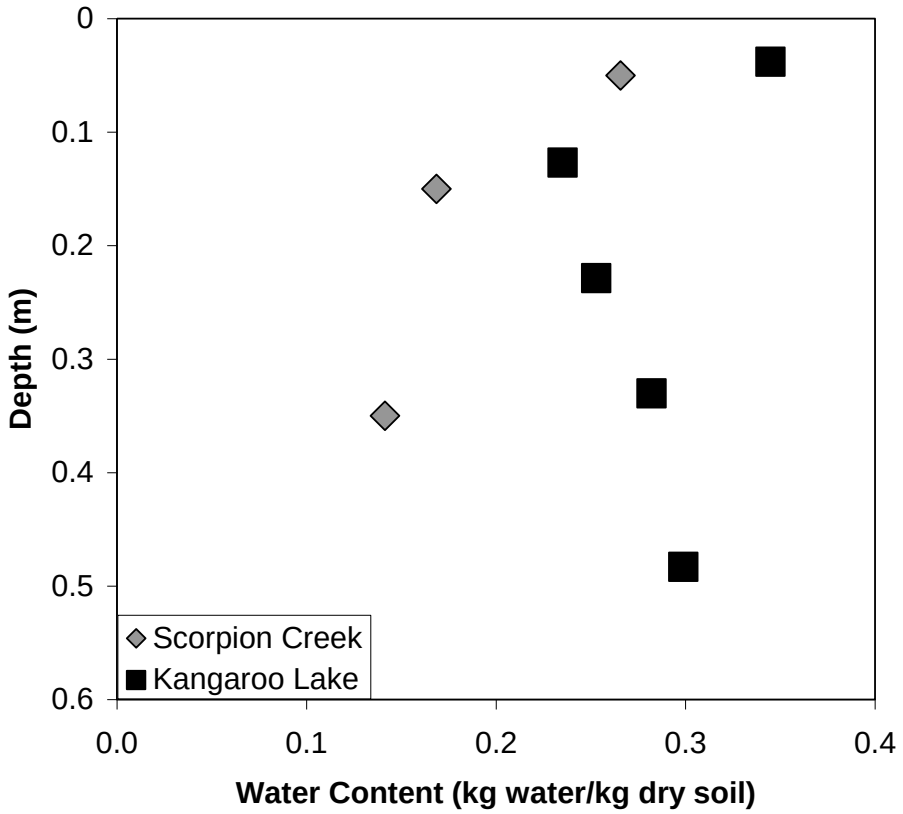

Figure 2.5. Water content versus depth for the soils developed on serpentinite at Scorpion Creek (gray diamonds) and Kangaroo Lake (black squares) (See also Table 2.1).

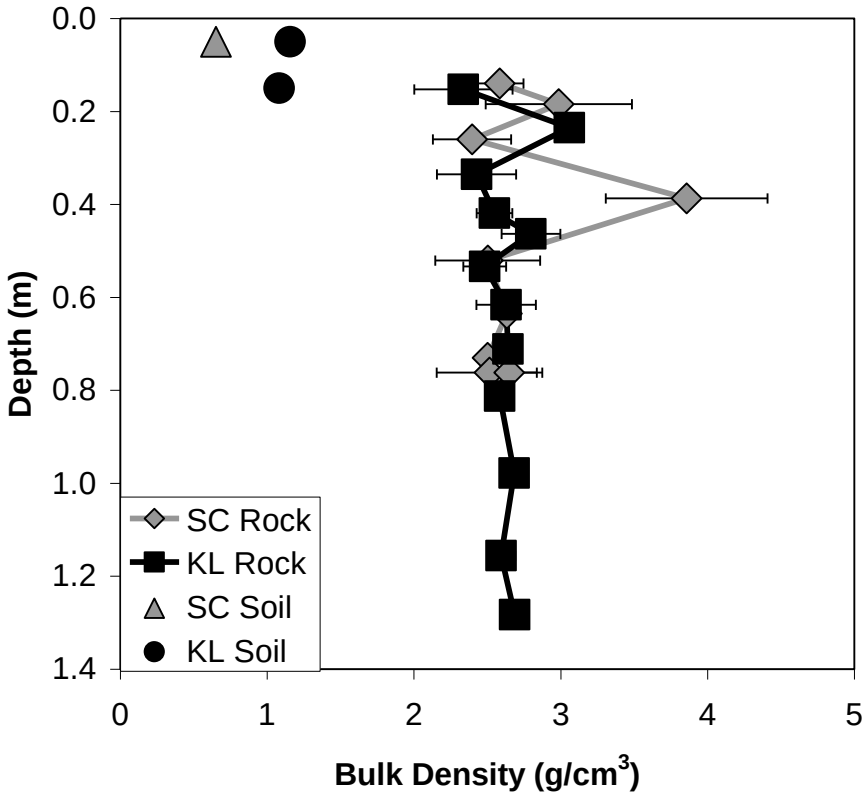

Figure 2.6. Bulk density versus depth for the serpentinite-derived soils at Scorpion Creek (gray triangle) and Kangaroo Lake (black circles) and for serpentinite rock cores from Scorpion Creek (gray diamonds) and Kangaroo Lake (black squares). Error bars represent the uncertainty propagated through the measurement of rock core bulk density. Where uncertainties are large, the sample size was small; the uncertainty in those measurements is, therefore, larger (See also Tables 2.2 and 2.3).

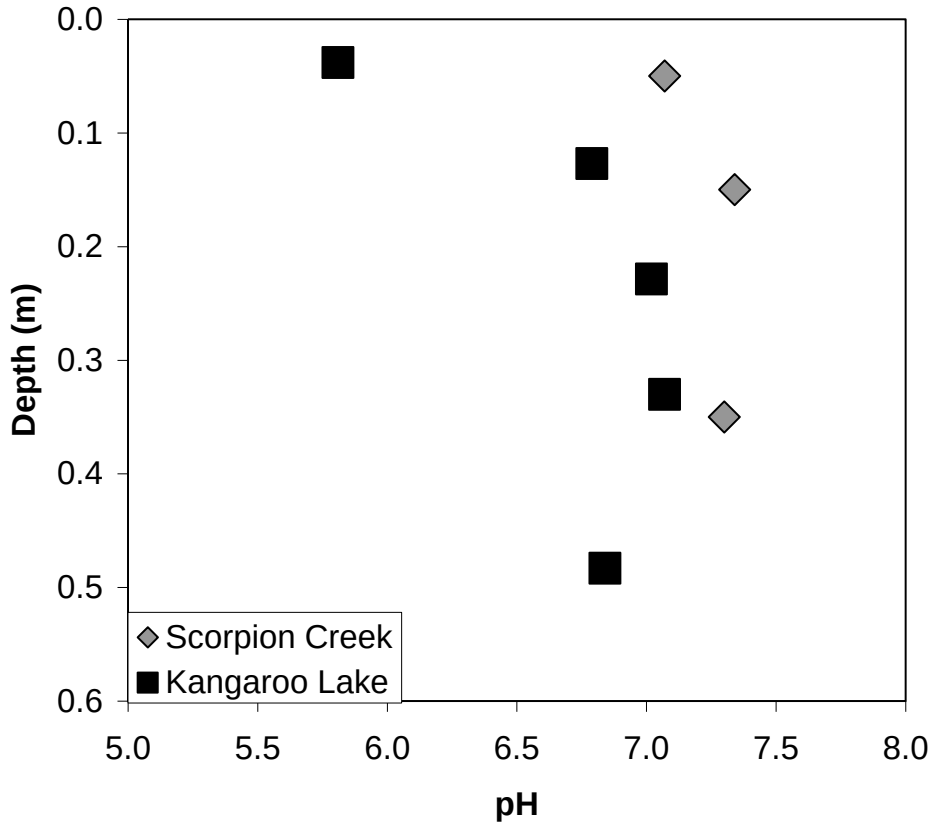

Figure 2.7. pH versus depth for the serpentinite-derived soils from Scorpion Creek (gray diamonds) and Kangaroo Lake (black squares) (See also Table 2.1).

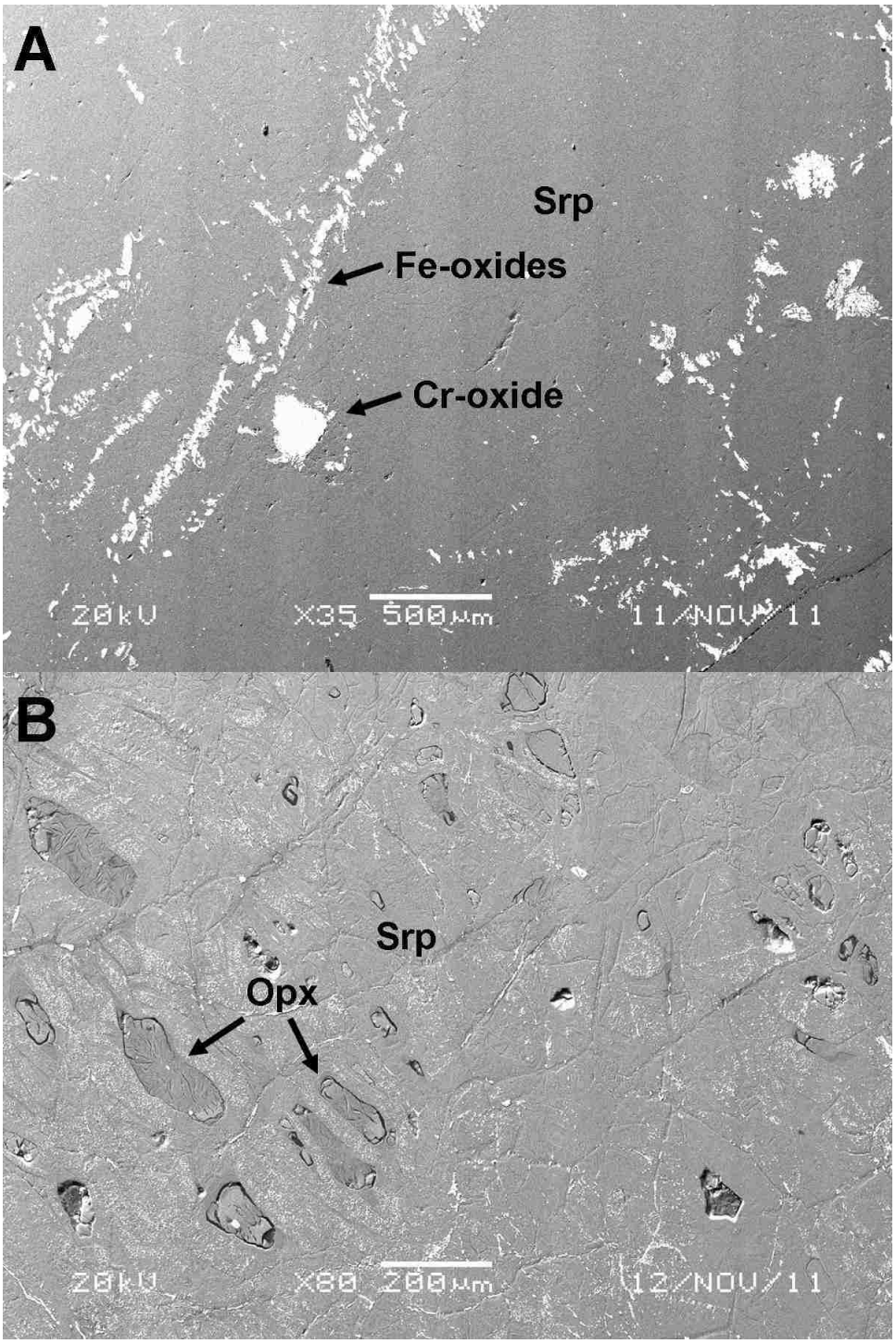

Figure 2.8. Backscattered electron micrographs of a rock core cross sections A) from Scorpion Creek (70-76 cm depth) showing characteristic serpentine (Srp, gray) with accessory iron- and chromium-oxides (white) and B) from Kangaroo Lake (27-41 cm depth) showing characteristic serpentine (Srp, gray) with accessory orthopyroxene (Opx) and iron- and chromium-oxides (white). Scale bars are 500 microns and 200 microns, respectively.

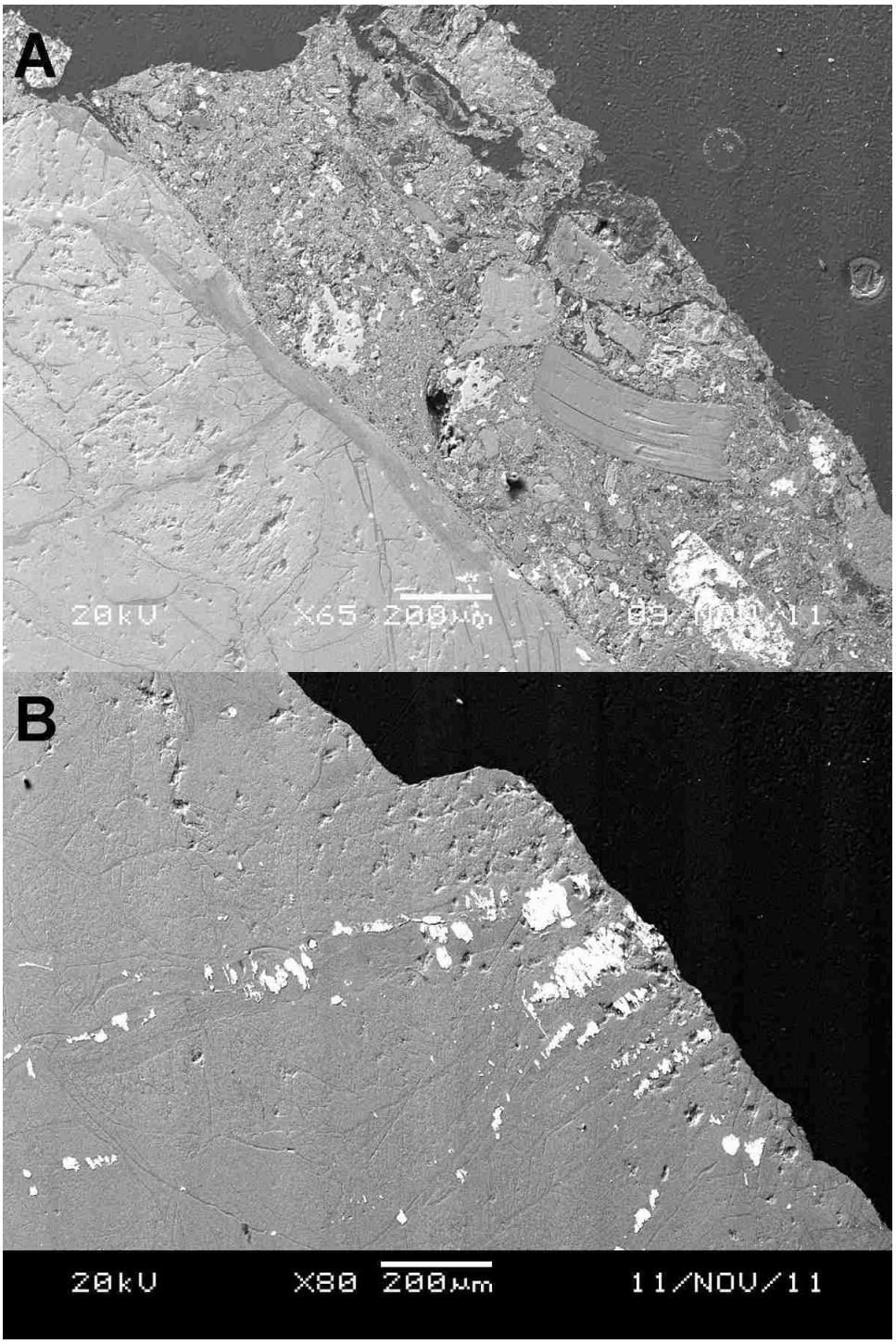

Figure 2.9. Backscattered electron micrographs of cross sections of rock fragments from the A) Scorpion Creek soil profile (0-10 cm depth) and B) Scorpion Creek rock cores (70-76 cm depth). There is little chemical change throughout the serpentine towards the exterior of the samples. A surficial coating of weathered rock and soil is accumulated on the surface of image A. Scale bar is 200 microns for both micrographs.

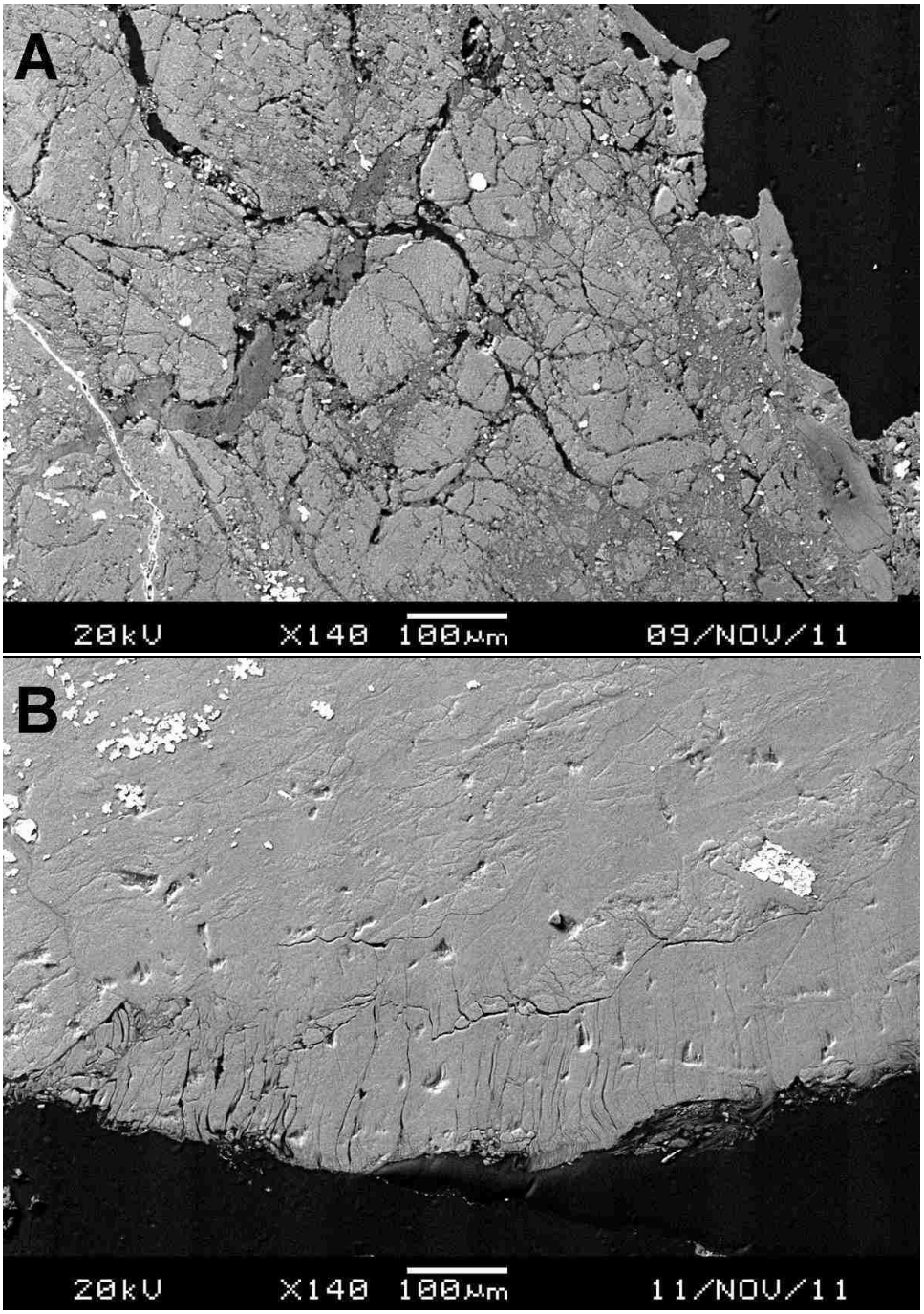

Figure 2.10. Backscattered electron micrographs of cross sections of rock fragments from the A) Scorpion Creek soil profile (30-40 cm depth) and B) Scorpion Creek rock cores (70-76 cm depth). Cracking and apparent disaggregation of the serpentine rock fragments are present along some surfaces, but are not extensive throughout the samples. There is little chemical variation in the serpentine towards the cross section exterior. Scale bar is 100 microns for both micrographs.

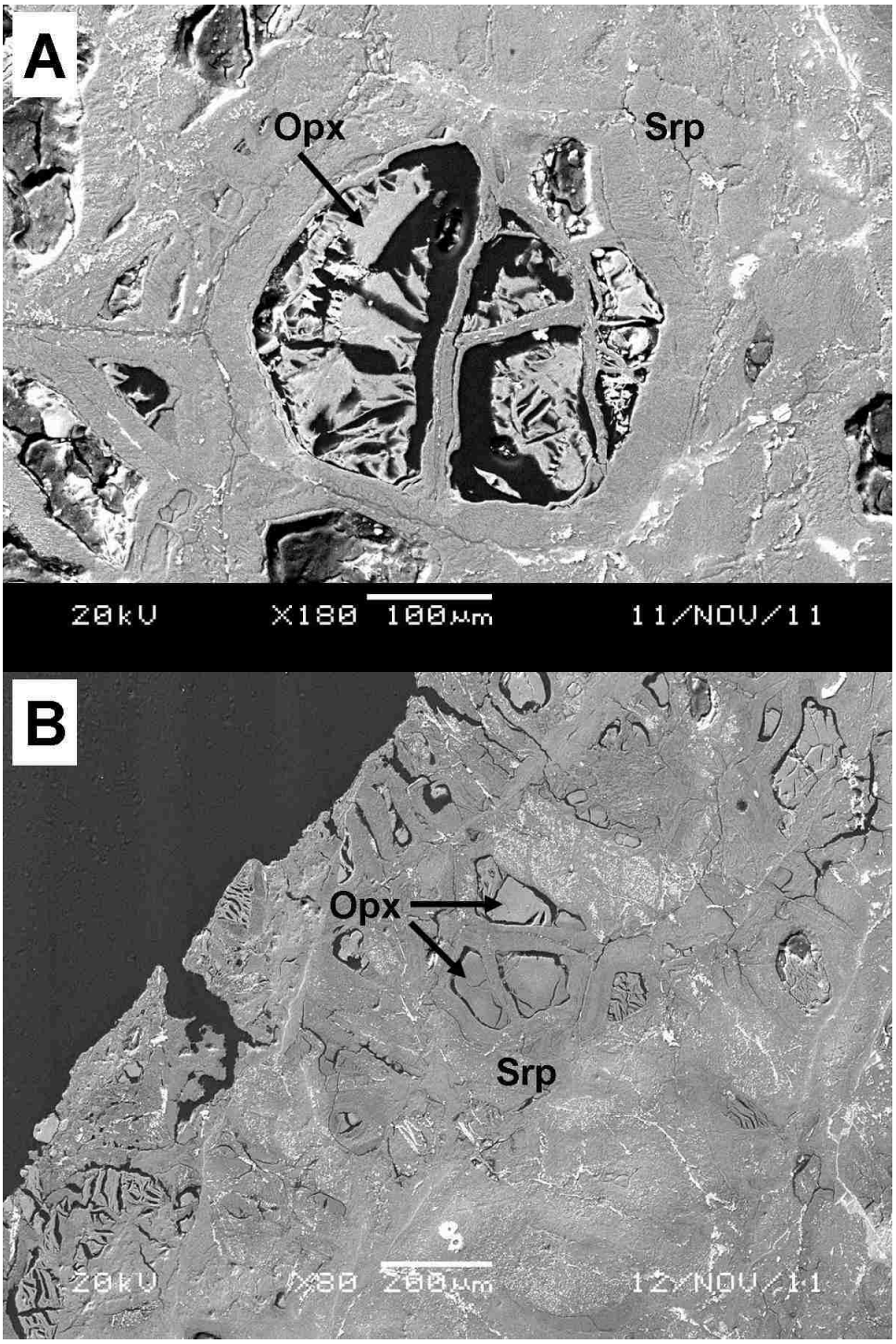

Figure 2.11. Backscattered electron micrographs of cross sections of rock fragments from the A) Kangaroo Lake soil profile (0-8 cm depth) and B) Kangaroo Lake rock cores (27-41 cm depth). Orthopyroxene (Opx) is present, although notably dissolved, in the sample and surrounded by serpentine (Srp). Scale bars are 100 microns and 200 microns, respectively.

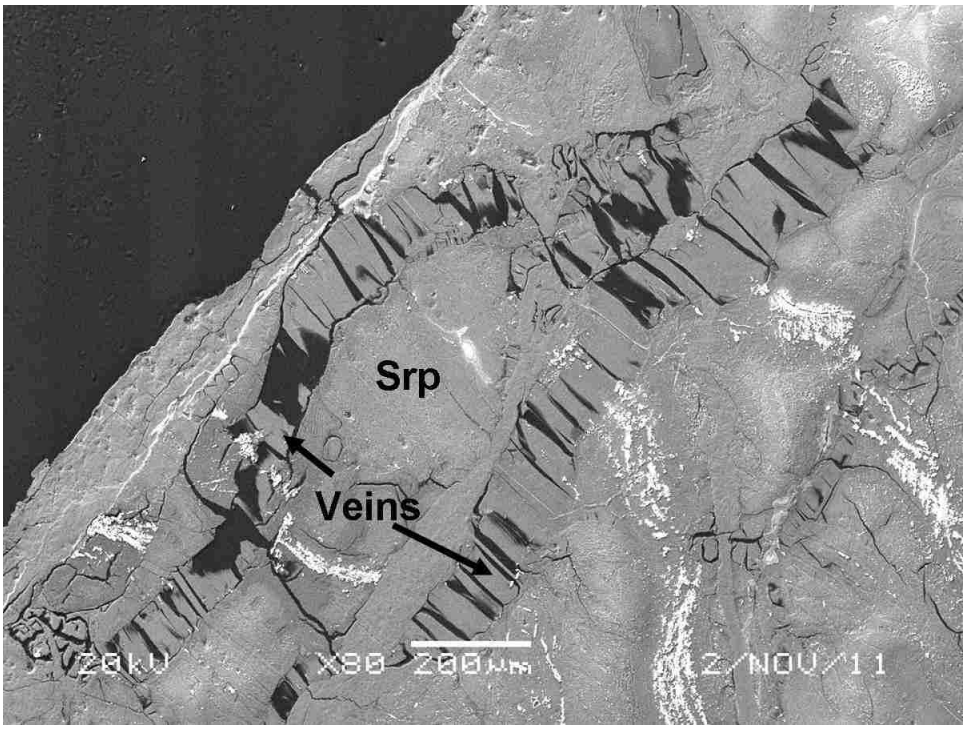

Figure 2.12. Backscattered electron micrograph of a cross section of a rock fragment from the Kangaroo Lake rock cores (27-41 cm depth). Veins of iron-rich serpentine appear to have preferentially dissolved out of the surrounding serpentine (Srp). Scale bar is 200 microns.

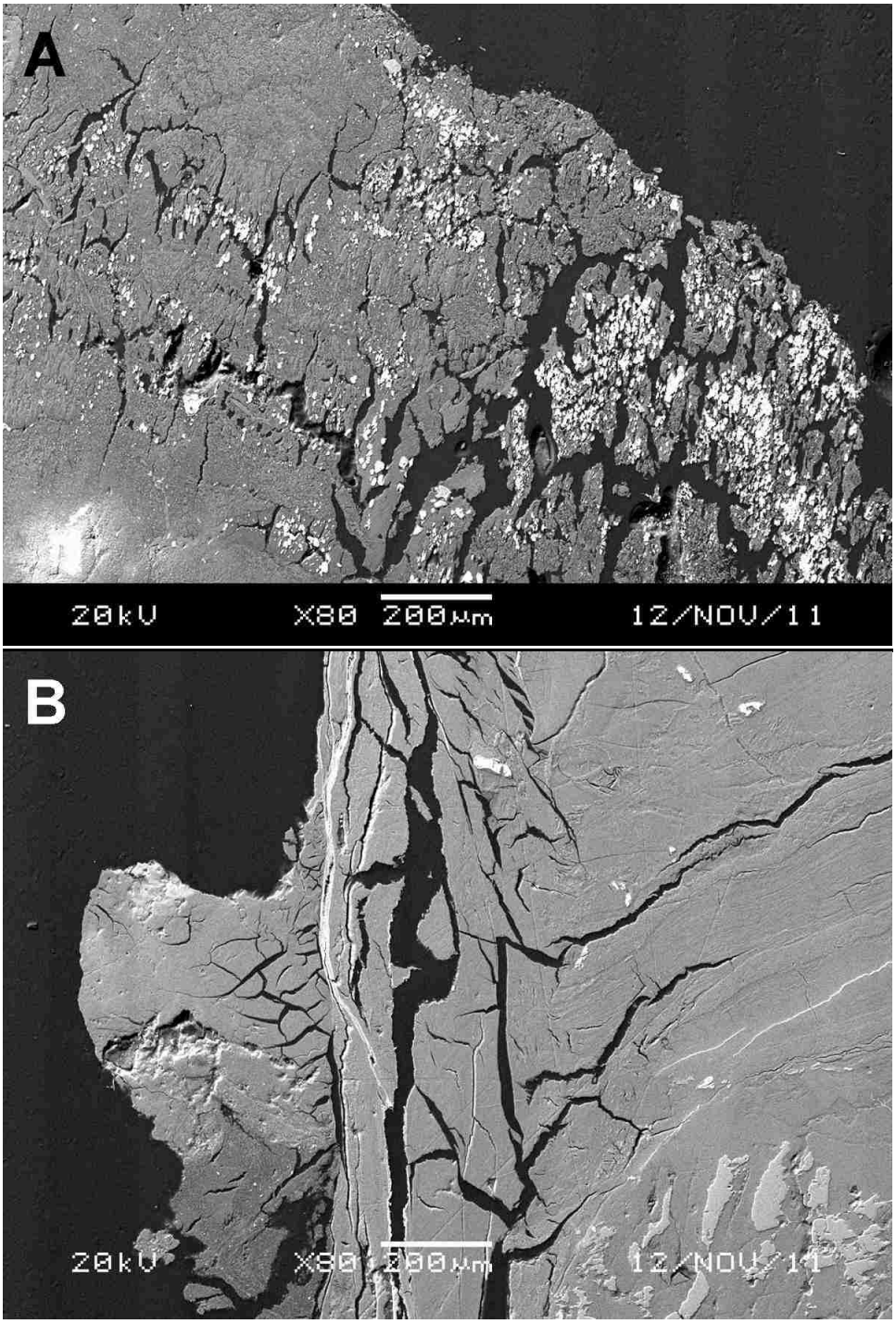

Figure 2.13. Backscattered electron micrographs of cross sections of rock fragments from the A) Kangaroo Lake soil profile (below 41 cm depth) and B) Kangaroo Lake rock cores (122-135 cm depth). Extensive fractures and cracking are common near the surfaces of the cross sections.

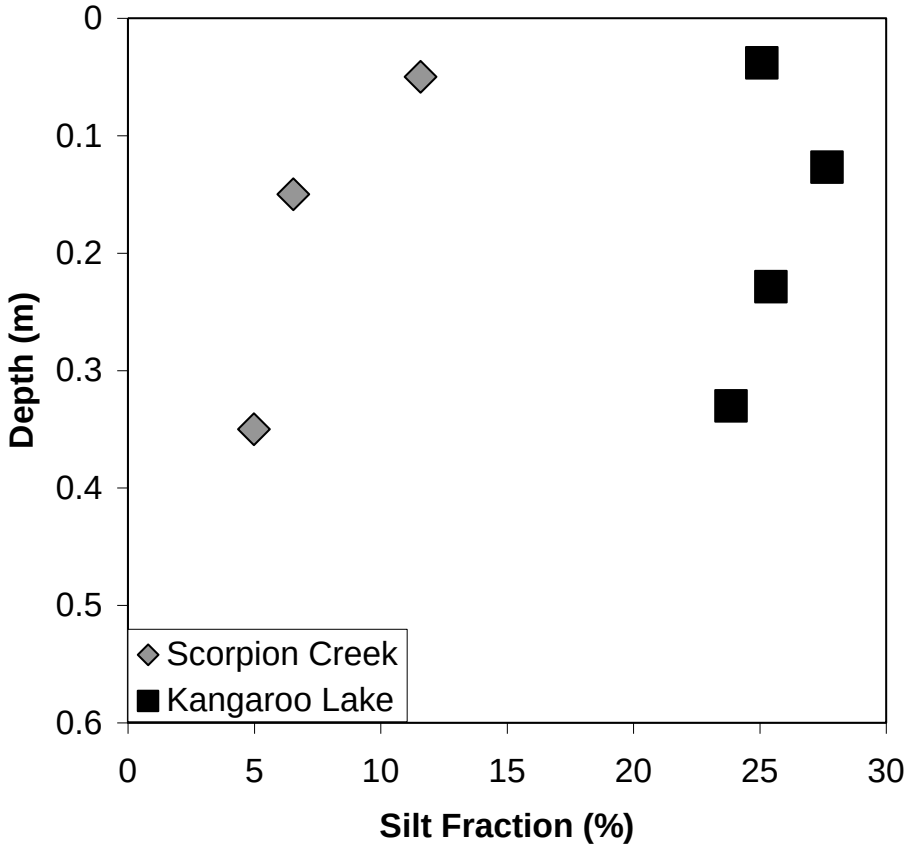

Figure 2.14. Percent silt fraction (by weight) versus depth of the soils collected from Scorpion Creek (gray diamonds) and Kangaroo Lake (black squares) (See also Table 2.4).

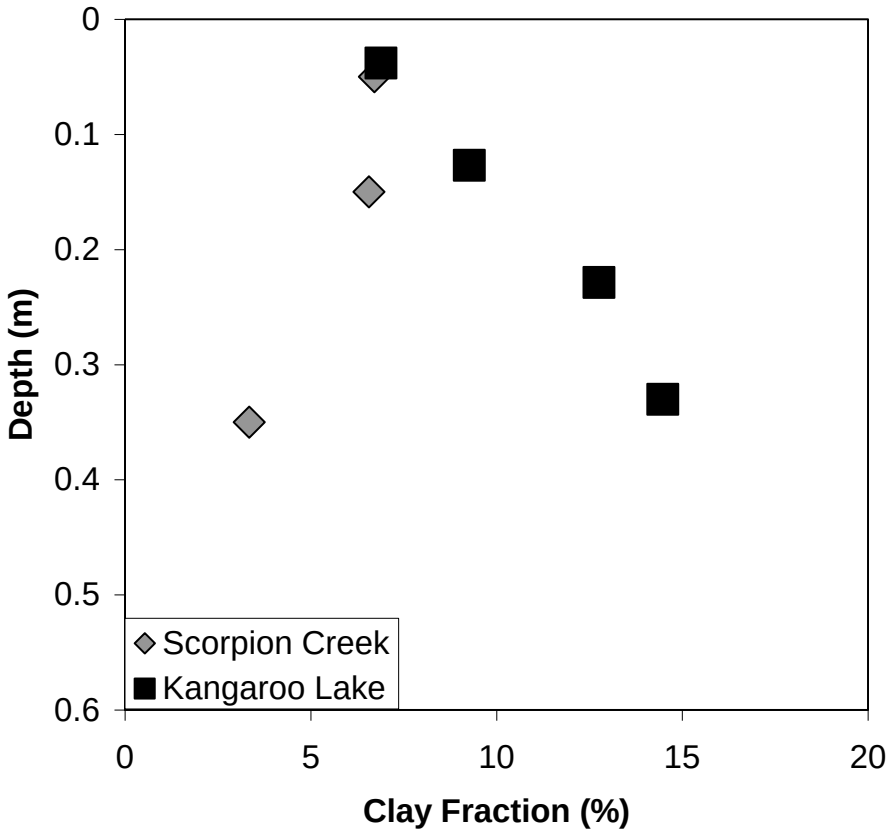

Figure 2.15. Percent clay fraction (by weight) versus depth of the soils collected from Scorpion Creek (gray diamonds) and Kangaroo Lake (black squares) (See also Table 2.4).

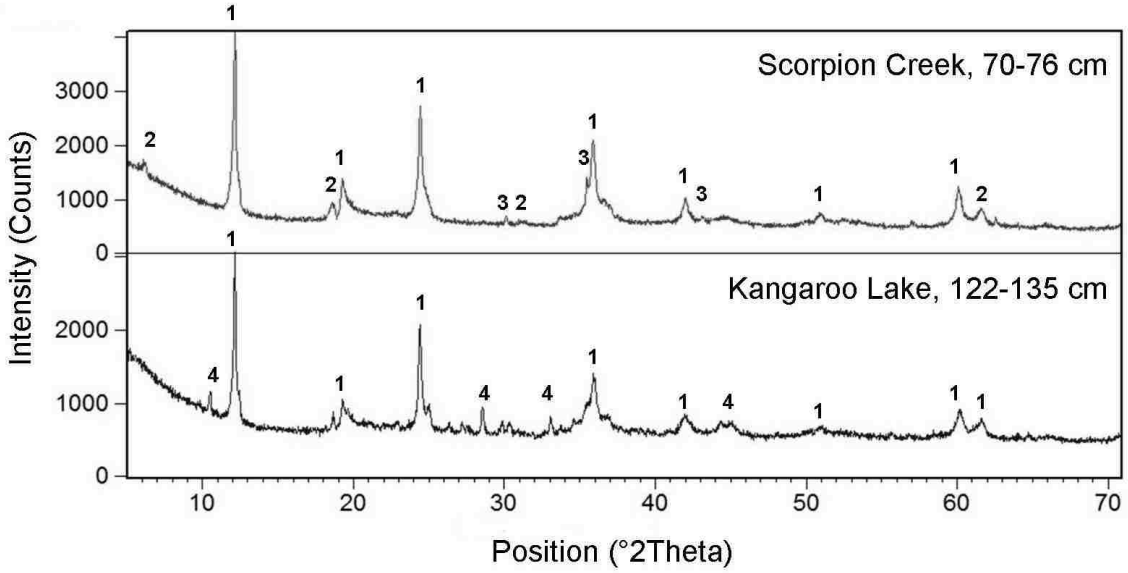

Figure 2.16. XRD micrographs of parent rock core for Scorpion Creek 70-76 cm and Kangaroo Lake 122-135 cm. Lizardite (1), clinochlore (2), and magnetite (3) are present in the Scorpion Creek rock core. Lizardite (1) and tremolite (4) are present in the Kangaroo Lake rock core (See also Table 2.5).

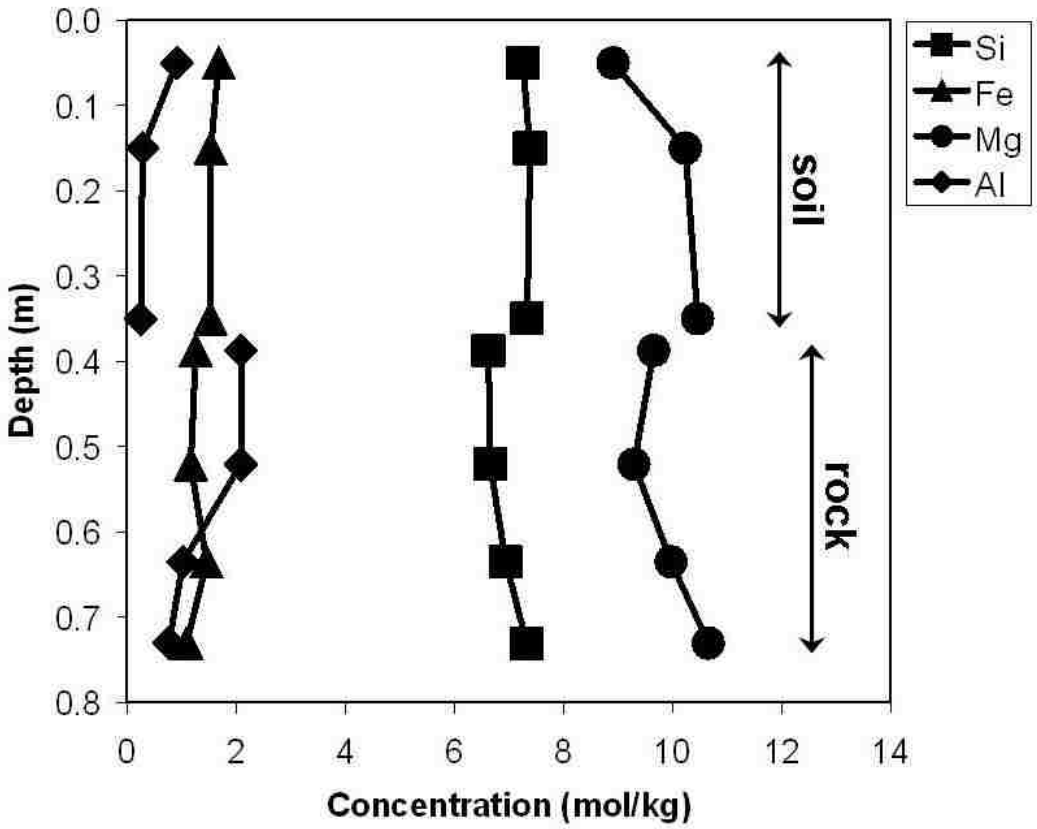

Figure 2.17. Elemental concentrations (in mol/kg) determined by XRF versus depth for Scorpion Creek soil and rock cores (See also Table 2.6).

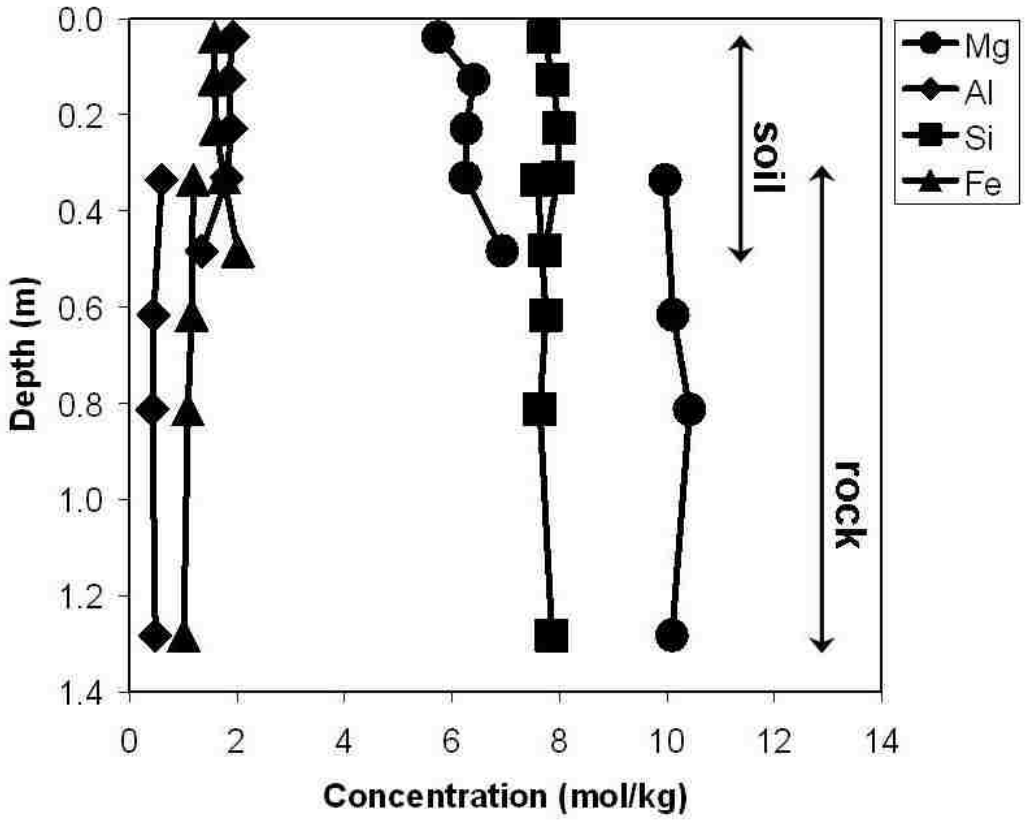

Figure 2.18. Elemental concentrations (in mol/kg) determined by XRF versus depth for Kangaroo Lake soil and rock cores (See also Table 2.8).

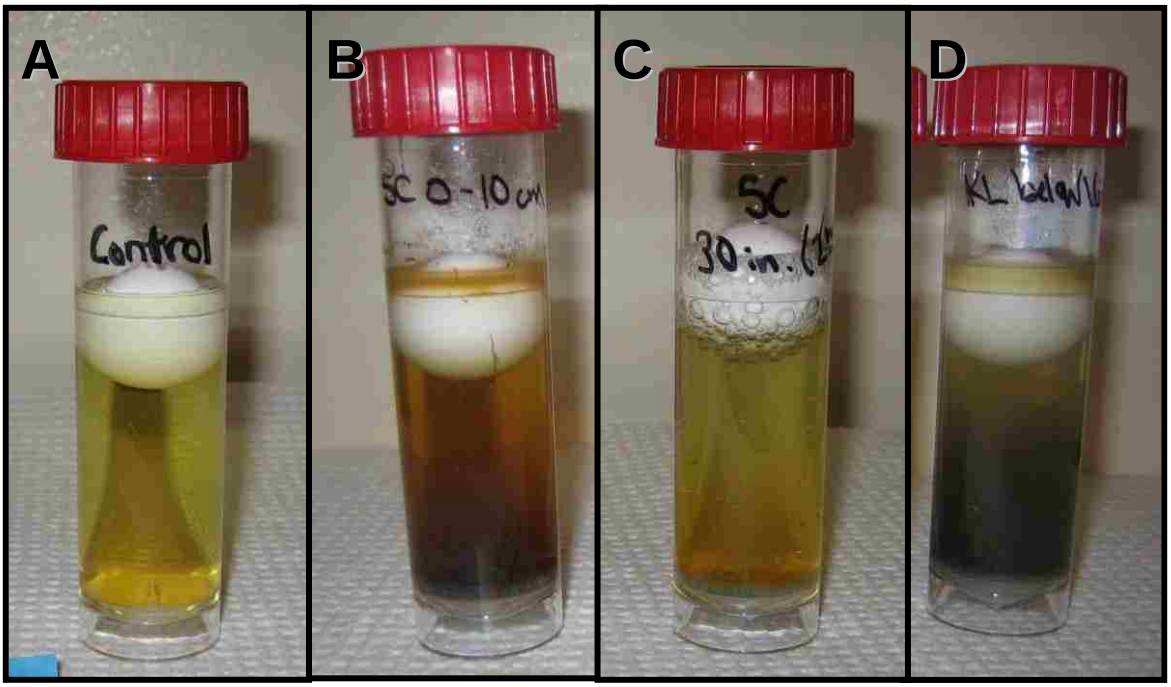

Figure 2.19. Photographs of BARTs containing the characteristic reactions observed in the Scorpion Creek and Kangaroo Lake soils and rock cores. A) Control testers remained a translucent yellow color without signs of growth (Day 24 is shown). B) Brown rings formed around the ball indicate the presence of iron-related bacteria. Soil from the Scorpion Creek 0-10 cm depth interval is shown on Day 24. C) Foam around the ball may indicate the growth of anaerobic bacteria. A rock core sample from a depth of 76 cm from Scorpion Creek is shown on Day 9. D) Yellow-green residue on the ball was observed; however, what it indicates is unknown. Soil from the Kangaroo Lake depth interval below 41 cm is shown on Day 30 (See also Table 2.10).

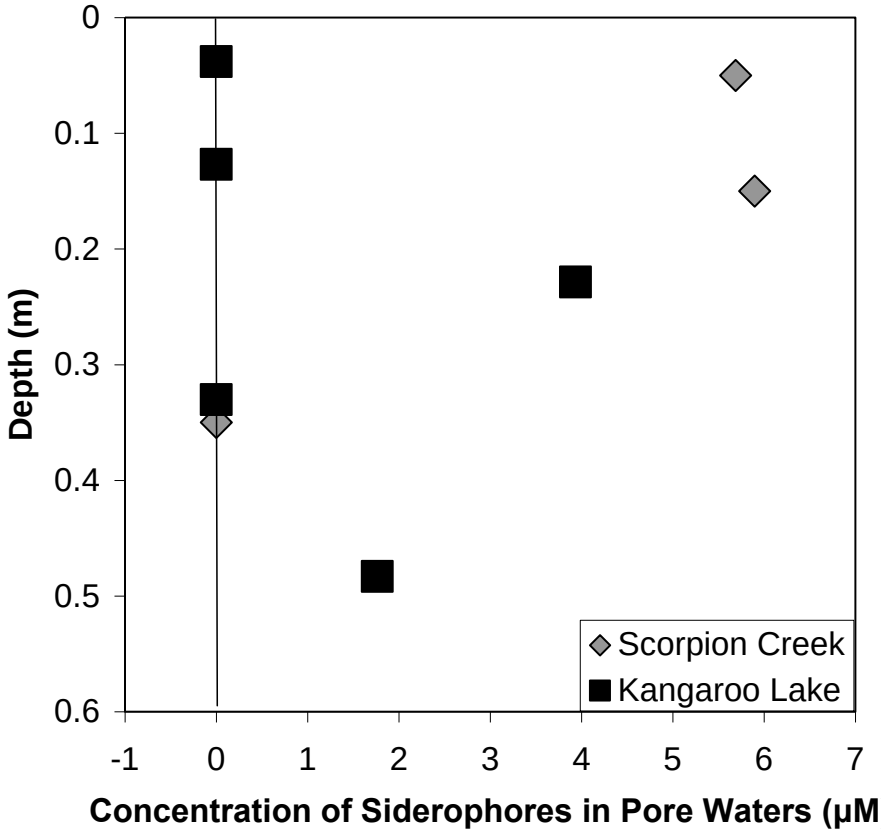

Figure 2.20. Concentrations of siderophores present in soil pore waters from Scorpion Creek (gray diamonds) and Kangaroo Lake (black squares. Concentrations were estimated based on the DFAM standard curve obtained from UV-absorbance measured at 630 nm wavelength (see Appendix B). DFAM is the commercially available siderophore deferoxamine mesylate. Concentrations plotted at 0 µM above represent concentrations that were below detection (see also Table 2.11).

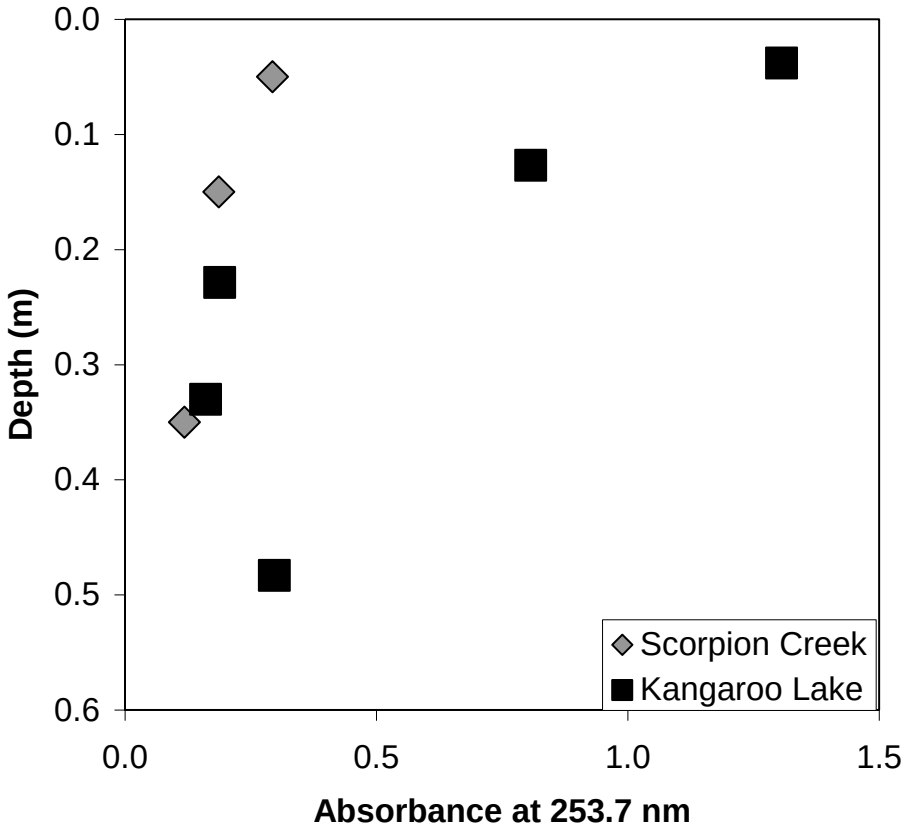

Figure 2.21. Ultraviolet absorbance of Scorpion Creek (gray diamonds) and Kangaroo Lake (black squares) soil pore waters measured at 253.7 nm to give an estimate of the presence of UV-absorbing organic constituents. Plotted absorbances are an average of three instrument readings, except in the case of Scorpion Creek 0-10 cm and 10-20 cm, which are an average of two readings (see also Table 2.12).

Tables

Table 2.1. Soil characteristics

Depth	Moist Color	Dry Color	Texture	pH	Water Content (kg/kg†)
Scorpion Creek:					
0-10 cm	10 YR 3/1	10 YR 6/3	loamy sand	7.07	0.27
10-20 cm	10 YR 3/6	10 YR 6/4	N/A*	7.34	0.17
30-40 cm	10 YR 3/4	10 YR 6/4	N/A*	7.30	0.14
Kangaroo Lake:					
0-8 cm	7.5 YR 2.5/2	10 YR 5/3	loamy sand	5.81	0.34
8-18 cm	7.5 YR 3/3	7.5 YR 5/4	sandy clay loam	6.79	0.24
18-28 cm	7.5 YR 3/4	10 YR 5/3	sandy clay loam	7.02	0.25
28-38 cm	7.5 YR 3/4	7.5 YR 4/4	clay loam	7.07	0.28
below 41 cm	7.5 YR 3/4	7.5 YR 5/4	clay loam	6.84	0.30

* N/A = Not available. This indicates that soil was too rocky to determine soil texture.

† Water content is reported as kg water per kg dry soil.

Table 2.2. Bulk density of soil.

Depth (cm)	Bulk Density (g/cm^3)
Scorpion Creek:	
0-10*	0.65
Kangaroo Lake:	
0-10*	1.16
10-20*	1.08

* Depth intervals do not match those of soil pit samples. Soil bulk density samples were collected adjacent to soil pits with a bulk density sampler.

Table 2.3. Bulk density of rock cores.

Depth (m)	Bulk Density (g/cm^3)	Uncertainty* (g/cm^3)
Scorpion Creek:		
0.13-0.15	2.59	0.16
0.15-0.22	2.99	0.50
0.22-0.30	2.40	0.27
0.30-0.47	3.86	0.55
0.47-0.57	2.50	0.36
0.57-0.70	2.63	0.04
0.70-0.76	2.50	0.05
0.76	2.51	0.36
0.76 (2nd)	2.65	0.19
Kangaroo Lake:		
0.10-0.20	2.34	0.33
0.20-0.27	3.06	0.10
0.27-0.41	2.43	0.27
0.41-0.43	2.55	0.12
0.43-0.50	2.80	0.20
0.50-0.57	2.48	0.15
0.57-0.66	2.63	0.20
0.66-0.76	2.64	0.04
0.76-0.86	2.58	0.03
0.86-1.09	2.68	0.04
1.09-1.22	2.59	0.10
1.22-1.35	2.69	0.06

* Uncertainty values were determined through error propagation of all uncertainties in measuring rock core bulk density.

Table 2.4. Percent silt- and clay-sized fractions from soil.

Depth	Silt Fraction (%)*	Clay Fraction (%)*
Scorpion Creek:		
0-10 cm	11.57	6.72
10-20 cm	6.54	6.57
30-40 cm	4.98	3.34
Kangaroo Lake:		
0-8 cm	25.09	6.89
8-18 cm	27.66	9.27
18-28 cm	25.44	12.76
28-38 cm	23.86	14.48
below 41 cm	N/A	N/A

* Percent silt- and clay-fractions of the soil were calculated by dividing the measured weight of the dried silt- and clay-sized fractions, respectively, by the total weight of the dry soil, as calculated from measured water content values.

N/A = Not applicable because there was not enough sample remaining to separate the silt- and clay-sized fractions.

Table 2.5. Mineralogy of soil and rock samples determined by XRD*.

Sample	Bulk Fraction	Silt Fraction (63-2 μm)	Clay Fraction (< 2 μm)
Scorpion Creek Soil:			
0-10 cm	Lz, Mag, Clc, Qz	Lz, Mag, Clc, Qz	Lz, Clc, Qz
10-20 cm	Lz, Mag, Clc	Lz, Mag, Clc, Qz	Lz, Clc
30-40 cm	Lz, Mag, Clc	Lz, Mag, Clc	Lz, Clc
Scorpion Creek Rock:			
30-47 cm	Lz, Mag, Clc	N/A	N/A
47-57 cm	Lz, Mag	N/A	N/A
57-70 cm	Lz, Mag, Clc	N/A	N/A
70-76 cm	Lz, Mag, Clc	N/A	N/A
Kangaroo Lake Soil:			
0-8 cm	Lz, Clc, Tr, Tlc, Pl, Qz	Lz, Clc, Tr, Tlc, Pl, Qz	Lz, Clc, Tr, Tlc, Qz
8-18 cm	Lz, Clc, Tr, Tlc, Pl, Qz	Lz, Clc, Tr, Tlc, Pl, Qz	Lz, Clc, Tr, Tlc, Qz
18-28 cm	Lz, Clc, Tr, Tlc, Pl, Qz	Lz, Clc, Tr, Tlc, Pl, Qz	Lz, Clc, Tr, Tlc, Qz
28-38 cm	Lz, Clc, Tr, Tlc, Pl, Qz	Lz, Clc, Tr, Tlc, Pl	Lz, Clc, Tr, Tlc, Qz
below 41 cm	Lz, Clc, Tr, Tlc, Pl, Qz, Mag	N/A†	N/A†
Kangaroo Lake Rock:			
27-41 cm	Lz, Clc, Zr-oxide, PbCrMb-oxide	N/A	N/A
57-66 cm	Lz, Clc	N/A	N/A
86-109 cm	Lz, Brc	N/A	N/A
122-135 cm	Lz, Tr	N/A	N/A

* Mineral abbreviations from Whitney and Evans (2010). Abbreviations: Brc = brucite, Clc = clinochlore, Lz = lizardite, Mag = magnetite, Pl = plagioclase, Qz = quartz, Tlc = talc, Tr = tremolite.

N/A = Not applicable.

† Not enough sample remaining to separate the silt- and clay-sized fractions.

Table 2.6. Scorpion Creek chemical analysis of major elements with XRF.

Major Elements	Scorpion Creek Soil			Scorpion Creek Rock			
(wt. %)	0-10 cm	10-20 cm	30-40 cm	30-47 cm	47-57 cm	57-70 cm	70-76 cm
SiO_2	43.49	44.29	44.46	39.36	39.39	41.54	43.77
Al_2O_3	4.62	1.45	1.27	10.53	10.47	5.19	3.90
TiO_2	0.123	0.059	0.05	0.059	0.049	0.065	0.057
Fe_2O_3	13.36	12.24	12.27	9.94	9.18	11.59	8.64
MgO	35.84	41.17	42.53	38.49	36.90	40.03	42.71
Na_2O	0.95	0.29	0.12	0.15	0.08	0.17	0.16
K_2O	0.24	0.08	BD	BD	BD	BD	BD
MnO	0.164	0.064	0.080	0.226	0.352	0.167	0.140
CaO	0.87	0.11	0.06	0.11	2.06	0.81	0.05
P_2O_5	0.082	0.024	0.013	0.005	0.006	0.003	0.004
Total	99.74	99.78	100.85	98.87	98.49	99.57	99.43

BD = Below detection.

Table 2.7. Scorpion Creek chemical analysis of trace elements with XRF.

Trace Elements	Scorpion Creek Soil			Scorpion Creek Rock			
(ppm)	0-10 cm	10-20 cm	30-40 cm	30-47 cm	47-57 cm	57-70 cm	70-76 cm
Sc	3	2	2	24	14	19	10
V	69	51	49	103	47	48	55
Ni	2440	2832	2827	1383	988	1388	1337
Cu	5	7	8	BD	2	1	2
Ga	BD	BD	2	5	3	2	2
Rb	BD	BD	BD	BD	1	1	1
Sr	BD	BD	BD	1	4	3	2
Y	BD	BD	BD	BD	BD	BD	BD
Zr	BD	BD	BD	1	BD	1	BD
Nb	BD	BD	BD	BD	BD	BD	BD
Ba	BD	BD	BD	BD	BD	BD	BD
La	BD	BD	BD	BD	6	9	5
Hf	BD	BD	BD	BD	BD	BD	BD
Pb	BD	BD	BD	BD	1	2	BD
Th	BD	BD	BD	BD	BD	BD	BD
U	BD	1.4	2.3	2	1	1	1

BD = Below detection.

Table 2.8. Kangaroo Lake chemical analysis of major elements with XRF.

Major Elements	Kangaroo Lake Soil					Kangaroo Lake Rock			
(wt. %)	0-8 cm	8-18 cm	18-28 cm	28-38 cm	below 41 cm	27-41 cm	57-66 cm	86-109 cm	122-135 cm
SiO_2	47.55	47.18	48.08	47.41	45.57	45.50	46.21	45.90	46.72
Al_2O_3	10.06	9.38	9.64	9.15	6.73	3.06	2.27	2.17	2.43
TiO_2	0.410	0.388	0.379	0.345	0.257	0.116	0.092	0.083	0.073
Fe_2O_3	12.97	12.54	12.88	13.87	15.79	9.43	9.16	8.69	7.96
MgO	23.75	25.71	25.32	24.95	27.43	40.08	40.47	42.02	40.24
Na_2O	3.17	0.82	0.67	0.50	0.46	0.49	0.18	0.21	0.28
K_2O	0.49	0.21	0.23	0.22	0.17	0.03	BD	0.02	0.01
MnO	0.269	0.254	0.197	0.202	0.186	0.105	0.100	0.099	0.097
CaO	3.66	3.04	2.73	2.31	1.46	0.93	0.78	0.86	1.09
P_2O_5	0.310	0.076	0.050	0.054	0.039	0.004	0.004	0.004	0.003
Total	102.64	99.6	100.18	99.01	98.09	99.75	99.27	100.06	98.90

BD = Below detection.

Table 2.9. Kangaroo Lake chemical analysis of trace elements with XRF.

Trace Elements	Kangaroo Lake Soil					Kangaroo Lake Rock			
(ppm)	0-8 cm	8-18 cm	18-28 cm	28-38 cm	below 41 cm	27-41 cm	57-66 cm	86-109 cm	122-135 cm
Sc	17	15	21	21	13	13	9	10	10
V	88	91	117	114	83	62	40	43	46
Ni	2311	2291	2152	2306	2463	2379	2225	2116	2186
Cu	46	45	39	47	47	22	9	10	21
Ga	6	5	8	8	7	2	1	3	2
Rb	9	8	10	19	9	1	1	1	2
Sr	25	25	48	39	28	4	3	4	3
Y	BD	BD	BD	BD	BD	BD	BD	BD	BD
Zr	23	22	41	35	25	2	2	1	1
Nb	BD	BD	BD	BD	BD	1	1	1	BD
Ba	54	65	91	79	60	BD	BD	BD	BD
La	BD	BD	BD	BD	BD	3	2	5	9
Hf	BD	BD	BD	8	BD	BD	BD	BD	BD
Pb	BD	BD	5	BD	BD	1	2	1	2
Th	BD	BD	BD	BD	BD	BD	BD	BD	BD
U	1.8	2.4	BD	1.4	1.1	BD	1	BD	2

BD = Below detection.

Table 2.10. IRB-BART™ results for Scorpion Creek and Kangaroo Lake soils and rock cores.

Depth	IRB-BART (+/-)	Visible Reaction	Day of Reaction
Scorpion Creek Soil:			
0-10 cm	+	brown ring	24
10-20 cm	-	-	-
30-40 cm	-	-	-
Scorpion Creek Rock:			
13-15 cm	+[#]	brown ring	52
30-47 cm	-	-	-
47-57 cm	-	-	-
57-70 cm	-	-	-
70-76 cm	-	-	-
76 cm	-[#]		
Kangaroo Lake Soil:			
0-8 cm	-	-	-
8-18 cm	+	brown ring	24
18-28 cm	-	-	-
28-38 cm	-*	-	-
below 41 cm	-*	-	-
Kangaroo Lake Rock:			
20-27 cm	-	-	-
27-41 cm	-	-	-
41-43 cm	-	-	-
50-57 cm	-	-	-
57-66 cm	-	-	-
76-86 cm	+[#]	brown ring	73
86-109 cm	-	-	-
109-122 cm	-	-	-
122-135 cm	-	-	-

+ Indicates a positive reaction for iron-related bacteria based on a visible reaction including brown rings, brown gel, and/or brown clouds.

- Indicates a negative reaction for iron-related bacteria.

* A yellow-green residue began to form between days 10 and 30, however, the meaning of such reaction is unknown.

[#] Foam formed around the floating ball between days 7 and 9, which may indicate the presence of anaerobic bacteria

Table 2.11. Results of chrome azurol S universal siderophore assay in soil pore waters.

	Absorbance*			Concentration	
Sample	**Average**	**SD**	**n**	**Water (µM)†**	**Soil (µmol dm^{-3})‡**
Standards:					
Blank (DI water)	0.000	0.000	4	-	-
0 µM DFAM	1.055	0.020	12	-	-
1 µM DFAM	1.054	0.007	12	-	-
5 µM DFAM	1.010	0.034	12	-	-
10 µM DFAM	0.983	0.040	12	-	-
15 µM DFAM	0.976	0.044	12	-	-
20 µM DFAM	0.961	0.052	12	-	-
Scorpion Creek:					
0-10 cm	1.021	0.006	12	5.688	2.302
10-20 cm	1.020	0.024	12	5.896	2.202
30-40 cm	1.055	0.013	12	BD	BD
Kangaroo Lake:					
0-8 cm	1.202	0.034	12	BD	BD
8-18 cm	1.126	0.020	12	BD	BD
18-28 cm	1.029	0.007	12	3.934	1.575
28-38 cm	1.068	0.013	12	BD	BD
below 41 cm	1.039	0.010	12	1.764	0.732

*UV-absorbance was measured at 630 nm wavelength. Average is the mean of all instrument readings taken at 2-hour intervals over 6 hours. SD is the standard deviation of the measurements. *n* is the number of measurements. Except for blanks, each sample was measured 3 times at each 2-hour interval over 6 hours. DFAM is the commercially available siderophore deferoxamine mesylate.

†Water concentrations (in µM) were estimated from the standard curve, assuming a siderophore similar in strength to DFAM. See Appendix B.

‡Soil concentrations (in µmol dm^{-3}) were estimated from using water siderophore concentrations, water content, and soil bulk density to obtain units similar to that of Hersman et al. (1995).

BD = below detection.

Table 2.12. UV-Absorbance for organic constituents in soil pore waters.

	Absorbance*		
Sample	**Average**	**SD**	**n**
Scorpion Creek:			
0-10 cm	0.294	0.004	2
10-20 cm	0.187	0.004	2
30-40 cm	0.118	0.001	3
Kangaroo Lake:			
0-8 cm	1.306	0.021	3
8-18 cm	0.807	0.001	3
18-28 cm	0.188	0.004	3
28-38 cm	0.160	0.001	3
below 41 cm	0.297	0.001	3

* UV-absorbance was measured at 253.7 nm wavelength. Average is the mean of duplicate or triplicate instrument readings. SD is the standard deviation of the measurements. *n* is the number of measurements. A cuvette containing only DI water was measured for the blank.

CHAPTER 3

CHEMICAL WEATHERING OF OLIVINE AT BLACK ROCK FLOW, LUNAR CRATER, NEVADA

Introduction

Chemical weathering is a critical process that plays a key role in controlling the geochemistry of natural waters, the cycling of atmospheric carbon dioxide, and in rates of soil formation. Silicate weathering, in particular, is important because approximately 92 weight percent of the Earth's crust is composed of silicate minerals. Many studies have examined olivine dissolution (Blum and Lasaga, 1988; Brady and Walther, 1989; Grandstaff, 1980; Grandstaff, 1986; Oelkers, 2001; Pokrovsky and Schott, 2000; Rosso and Rimstidt, 2000; Siegel and Pfannkuch, 1984; Wogelius and Walther, 1991; Wogelius and Walther, 1992) as a model mineral, however few have examined its dissolution in an arid environment.

The mafic mineral olivine dissolves quickly in comparison to other silicate minerals due to its relatively simple mineral structure that contains isolated silica tetrahedra (Goldich, 1938; Schott & Berner 1983; Pokrovsky & Schott, 2000). As a result, olivine has been widely used as a model mineral for laboratory dissolution studies under a variety of conditions (Figure 3.1). Dissolution features as a result of chemical weathering, such as etch pits, have been thoroughly characterized on naturally-weathered olivine (Velbel and Ranck, 2008; Velbel, 2009; Nowicki and Velbel, 2011). Despite the extensive body of work on olivine dissolution kinetics in the laboratory, and olivine etch pit formation, few studies have examined olivine dissolution rates in the field (Figure 3.1; Schnoor, 1990), particularly under arid conditions. Therefore, in order to measure field

rates of olivine dissolution under arid conditions, etch pit volume and surface area was quantified on dated rock flows at Black Rock Flow, Nevada.

Geologic Setting

Black Rock Flow (also mentioned in the literature as Marcath Flow; Bergman et al., 1981; Dickson, 1997) is a basaltic lava flow located just north of U.S. Highway 6 in northern Nye County, Nevada (Figure 3.2). Black Rock Flow is located within the Lunar Crater Volcanic Field, a north-northeast trending belt composed of Late Cenozoic alkali basalts (Bergman et al., 1981). The Lunar Crater Volcanic Field is approximately 10 km wide and 100 km long, and extends from the Reveille Range to the Pancake Range (Bergman et al., 1981; Dickson, 1997).

The most recent eruption in the Lunar Crater Volcanic Field formed Black Rock Flow. Shepard et al. (1995) dated the surface of Black Rock Flow at 38 +/- 10 ka using ^{36}Cl and ^{10}Be cosmogenic nuclides. This age (~38 ka) provides a constraint for the amount of time the flow has been subject to weathering. Black Rock Flow contains phenocrysts of anorthoclase, olivine, and hornblende, and also xenoliths of lherzolite and dunite (Stickney, 2004). The dunite xenoliths have been observed up to 3 cm in size (Stickney, 2004).

The Black Rock Flow area currently has an arid continental climate and receives 12 cm of mean annual precipitation (Dohrenwend et al., 1987). Approximately 45,000 years ago, south-central Nevada experienced drier, cooler summers and winters with roughly 20% more precipitation than current levels (Spaulding, 1985). Roughly 30,000 years ago, temperatures were probably 3-6°C cooler than present temperatures

(Spaulding, 1985). By 18,000 years ago, average annual precipitation likely was not more than 40% of current quantities (Spaulding, 1985). Post-glacial warming trends began, and around 10,000 years ago the mean annual temperatures in south-central Nevada neared current values (Spaulding, 1985).

Objectives and Hypotheses

Despite an extensive literature of laboratory olivine dissolution experiments, and qualitative observations of field olivine weathering, few studies have examined olivine dissolution rates in the field (e.g. Schnoor, 1990; Figure 3.1), and none, to the author's knowledge, under arid conditions. Therefore, the purpose of this study is to determine the dissolution rate and weathering products of olivine in a natural field setting in a desert environment. It is hypothesized that the weathering rate measured will be orders of magnitude slower than published laboratory dissolution rates due to the laboratory-field discrepancy (White and Brantley, 2003) and the arid climate.

Methods

Sample Collection and Preparation

Samples of basalt containing dunite xenoliths were collected from Black Rock Flow using a rock hammer. The samples were selected from outcrops rather than loose pieces in order to reduce the possibility that the basalt surface had been moved since its original exposure. Black Rock Flow has two lobes, which will be referred to as the north lobe and south lobe (Figure 3.2). Samples were collected from both the north lobe (approximately 38°29.823 N, 116°00.243 W) and the south lobe (approximately

38°28.535 N, 116°00.553 W). Hand samples were then cut into smaller sizes on a rock saw without water, to avoid any potential dissolution of salts. More precise cuts to isolate the olivine xenoliths were made on an IsoMet saw with ethanol. Samples were then rinsed and sonicated (Branson Ultrasonic Cleaner, Model 2510) in ethanol to remove basalt dust residue from cutting but to avoid potential dissolution of any water-soluble secondary minerals.

Scanning Electron Microscopy

The surfaces of the olivine xenoliths were carbon-coated and analyzed using scanning electron microscopy (SEM) to identify dissolution etch pits and energy dispersive spectroscopy (EDS) to measure chemical composition of the samples using a JEOL scanning electron microscope model JSM-5610 at the UNLV Electron Microanalysis and Imagine Laboratory (EMiL). Due to the unpolished surfaces, EDS measurements are semi-quantitative.

Results

Field and Hand Sample Observations

Eight samples of basalt containing nine dunite xenoliths, ranging in size from 1.2-3.0 cm in diameter, were collected from Black Rock Flow (Table 3.1). Five of the basalt samples were collected from the north lobe of the basalt flow, and three were collected from the south lobe. All five basalt samples from the north lobe are vesicular basalt, whereas two of the three from the south lobe are non-vesicular (Figure 3.3). The two dunite xenoliths within the non-vesicular basalt appear concave compared to the

surrounding basalt surface, whereas the xenoliths within the vesicular basalt are more even with the surrounding basalt surface (Figure 3.3). Most of the dunite xenoliths appear to be granular with some reddish staining (Figure 3.4a). However, some dunite xenoliths appear to be relatively smooth and green without reddish staining (Figure 3.4b).

Scanning Electron Microscopy

Seven of the original nine dunite xenoliths were observed using SEM—two samples could not be observed due to the concave surfaces. Etch pits were identified on the surfaces of four of the seven dunite xenoliths that were observed using SEM (Figures 3.5 and 3.6). The apparent etch pits are approximately diamond-shaped (Figure 3.6) and vary in size from approximately 1.4-8.2 microns in diameter. The average diameter of the 75 etch pits measured is 3.7 microns. The etch pits, if present, may appear isolated or side-by-side, and they also seem to be oriented in the same direction (Figure 3.6). In addition, some areas where etch pits were not observed appear to have a coating on the surface that contains manganese as measured by EDS (Figure 3.7).

Discussion

Alteration in the form of reddish staining was visible on olivine-rich xenoliths in most of the hand samples. The reddish staining, presumably iron oxides, is especially evident along fractures or grain boundaries where weathering fluids would be able to penetrate the mineral. Also, the texture of the basalt seems to play a role in the weathering of the dunite surface with respect to the basalt surface. It appears that the non-vesicular basalt is more resistant to weathering relative to the dunite, as shown by the

concave shape of the dunite surfaces. In contrast, the dunite surfaces within the vesicular basalt seem to weather at a similar pace given the relatively smooth transition from the basalt to the dunite surface.

Apparent diamond-shaped etch pits were observed on four of the xenoliths analyzed from Black Rock Flow, Nevada (Figures 3.5 and 3.6). These etch pits appear to be similar to etch pits identified on naturally-weathered olivine surfaces from Hawaii, North Carolina, and Georgia (Velbel, 2009; Nowicki and Velbel, 2011). According to Velbel (2009), etch pits are not a pre-weathering characteristic, but rather an indication that chemical weathering has occurred. Therefore, olivine weathering in an arid environment apparently consists of etch pit formation comparable to etch pit formation on olivine in more humid environments. This is consistent with previous assertions that etch pits formed on olivine have similar geometries regardless of differences in the age of the surface, crystallization history, and regolith history (Velbel and Ranck, 2008; Velbel, 2009). Although the etch pits identified in this study appear less distinct than those identified in Velbel (2009) and Nowicki and Velbel (2011), the pits appear to share similar geometries.

Velbel (2009) has extensively studied the geometries of etch pits on naturally-weathered olivine surfaces using SEM. Diamond-shaped etch pits, according to Velbel (2009), are actually a cross-sectional view of two conical etch pits joined base-to-base. Nowicki and Velbel (2011) determined an empirical ratio of radius-to-height of 1.78 for such diamond-shaped etch pits. The relationships stated in Nowicki and Velbel (2011) can be applied to calculate volumes and surface areas of etch pits using the geometries observed in the apparent etch pits on dunite xenoliths from Black Rock Flow, Nevada.

These measurements can then be used to calculate a mineral dissolution rate (Equation 3.1)

$$R = \frac{d}{tV} \qquad (Equation\ 3.1)$$

where R is the surface-area normalized dissolution rate (mol/m^{2}s), d is the total advance of the mineral surface (m), t is the time of exposure (s), and V is the molar volume of the mineral of interest (for forsterite: 4.3×10^{-5} m^3/mol). The rate, R, calculated from surface retreat in this manner is normalized to a geometric surface area. The field rate, R, can then be compared to laboratory dissolution rates normalized to BET surface areas by dividing by a roughness factor, in this case 5.4 (Rimstidt et al., in press). Gordon and Brady (2002) used a similar technique where the porosity, or weathered portion of an exposed basalt flow, was divided by the age of the basalt flow to determine weathering rates (in mol/cm^{2}s) of basaltic glass at McCartys flow at El Malpais, New Mexico.

Because the etch pits are a cross-section of two cones, the depth of an etch pit is not an accurate representation of the total advance of the mineral surface (d). Using the average diameter (3.7 μm) measured from 75 etch pits observed in SEM and the radius-to-height ratio from Nowicki and Velbel (2011), an average etch pit height of 1.04 μm was calculated. The radius and height were then used to estimate the average volume and surface area of the diamond-shaped etch pits. The average etch pit volume (m^3) was divided by the average surface area (m^2) to obtain a representative distance (m) for the advance of the mineral surface. It should be noted that not all dunite surfaces examined here contained etch pits, therefore this should be considered a maximum estimate of the advance of the mineral surface.

The time of exposure (*t*) is considered to be the exposure age for Black Rock Flow (38 +/- 10 ka, measured using cosmogenic nuclides by Shepard et al., 1995) making the assumption that this age accurately reflects the surface and that negligible physical removal of olivine etch pits has occurred. Measuring the ages of surfaces is difficult, and they are often constrained by the age of moraines, the age of flows (Hausrath et al., 2008a), and, when available, cosmogenic dating of the surface, as was used here. If physical erosion removed the surfaces, decreasing the size of the etch pits, then rates calculated represent minimum dissolution rates.

The forsterite dissolution rate measured from these etch pits, after adjusting for roughness, is 3.48×10^{-15} mol/m^{2}s, which is approximately four to five orders of magnitude slower than published laboratory dissolution rates at a pH of ~7-9 (Figure 3.1). Due to the arid environment at Black Rock Flow, pH of weathering fluids was not measured; a pH of ~7-9 is estimated based on pH measurements of a similar olivine-rich basaltic regolith at Sverrefjell Volcano in the polar desert Svalbard (Hausrath et al., 2008a; Hausrath et al., 2008b). The rate determined in this study is also approximately 1.5 orders of magnitude slower than the field dissolution rate published in Schnoor (1990) for pH ~5.4 (Figure 3.1), most likely due to the arid climate and higher pH.

Conclusions

Evidence of chemical weathering, specifically diamond-shaped etch pits, were observed through SEM on four of the dunite xenoliths obtained from Black Rock Flow, Nevada. Olivine weathering in an arid environment apparently consists of etch pit formation comparable to etch pit formation on olivine observed in previous studies

(Velbel (2009); Nowicki and Velbel, 2011) in more humid environments. Other signs of weathering were also observed, such as possible iron-oxidation on some surfaces as well as concave surfaces on some xenoliths relative to the surrounding basalt. Rock coatings containing manganese were also observed on some surfaces in areas where etch pits were not observed. A field dissolution rate of 3.48×10^{-15} mol/m^{2}s for forsterite was measured. This rate, as hypothesized, is several orders of magnitude slower than published laboratory dissolution rates at a similar pH.

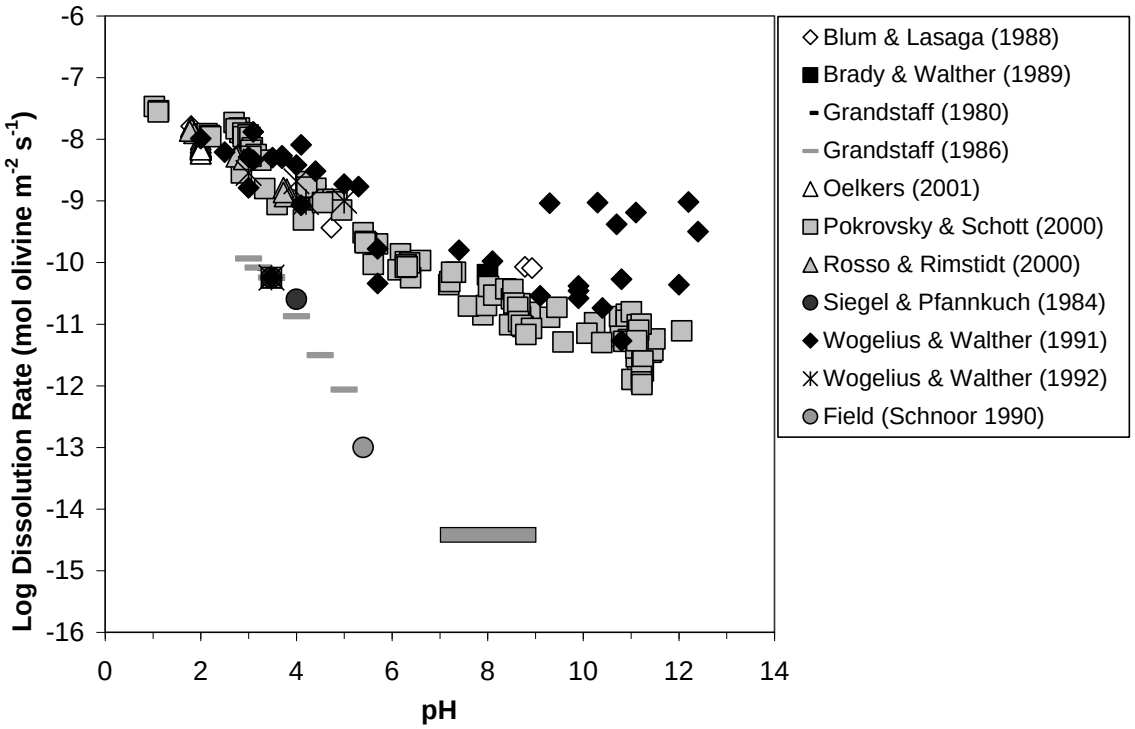

Figure 3.1. Olivine (forsterite) dissolution rates determined in the laboratory (at 298 K) and one field dissolution rate determined in a watershed study. Note the several orders of magnitude discrepancy between the field rates and the laboratory rates. The shaded gray box indicates the rate calculated in this study, with vertical uncertainty based on the uncertainty of the Black Rock Flow exposure date (Shepard et al. 1995) and horizontal uncertainty from the estimated pH of ~7-9.

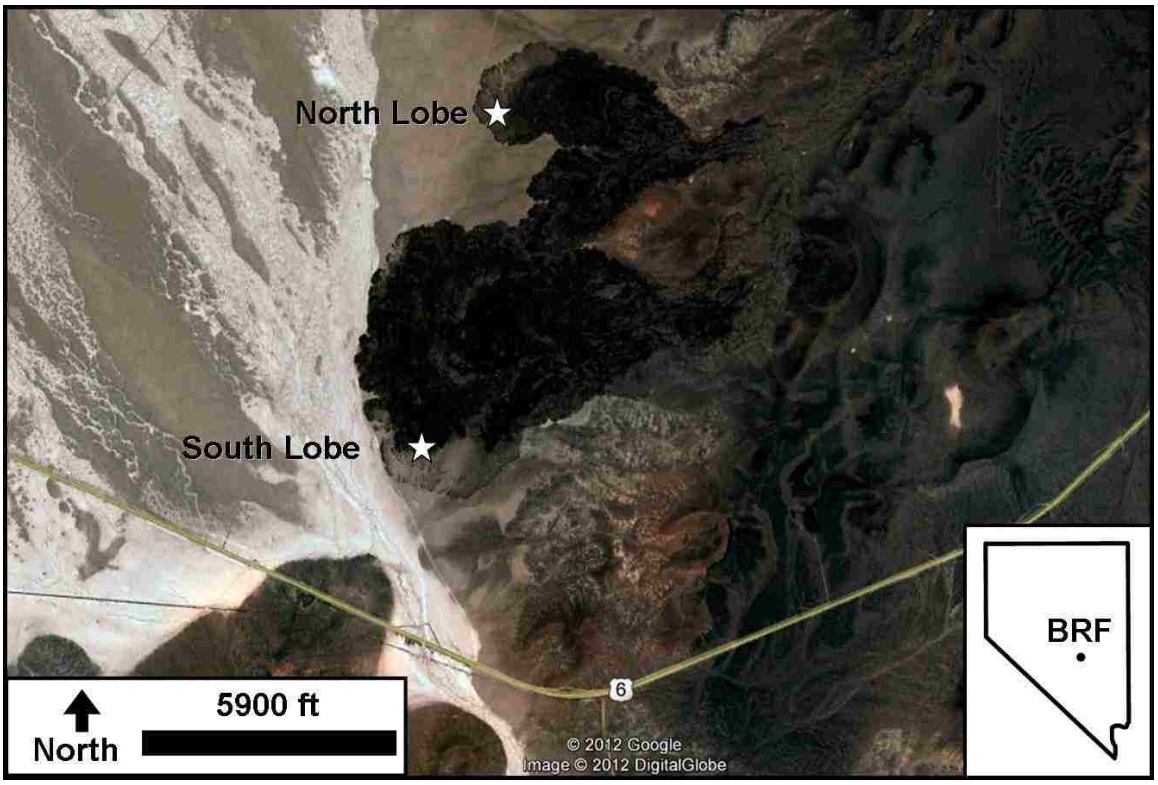

Figure 3.2. Google Earth image showing Black Rock Flow just north of U.S. Highway 6 in central Nevada. Stars on the north and south lobe of the basalt flow indicate approximate sampling locations.

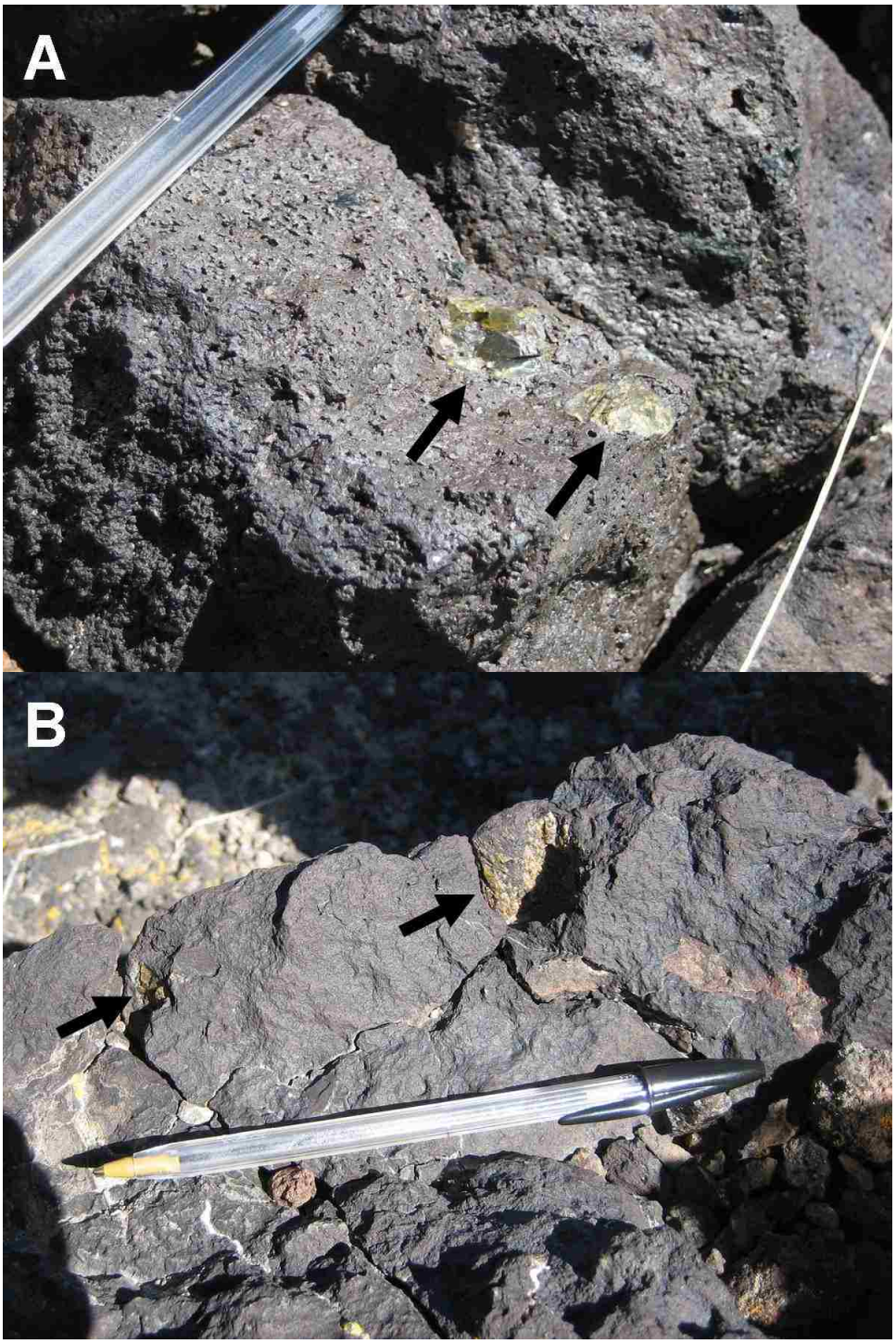

Figure 3.3. Photographs of dunite xenolith samples in place at Black Rock Flow, Nevada. Dunite xenoliths are denoted by black arrows. A) Samples collected from vesicular basalt on the north lobe of Black Rock Flow. The surfaces of the xenoliths are relatively even with the surrounding basalt surface. B) Samples collected from non-vesicular basalt on the south lobe of Black Rock Flow. The surfaces of these xenoliths appear to be concave in relation to the surrounding basalt surface. Please note the pen for scale in each image.

Figure 3.4. Photographs of dunite xenolith samples collected from Black Rock Flow, Nevada. A) Dunite xenolith displaying a more granular texture as well as reddish staining. B) Dunite xenolith displaying a relatively smoother surface without reddish staining. Please note the ruler for scale in each image.

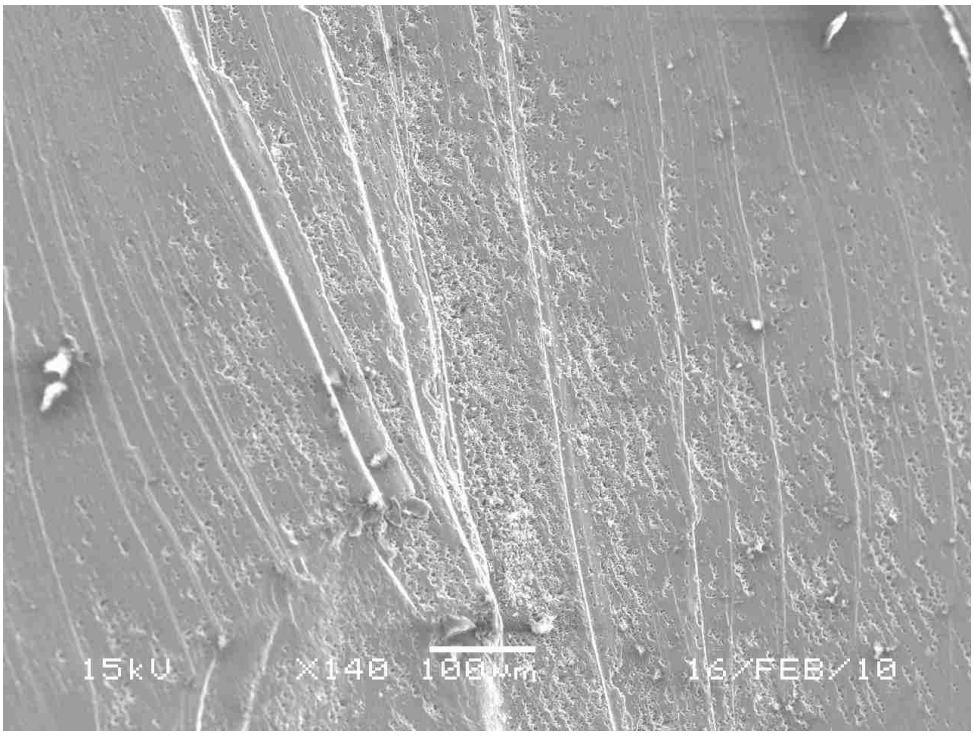

Figure 3.5. SEM micrograph of extensive area of pitting on a dunite xenolith surface. Scale bar is 100 microns.

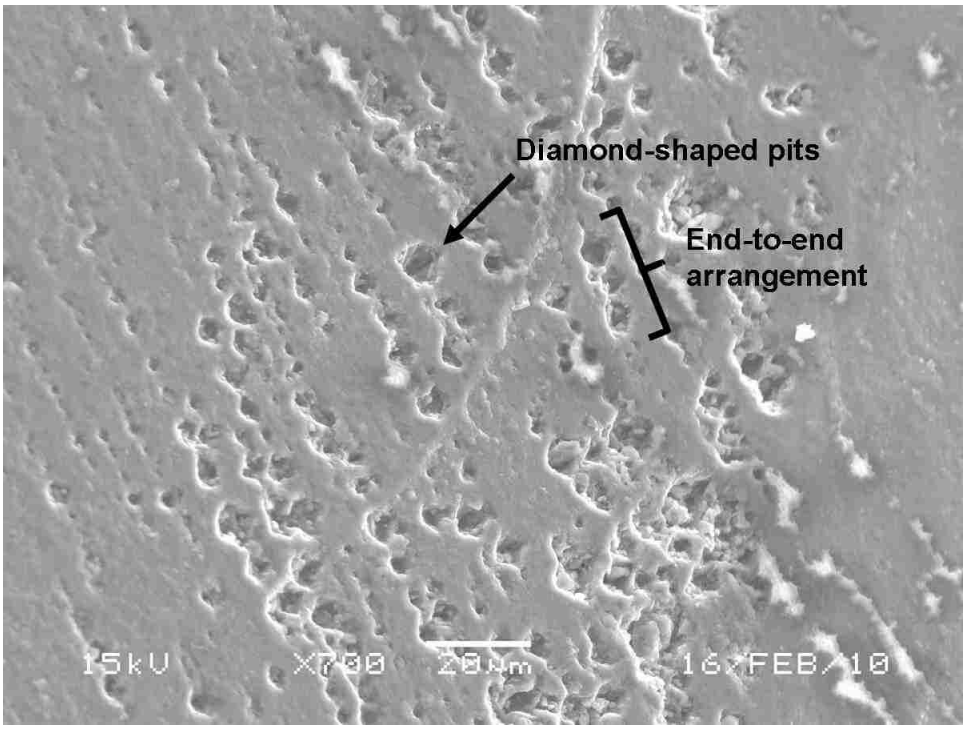

Figure 3.6. SEM micrograph of diamond-shaped etch pits on a dunite xenolith surface. Some pits are isolated while others are arranged end-to-end. However, all appear to share the same orientation. Scale bar is 20 microns.

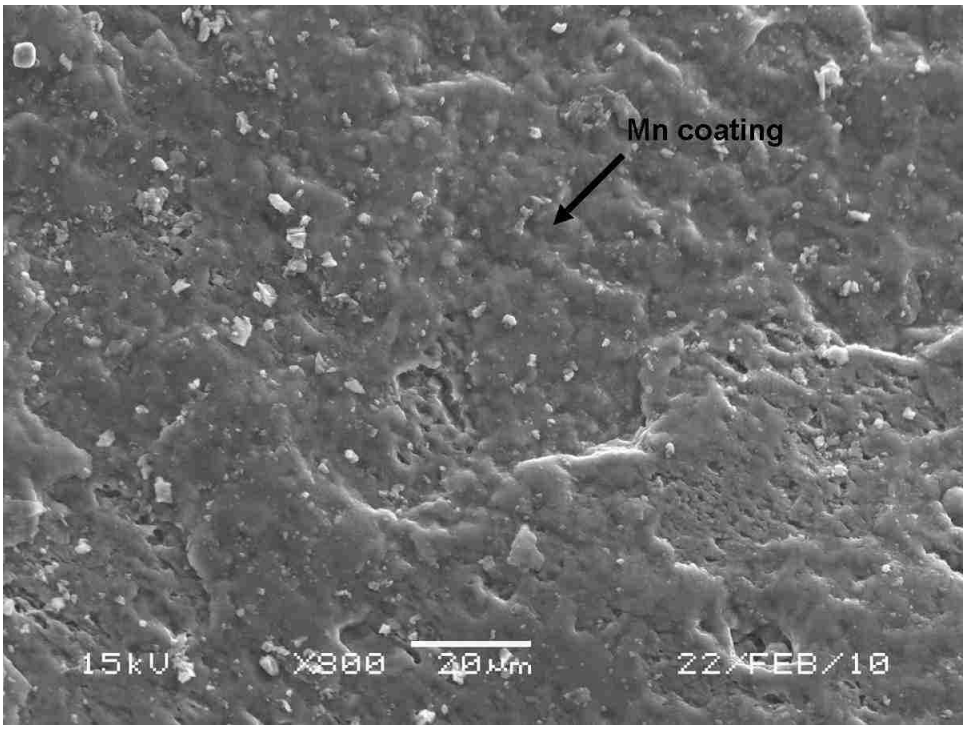

Figure 3.7. SEM micrograph of a manganese-containing rock coating on a dunite xenolith surface. Scale bar is 20 microns.

Tables

Table 3.1. Characteristics of dunite xenoliths collected from Black Rock Flow.

Sample	Lobe	Basalt Texture	Xenolith Diameter	Color	Etch Pits*
BRF1	North	vesicular	3 cm	reddish	no
BRF2	North	vesicular	3 cm	reddish	no
BRF3	North	vesicular	2 cm	green	yes
BRF4	North	vesicular	1.2 cm	green	yes
BRF5a	North	vesicular	1.9 cm	green	yes
BRF5b	North	vesicular	1.8 cm	green	yes
BRF6	South	non-vesicular	2.5 cm	reddish	N/A
BRF7	South	non-vesicular	1.3 cm	reddish	N/A
BRF8	South	vesicular	2 cm	reddish	no

* Yes or no denotes the presence or absence, respectively, of apparent diamond-shaped etch pits as determined by SEM analysis.

N/A = Not applicable because the surfaces of these samples were too concave to effectively perform SEM analysis.

APPENDIX A

KLAMATH MOUNTAINS SEM-EDS DATA

This appendix contains all of the SEM-EDS data for rock fragments found in soils and rock cores from Scorpion Creek and Kangaroo Lake. Samples were prepared as stated in the methods section of Chapter 2, and analyzed at the UNLV Electron Microanalysis and Imaging Laboratory (EMiL) using a JEOL scanning electron microscope model JSM-5610. Concentrations listed for each EDS spectra are in units of weight percent.

Scorpion Creek Soil: depth interval 0-10 cm

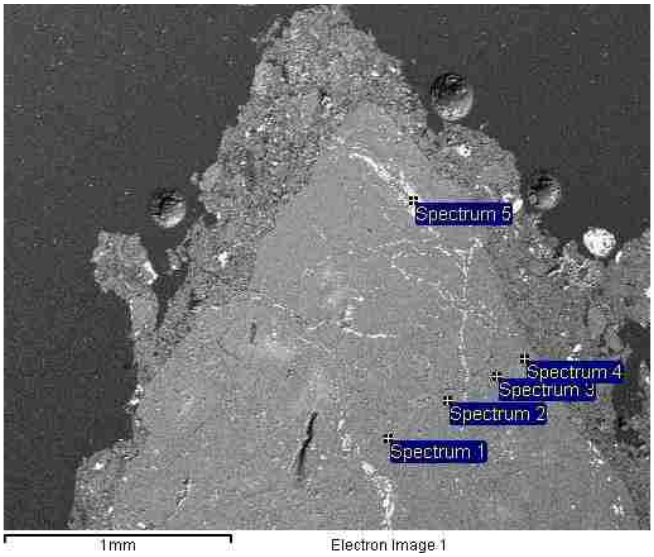

	(values in wt. %; if box is blank, it was below detection)				
Spectrum	**O**	**Mg**	**Si**	**Fe**	**Total**
Spectrum 1	50.22	24.32	21.67	3.8	100
Spectrum 2	51.64	24.17	20.86	3.33	100
Spectrum 3	48.74	24.48	22.72	4.06	100
Spectrum 4	53.36	24.1	20.43	2.11	100
Spectrum 5	32.53	2.84	1.95	62.68	100

Scorpion Creek Soil: depth interval 0-10 cm

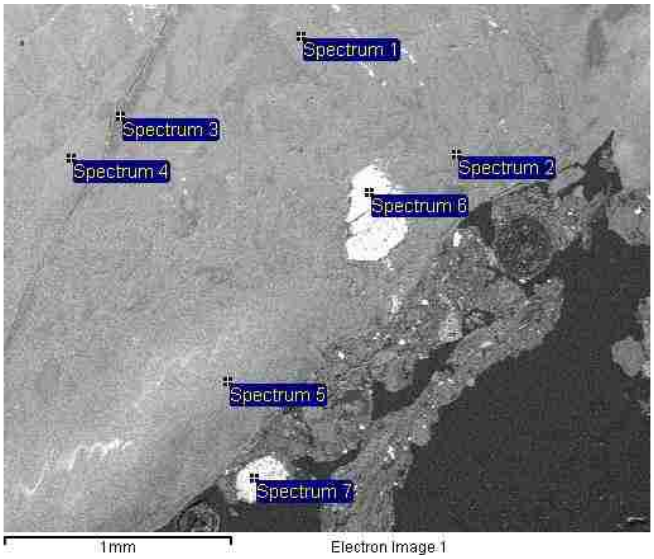

	(values in wt. %; if box is blank, it was below detection)									
Spectrum	**O**	**Mg**	**Al**	**Si**	**Cl**	**Cr**	**Mn**	**Fe**	**Zn**	**Total**
Spectrum 1	51.81	24.25		20.91				3.03		100
Spectrum 2	53.16	24.08		19.89				2.87		100
Spectrum 3	47.73	24.48		24.37	0.99			2.43		100
Spectrum 4	65.58	21.1		13.32						100
Spectrum 5	68.32	20.38		11.3						100
Spectrum 6	34.6	3.79	3.44	2.08		22.54	2.95	29.38	1.24	100
Spectrum 7	39.99	5	9.2			21.21	1	22.86	0.74	100

Scorpion Creek Soil: depth interval 0-10 cm

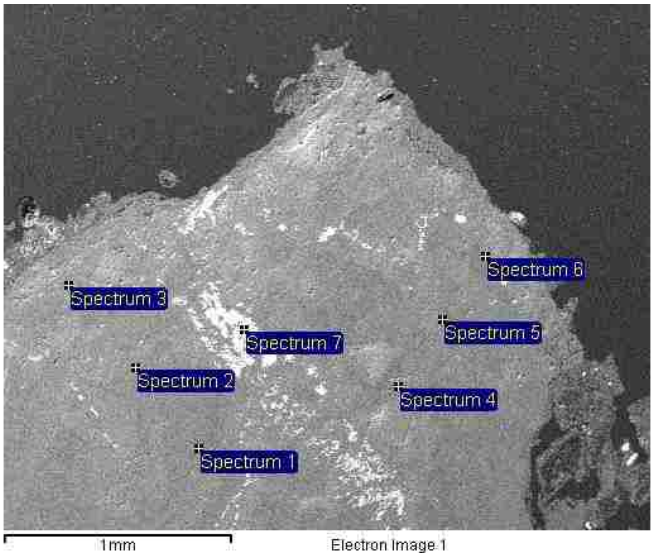

	(values in wt. %; if box is blank, it was below detection)					
Spectrum	**O**	**Mg**	**Si**	**Cl**	**Fe**	**Total**
Spectrum 1	48.39	24.69	23.05	0.61	3.26	100
Spectrum 2	51.01	24.61	21.16		3.22	100
Spectrum 3	50.35	24.61	21.68		3.36	100
Spectrum 4	52.08	23.68	21.2		3.03	100
Spectrum 5	52.16	24.44	20.51		2.89	100
Spectrum 6	49.79	24.38	22.35	0.34	3.15	100
Spectrum 7	29.11		0.69		70.2	100

Scorpion Creek Soil: depth interval 0-10 cm

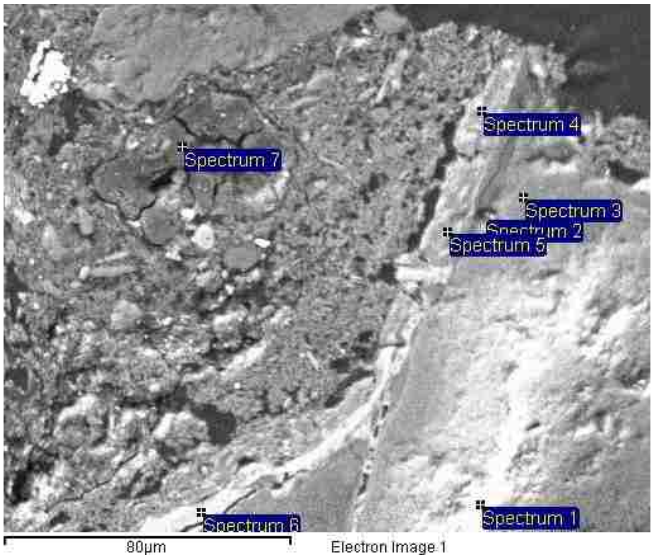

	(values in wt. %; if box is blank, it was below detection)									
Spectrum	**O**	**Mg**	**Al**	**Si**	**Ca**	**Mn**	**Fe**	**Co**	**Ni**	**Total**
Spectrum 1	58.2	22.74		18.52			0.53			100
Spectrum 2	48	24.68		24.96			2.36			100
Spectrum 3	48.52	24.96		24.33			2.2			100
Spectrum 4	41.62	8.58	6.21	17.74	0.82	7.39	13.93	1.69	2.02	100
Spectrum 5	47.96	10.47		18.23	1	5.72	13.11	1.48	2.03	100
Spectrum 6	43.02	5.38	5.36	6.72	0.56	22.31	6.69	4.21	5.75	100
Spectrum 7	53.03	9.44	3.41	4.36	11.73		18.03			100

Scorpion Creek Soil: depth interval 0-10 cm

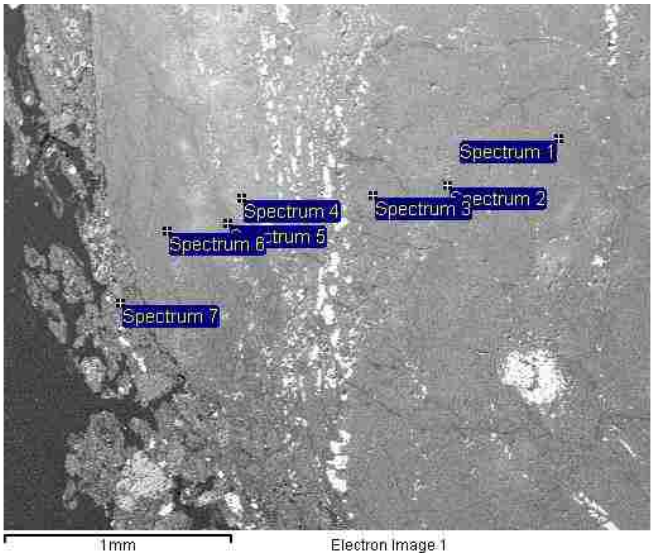

	(values in wt. %; if box is blank, it was below detection)						
Spectrum	**O**	**Mg**	**Si**	**Cl**	**Ca**	**Fe**	**Total**
Spectrum 1	50.9	24.34	21.58			3.18	100
Spectrum 2	50.92	24.36	21.23			3.49	100
Spectrum 3	51.6	24.45	20.61			3.33	100
Spectrum 4	63.02	21.64	15.02			0.32	100
Spectrum 5	48.43	25.14	23.49			2.94	100
Spectrum 6	49.13	24.85	22.79	0.36		2.87	100
Spectrum 7	48.86	21.02	20.36		1.25	8.52	100

Scorpion Creek Soil: depth interval 0-10 cm

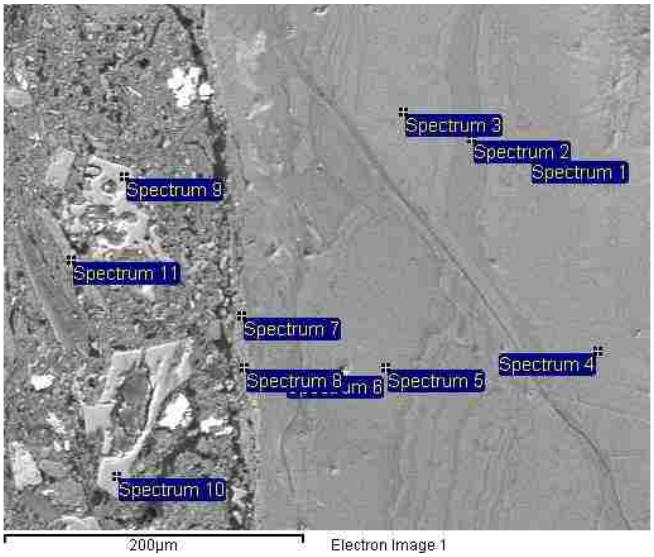

(values in wt. %; if box is blank, it was below detection)

Spectrum	O	Na	Mg	Al	Si	Cl	K	Ca	Mn	Fe	Co	Total
Spectrum 1	50.45		24.7		22.88					1.96		100
Spectrum 2	49.32		25.12		22.72	0.41				2.43		100
Spectrum 3	49.63		25.15		22.05	0.39				2.77		100
Spectrum 4	49.64		24.78		22.54	0.36				2.69		100
Spectrum 5	50.06		24.68		22.63	0.33				2.26		100
Spectrum 6	49.39		25.25		23.18					2.19		100
Spectrum 7	47.87		17.83		22.73				0.91	10.69		100
Spectrum 8	47.03		15.36		22.38			0.38	2.57	11.36	1	100
Spectrum 9	53.67	1.75		6.24	33.24		3.11	0.65		1.33		100
Spectrum 10	50.62	2.29		6.79	35.05		3.27	0.71		1.36		100
Spectrum 11	46.24		17.97		27.85	0.54				7.4		100

Scorpion Creek Soil: depth interval 0-10 cm

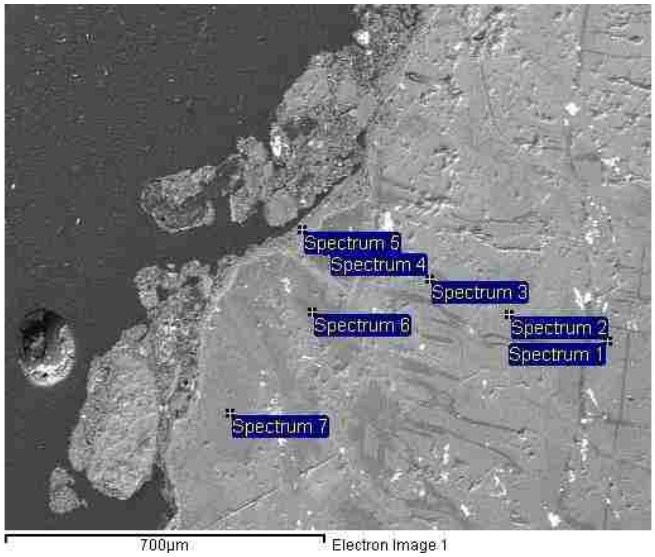

	(values in wt. %; if box is blank, it was below detection)						
Spectrum	**O**	**Mg**	**Si**	**Cl**	**Mn**	**Fe**	**Total**
Spectrum 1	50.11	24.34	22.23			3.33	100
Spectrum 2	50.25	24.57	21.81			3.37	100
Spectrum 3	50.57	24.89	21.45			3.09	100
Spectrum 4	46.82	24.69	24.74	1.13		2.62	100
Spectrum 5	45.55	19.76	22.63		1.56	10.51	100
Spectrum 6	46.94	24.27	25.19	1.02		2.58	100
Spectrum 7	48.8	25	23.25			2.95	100

Scorpion Creek Soil: depth interval 0-10 cm

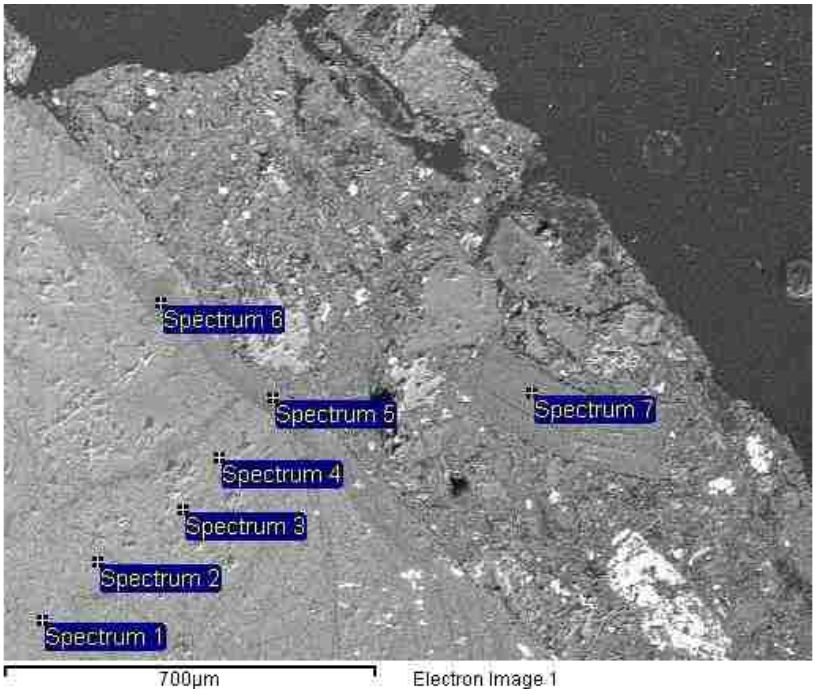

	(values in wt. %; if box is blank, it was below detection)							
Spectrum	**O**	**Mg**	**Si**	**Cl**	**Cr**	**Fe**	**Ni**	**Total**
Spectrum 1	51.24	24.67	20.66			3.43		100
Spectrum 2	48.77	24.71	22.65			3.87		100
Spectrum 3	51	23.75	21.47		0.48	3.3		100
Spectrum 4	51.91	23.44	20.88		0.68	3.09		100
Spectrum 5	47.51	24.23	23.94			4.32		100
Spectrum 6	45.1	25.61	24.47	1.2		2.99	0.64	100
Spectrum 7	48.28	25.47	24.28			1.98		100

Scorpion Creek Soil: depth interval 30-40 cm

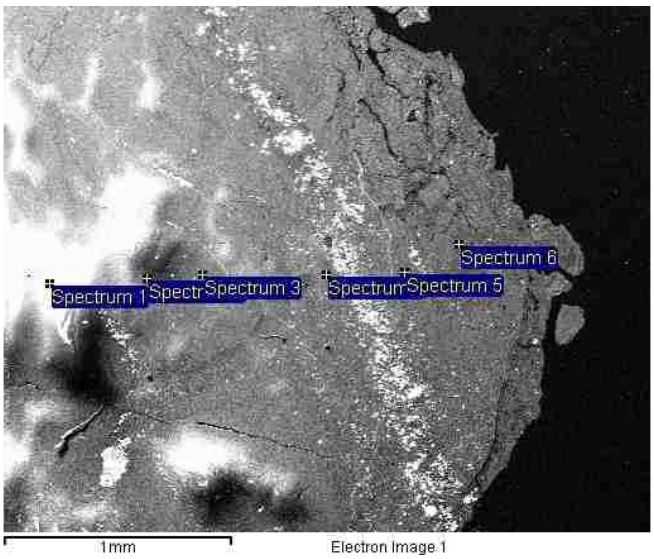

	(values in wt. %; if box is blank, it was below detection)					
Spectrum	**O**	**Mg**	**Si**	**Cl**	**Fe**	**Total**
Spectrum 1	71.96	18.74	9.3			100
Spectrum 2	58.93	23.24	16.86		0.97	100
Spectrum 3	49.26	25.13	22.31		3.29	100
Spectrum 4	48.16	24.23	23.52	0.45	3.64	100
Spectrum 5	48.86	24.17	22.68	0.53	3.77	100
Spectrum 6	50.3	24.37	22.05		3.28	100

Scorpion Creek Soil: depth interval 30-40 cm

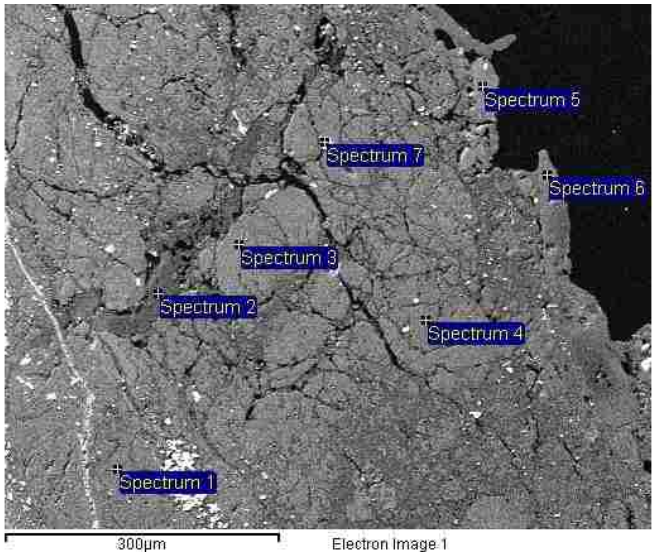

	(values in wt. %; if box is blank, it was below detection)							
Spectrum	**O**	**Mg**	**Si**	**Cl**	**Cr**	**Fe**	**Ni**	**Total**
Spectrum 1	48.74	24.44	22.6	0.45		3.78		100
Spectrum 2	45.26	25.97	26.23			2.54		100
Spectrum 3	49.94	24.67	21.88			3.51		100
Spectrum 4	48.39	24.69	23.04			3.89		100
Spectrum 5	50.83	24.52	22.13			2.52		100
Spectrum 6	48.72	24.84	24.19			2.24		100
Spectrum 7	39.26	4.43	7.58		1.13	45.52	2.07	100

Scorpion Creek Soil: depth interval 30-40 cm

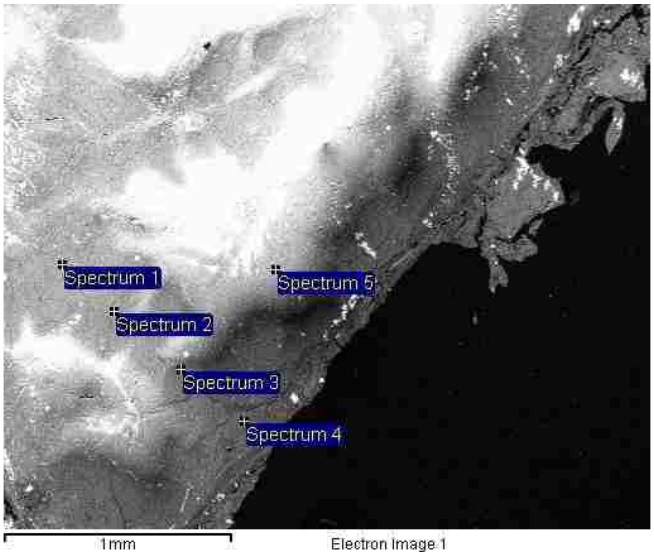

	(values in wt. %; if box is blank, it was below detection)					
Spectrum	**O**	**Mg**	**Si**	**Cl**	**Fe**	**Total**
Spectrum 1	50.02	24.76	22.3		2.92	100
Spectrum 2	51.3	24.39	21.04	0.44	2.82	100
Spectrum 3	51.31	24.78	20.83		3.07	100
Spectrum 4	48.95	25.05	22.65		3.35	100
Spectrum 5	77.81	13.54	8.65			100

Scorpion Creek Soil: depth interval 30-40 cm

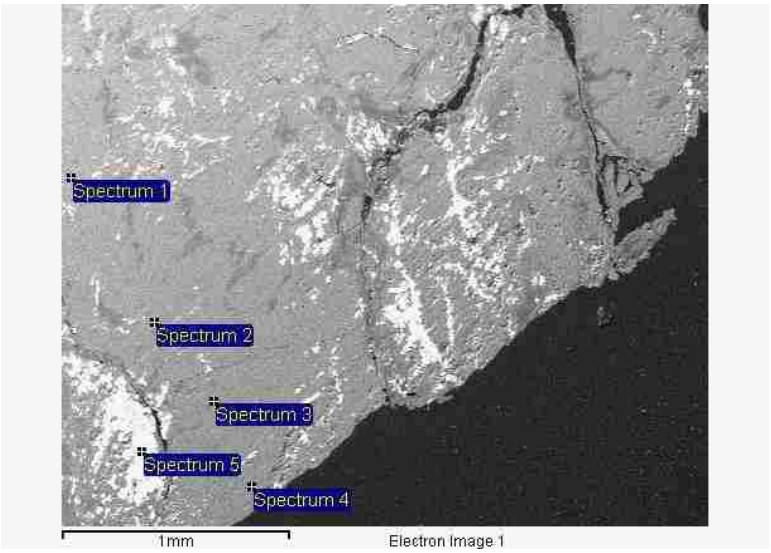

	(values in wt. %; if box is blank, it was below detection)				
Spectrum	**O**	**Mg**	**Si**	**Fe**	**Total**
Spectrum 1	51.86	24.87	21.76	1.5	100
Spectrum 2	51.37	24.98	22.21	1.44	100
Spectrum 3	51.51	24.86	22.03	1.6	100
Spectrum 4	51.55	25.12	22.05	1.28	100
Spectrum 5	33.28		0.62	66.1	100

Scorpion Creek Soil: depth interval 30-40 cm

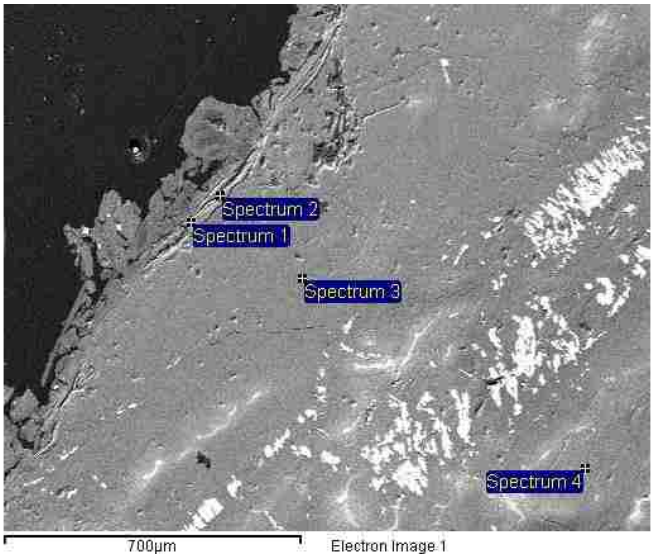

	(values in wt. %; if box is blank, it was below detection)								
Spectrum	**O**	**Mg**	**Al**	**Si**	**K**	**Ca**	**Ti**	**Fe**	**Total**
Spectrum 1	41.03	3.63	10.11	25.24		0.71		19.28	100
Spectrum 2	48.08	3.94	9.51	23.73	0.33	0.55	0.35	13.51	100
Spectrum 3	51.86	24.12		20.83				3.19	100
Spectrum 4	56.28	23.67		18.54				1.52	100

Scorpion Creek Soil: depth interval 30-40 cm

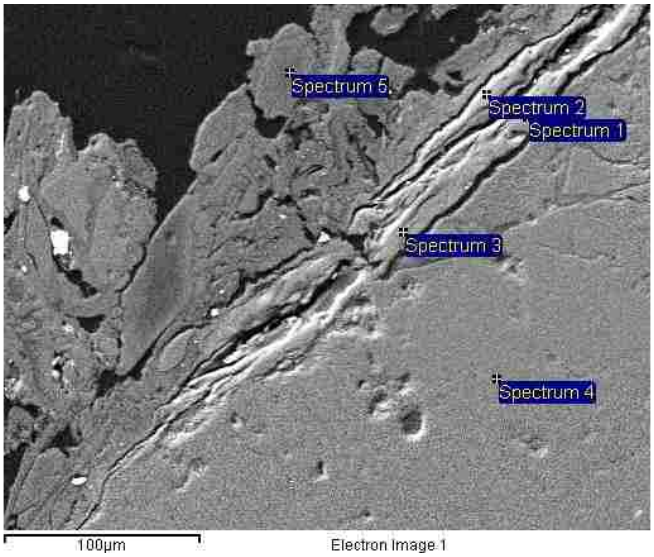

	(values in wt. %; if box is blank, it was below detection)						
Spectrum	**O**	**Mg**	**Al**	**Si**	**Ca**	**Fe**	**Total**
Spectrum 1	47.22	4.4	10.02	23.51	0.67	14.17	100
Spectrum 2	45.61	7.5	8.02	23.21	0.46	15.2	100
Spectrum 3	46.51	3.85	9.73	24.39	0.63	14.89	100
Spectrum 4	51.75	24.23		20.84		3.18	100
Spectrum 5	46.87	25.46		26.02		1.65	100

Scorpion Creek Soil: depth interval 30-40 cm

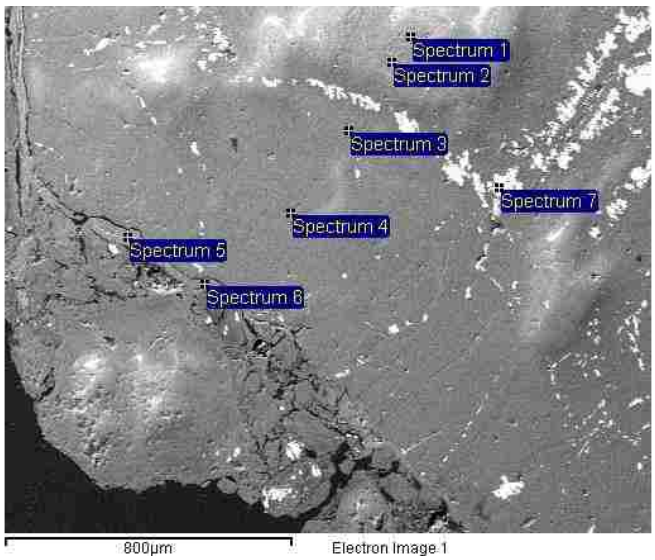

	(values in wt. %; if box is blank, it was below detection)								
Spectrum	**O**	**Mg**	**Al**	**Si**	**Ca**	**Ti**	**Fe**	**Ni**	**Total**
Spectrum 1	60.8	22.38		15.91			0.92		100
Spectrum 2	57.02	23.55		18.05			1.38		100
Spectrum 3	53.64	24.13		20.03			2.2		100
Spectrum 4	51.39	24.22		21.31			3.08		100
Spectrum 5	46.81	7.3	7.86	24.23	0.67		12.43	0.7	100
Spectrum 6	45.18	4.26	10.2	23.62	0.45	0.4	15.89		100
Spectrum 7	30.28	6.22		3.61			59.89		100

Scorpion Creek Rock Core: depth interval 30-47 cm

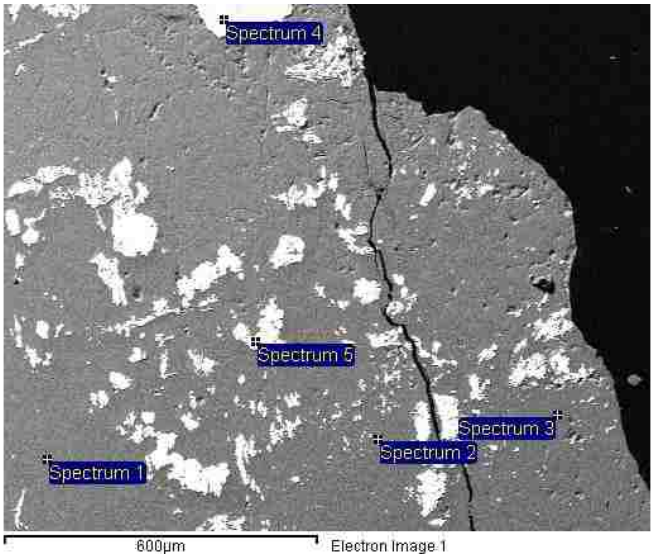

(values in wt. %; if box is blank, it was below detection)

Spectrum	O	Mg	Al	Si	Cr	Mn	Fe	Ni	Zn	Total
Spectrum 1	50.02	24.38	0.47	21.77			3.37			100
Spectrum 2	51.27	24.11	0.53	21.02			3.08			100
Spectrum 3	51.85	24	0.37	20.7			3.08			100
Spectrum 4	32.39	4.09	6.94	0.61	22.94	2.75	29.39		0.88	100
Spectrum 5	28.66						70.73	0.61		100

Scorpion Creek Rock Core: depth interval 30-47 cm

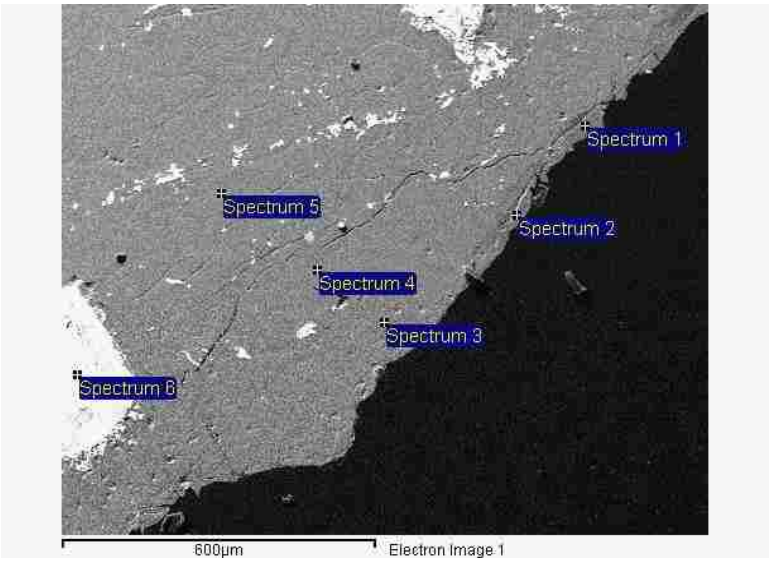

	(values in wt. %; if box is blank, it was below detection)								
Spectrum	**O**	**Mg**	**Al**	**Si**	**Ti**	**Cr**	**Fe**	**Ni**	**Total**
Spectrum 1	45.14	17.95	3.62	24.24			8.48	0.57	100
Spectrum 2	45.54	17.28	4.06	24.86			8.26		100
Spectrum 3	51.41	24.1	0.37	21.04			3.09		100
Spectrum 4	51.35	24.57		21.02			3.07		100
Spectrum 5	50.38	24.33	0.41	21.79			3.09		100
Spectrum 6	35.54	6.59	11.15		0.29	28.3	18.14		100

Scorpion Creek Rock Core: depth interval 30-47 cm

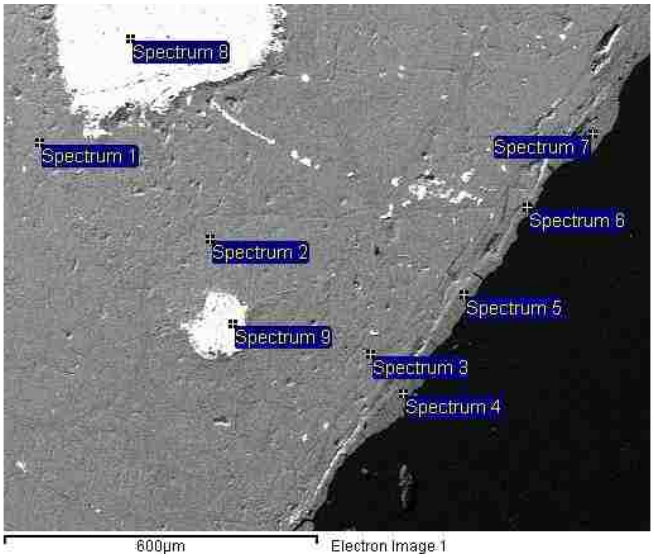

	(values in wt. %; if box is blank, it was below detection)							
Spectrum	**O**	**Mg**	**Al**	**Si**	**Cr**	**Mn**	**Fe**	**Total**
Spectrum 1	50.76	24.7		21.48			3.06	100
Spectrum 2	51.77	24.25	0.37	20.34			3.27	100
Spectrum 3	51.21	24.42	0.4	21			2.97	100
Spectrum 4	45.58	21.97	2.56	23.73			6.15	100
Spectrum 5	44.22	21.93	2.52	24.2			7.13	100
Spectrum 6	44.66	16.99	4.16	22.83			11.36	100
Spectrum 7	45.37	19.74	2.94	23.38			8.57	100
Spectrum 8	34.79	6.04	9.59		31.61		17.97	100
Spectrum 9	31.07	3.89	7.67		13.65	0.71	43	100

Scorpion Creek Rock Core: depth interval 30-47 cm

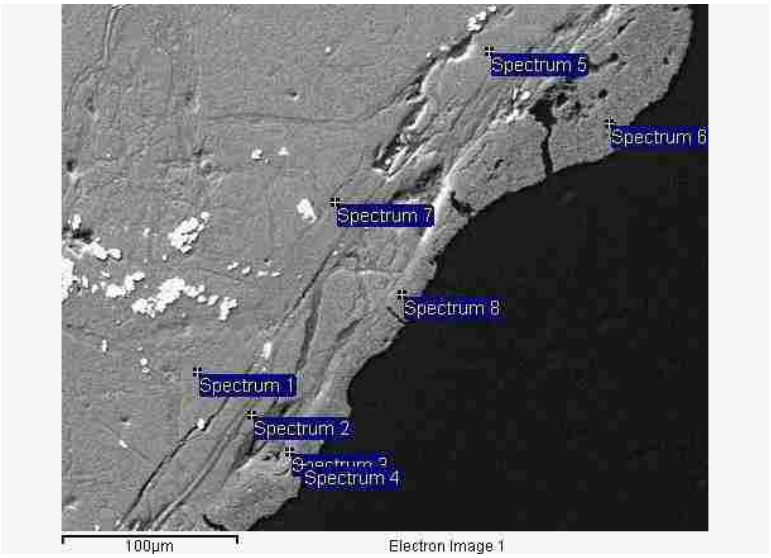

(values in wt. %; if box is blank, it was below detection)

Spectrum	O	Mg	Al	Si	Ca	Mn	Fe	Co	Ni	Total
Spectrum 1	50.94	24.41		21.12			3.53			100
Spectrum 2	50.59	24.69		21.75			2.97			100
Spectrum 3	45.27	4.79	7.87	25.09	0.59		16.4			100
Spectrum 4	48.61	21.77	1.84	21.81			5.97			100
Spectrum 5	51.66	24.56		20.89			2.88			100
Spectrum 6	47.71	20.71	2.36	22.07			7.16			100
Spectrum 7	51.45	24.1	0.72	21.4			2.33			100
Spectrum 8	41.34	11.36	5.5	16.97	0.33	8.09	10.8	3.12	2.51	100

Scorpion Creek Rock Core: depth interval 30-47 cm

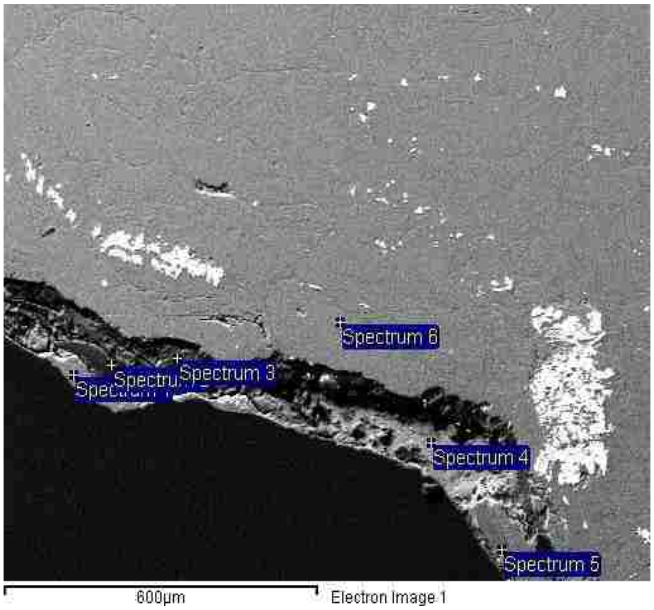

(values in wt. %; if box is blank, it was below detection)

Spectrum	O	Na	Mg	Al	Si	S	Cl	K	Ca	Ti	Fe	Mo	Total
Spectrum 1	51.22		24.26	0.36	21.14						3.01		100
Spectrum 2	51.72		2.12	2.67	22.91		1.08	0.92	4.75	1.05	9.11	3.67	100
Spectrum 3	39.5		5.09	4.2	33.54	2.15		1.24	4.38	1.66	8.23		100
Spectrum 4	47.2	8.74	2.59	0.76	35.31			0.75	4.27		0.38		100
Spectrum 5	48.16		25.45	0.53	24.16						1.7		100
Spectrum 6	50.95		24.66	0.35	21.03						3.01		100

Scorpion Creek Rock Core: depth interval 30-47 cm

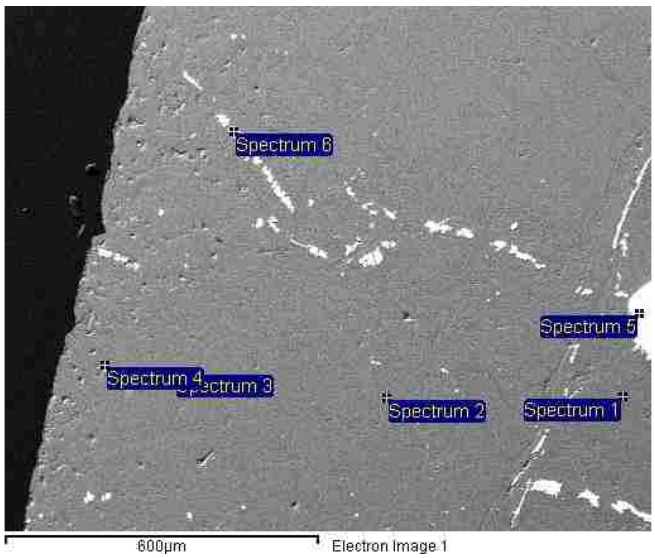

	(values in wt. %; if box is blank, it was below detection)							
Spectrum	**O**	**Mg**	**Al**	**Si**	**Cr**	**Mn**	**Fe**	**Total**
Spectrum 1	51.99	24.02	0.42	20.53			3.04	100
Spectrum 2	51.32	24.19	0.41	21.04			3.03	100
Spectrum 3	51.25	24.24	0.33	20.95			3.22	100
Spectrum 4	48.59	24.48	0.41	22.71			3.81	100
Spectrum 5	30.17	3.24		3.11	20.24	3.27	39.97	100
Spectrum 6	31.16	2.38		1.32			65.14	100

Scorpion Creek Rock Core: depth interval 70-76 cm

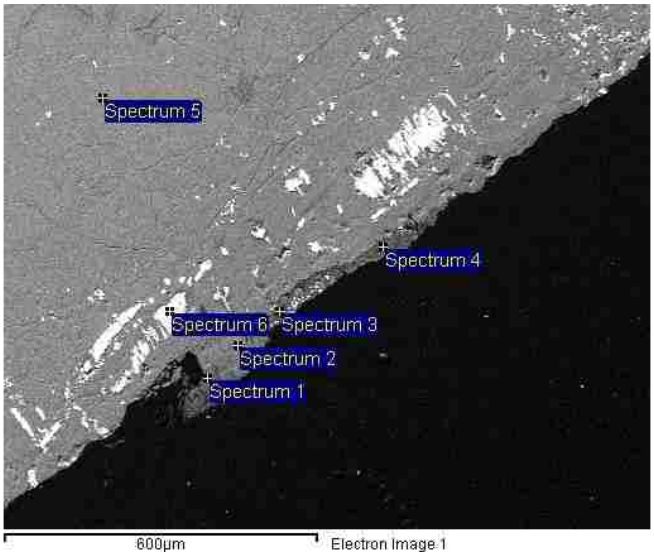

	(values in wt. %; if box is blank, it was below detection)					
Spectrum	**O**	**Mg**	**Al**	**Si**	**Fe**	**Total**
Spectrum 1	49.85	24.69	0.59	23.32	1.55	100
Spectrum 2	51.98	24.58	0.39	21.5	1.55	100
Spectrum 3	45.24	24.06	0.64	23.8	6.26	100
Spectrum 4	46.66	24.95	0.69	24.67	3.03	100
Spectrum 5	51.57	24.13	0.39	20.94	2.97	100
Spectrum 6	33.26	3.43		2.84	60.47	100

Scorpion Creek Rock Core: depth interval 70-76 cm

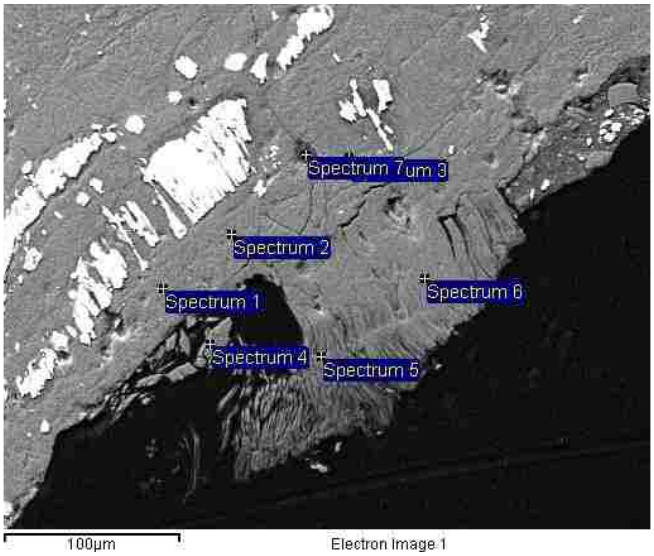

	(values in wt. %; if box is blank, it was below detection)							
Spectrum	**O**	**Mg**	**Al**	**Si**	**Ca**	**Mn**	**Fe**	**Total**
Spectrum 1	51.86	24.21	0.3	20.47			3.15	100
Spectrum 2	52.59	23.66	0.34	20.15			3.25	100
Spectrum 3	52.09	23.87	0.37	20.72			2.95	100
Spectrum 4	49.23	24.94	0.74	23.03			2.06	100
Spectrum 5	50.23	24.64	0.72	22.77			1.64	100
Spectrum 6	51.54	24.16	0.55	22.01			1.74	100
Spectrum 7	44.55	17.48	2.01	27.49	1.84	0.52	6.1	100

Scorpion Creek Rock Core: depth interval 70-76 cm

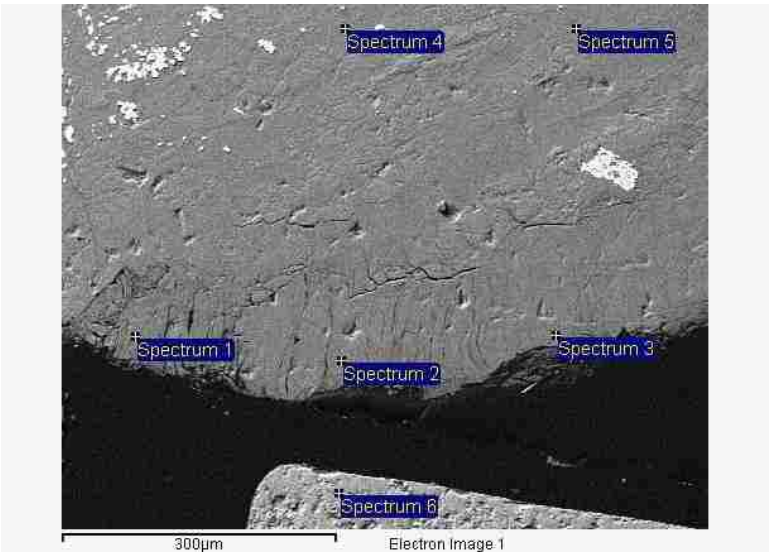

	(values in wt. %; if box is blank, it was below detection)							
Spectrum	**O**	**Na**	**Mg**	**Al**	**Si**	**K**	**Fe**	**Total**
Spectrum 1	51.09		24.58	0.51	22.23		1.6	100
Spectrum 2	51.49		24.02	0.63	21.78		2.07	100
Spectrum 3	51.92		24.35	0.68	21.71		1.35	100
Spectrum 4	51.48		24.41	0.55	21.83		1.73	100
Spectrum 5	51.5		23.65	0.59	21.4		2.86	100
Spectrum 6	45.35	0.57		9.27	31.25	13.56		100

Scorpion Creek Rock Core: depth interval 70-76 cm

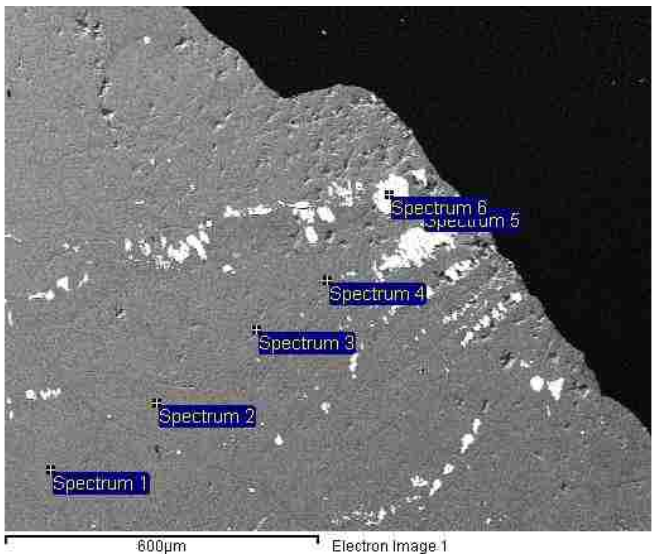

	(values in wt. %; if box is blank, it was below detection)					
Spectrum	**O**	**Mg**	**Al**	**Si**	**Fe**	**Total**
Spectrum 1	51.66	24.22	0.3	20.91	2.91	100
Spectrum 2	51.55	24.29	0.36	20.61	3.19	100
Spectrum 3	51.64	24.13	0.36	20.73	3.14	100
Spectrum 4	51.75	24.22	0.3	20.53	3.2	100
Spectrum 5	51.15	24.22	0.36	21.01	3.26	100
Spectrum 6	28.57				71.43	100

Scorpion Creek Rock Core: depth interval 70-76 cm

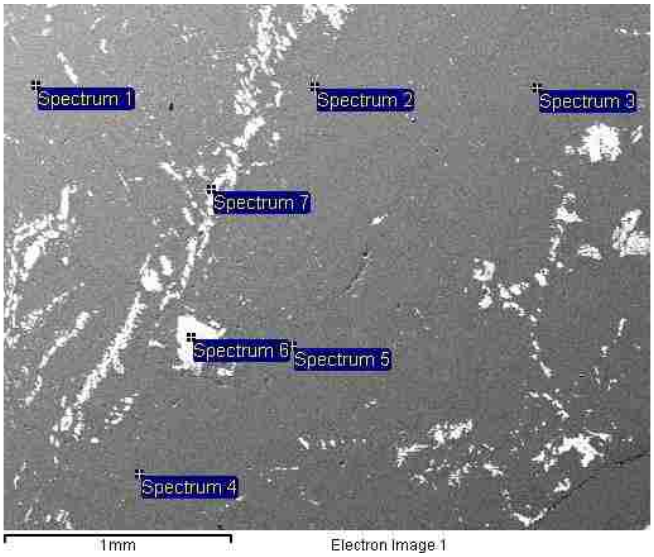

	(values in wt. %; if box is blank, it was below detection)						
Spectrum	**O**	**Mg**	**Al**	**Si**	**Cr**	**Fe**	**Total**
Spectrum 1	51.82	24.02	0.3	20.21		3.65	100
Spectrum 2	52.42	23.86	0.35	20.72		2.66	100
Spectrum 3	52.45	23.67	0.43	20.5		2.96	100
Spectrum 4	52.95	21.38	6.68	16.67		2.32	100
Spectrum 5	51.94	24.34	0.37	20.64		2.71	100
Spectrum 6	35.25	6.21	12.53		27.12	18.89	100
Spectrum 7	28.5					71.5	100

Kangaroo Lake Soil: depth interval 0-8 cm

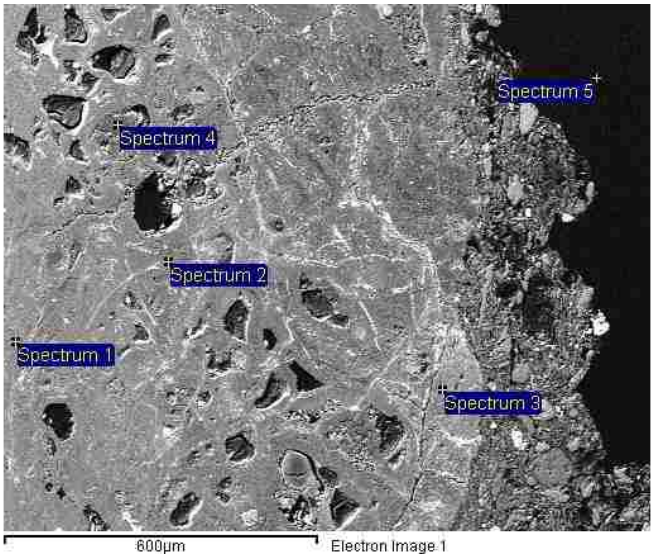

	(values in wt. %; if box is blank, it was below detection)								
Spectrum	**O**	**Mg**	**Al**	**Si**	**Cl**	**Mn**	**Fe**	**Ni**	**Total**
Spectrum 1	46.22	18.71	2.85	21.81			9.86	0.56	100
Spectrum 2	39.98	17.17	1.28	16.71			24.86		100
Spectrum 3	35.61	7.22	4.67	12.18		1.74	38.58		100
Spectrum 4	42.31	14.4	4.04	21.81	1.84		15.59		100
Spectrum 5	77.95				22.05				100

Kangaroo Lake Soil: depth interval 0-8 cm

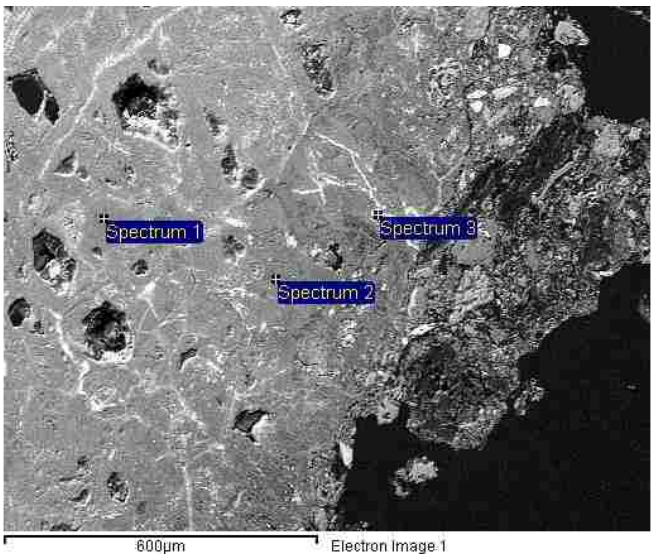

	(values in wt. %; if box is blank, it was below detection)					
Spectrum	**O**	**Mg**	**Al**	**Si**	**Fe**	**Total**
Spectrum 1	47.23	22.74	0.7	22.74	6.58	100
Spectrum 2	48.96	22.72	0.75	22.29	5.28	100
Spectrum 3	30.36		0.48	1.57	67.6	100

Kangaroo Lake Soil: depth interval 0-8 cm

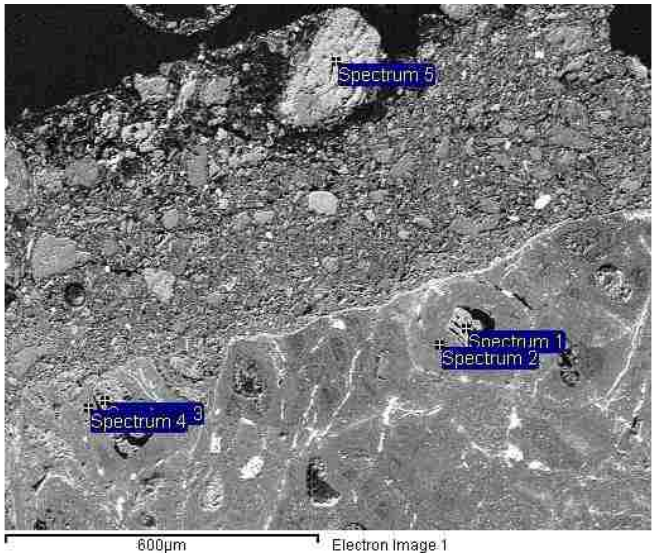

(values in wt. %; if box is blank, it was below detection)

Spectrum	O	Mg	Al	Si	Cl	K	Ca	Cr	Mn	Fe	Ni	Total
Spectrum 1	38.1	6.83	3.81	16.02	0.46		0.48	0.39		33.17	0.75	100
Spectrum 2	47.89	21.71	0.96	21.16						8.29		100
Spectrum 3	38.62	4.72	5.68	12.79			0.9	0.57	5.33	30.33	1.07	100
Spectrum 4	43.16	18.69	3.2	20.5					5.12	8.64	0.69	100
Spectrum 5	46.68	4.69	10.43	17.14		0.53				19.49	1.05	100

Kangaroo Lake Soil: depth interval 0-8 cm

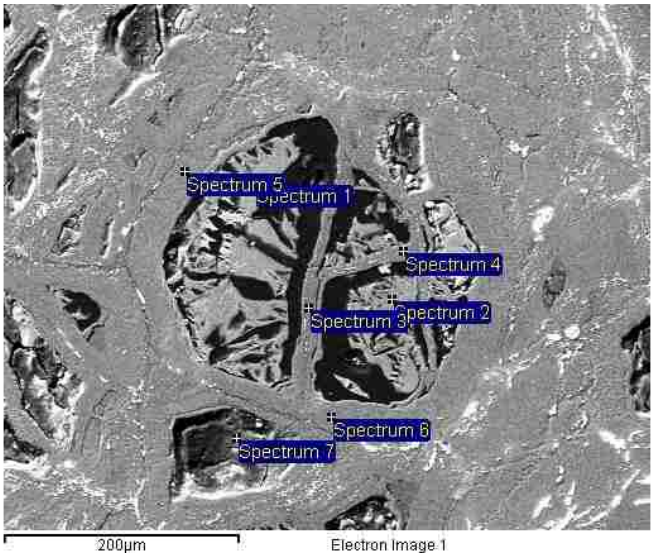

(values in wt. %; if box is blank, it was below detection)

Spectrum	O	Mg	Al	Si	S	Cl	Ca	Cr	Mn	Fe	Total
Spectrum 1	38.33	6.83	5.34	19.02		0.53	1.07	0.96		27.93	100
Spectrum 2	40.08	8.44	5.57	19.32		0.64	0.72	0.92		24.32	100
Spectrum 3	45.49	22.62	1.25	22.9		0.48			0.61	6.65	100
Spectrum 4	48.95	24.34		21.8						4.9	100
Spectrum 5	49.6	23.01	0.56	21.05						5.77	100
Spectrum 6	48.47	23.1	0.82	22.34						5.27	100
Spectrum 7	30.32	15.95	3.4	36.32	0.99	0.75	2.11			10.17	100

Kangaroo Lake Soil: depth interval 0-8 cm

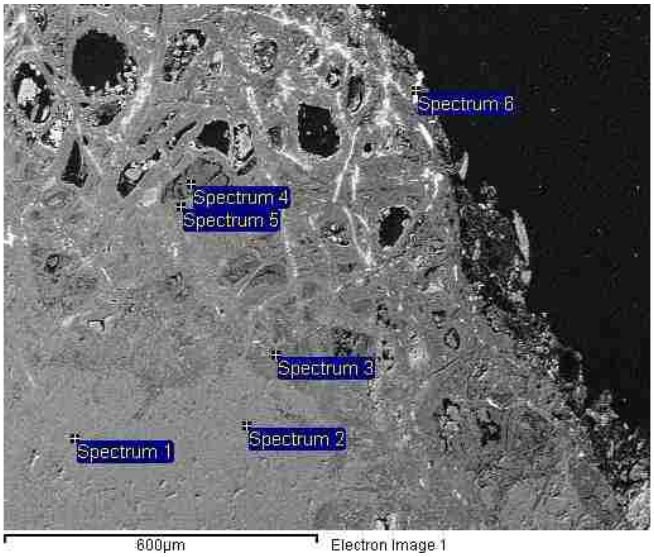

	(values in wt. %; if box is blank, it was below detection)								
Spectrum	**O**	**Mg**	**Al**	**Si**	**Cl**	**Ca**	**Cr**	**Fe**	**Total**
Spectrum 1	50.37	20.08	9.41	15.78				4.36	100
Spectrum 2	50.77	19.89	10.71	15.43				3.19	100
Spectrum 3	46.31	21.47	2.74	21.53	0.8			7.15	100
Spectrum 4	38.52	12.01	4.68	18.92	1.74	0.47		23.65	100
Spectrum 5	47.58	24.31		22.38	0.34			5.4	100
Spectrum 6	20.65	5.09	0.48	4.48			0.68	68.61	100

Kangaroo Lake Soil: depth interval 0-8 cm

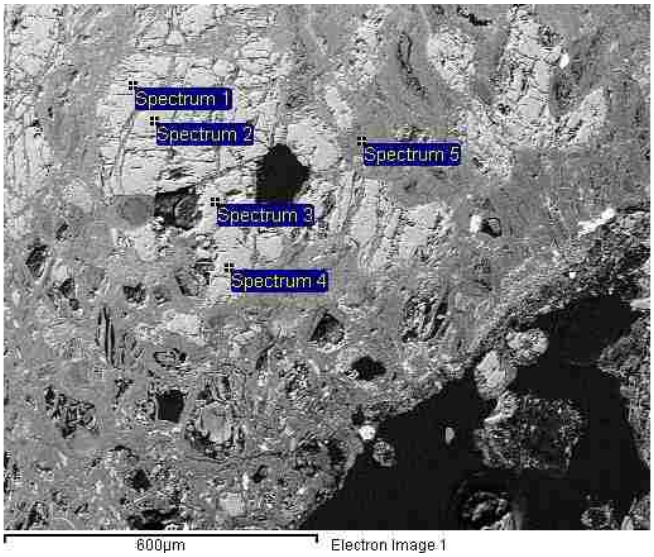

(values in wt. %; if box is blank, it was below detection)

Spectrum	O	Mg	Al	Si	Cl	Ca	Ti	Cr	Fe	Total
Spectrum 1	44.16	9.81	1.64	25.33		15.74	0.37	0.76	2.19	100
Spectrum 2	44.02	9.62	2.1	25.11		15.74	0.42	0.9	2.09	100
Spectrum 3	43.74	9.86	1.87	25.49		15.88	0.46	0.75	1.95	100
Spectrum 4	44.37	9.66	1.54	25.52		15.85	0.37	0.74	1.95	100
Spectrum 5	47.11	20.62	1.94	21.52	0.43				8.37	100

Kangaroo Lake Soil: depth interval 0-8 cm

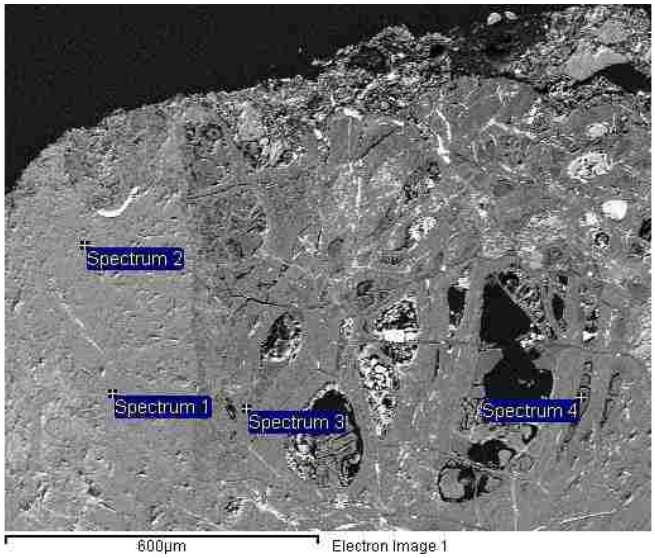

	(values in wt. %; if box is blank, it was below detection)					
Spectrum	**O**	**Mg**	**Al**	**Si**	**Fe**	**Total**
Spectrum 1	50.07	19.8	9.44	16.33	4.37	100
Spectrum 2	49.45	19.9	10.43	16.38	3.84	100
Spectrum 3	48.97	23.76	0.48	22.56	4.23	100
Spectrum 4	48.06	24.34	0.53	23.34	3.74	100

Kangaroo Lake Soil: depth interval 0-8 cm

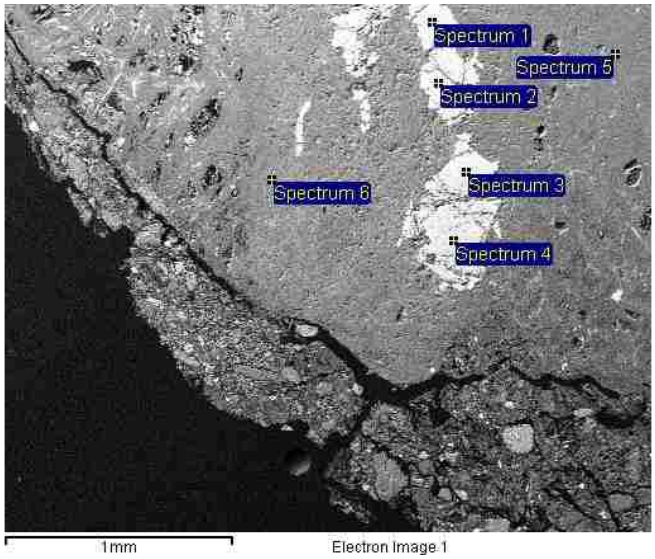

	(values in wt. %; if box is blank, it was below detection)							
Spectrum	**O**	**Mg**	**Al**	**Si**	**Ti**	**Cr**	**Fe**	**Total**
Spectrum 1	36.71	7.68	15.37		0.59	23.59	16.06	100
Spectrum 2	36.17	8.13	15.96		0.45	23.72	15.57	100
Spectrum 3	37.55	8.55	16.59		0.45	22.36	14.5	100
Spectrum 4	36.62	8.61	16.68		0.36	22.53	15.2	100
Spectrum 5	51.64	22.29	2.22	19.73			4.13	100
Spectrum 6	50.83	21.57	3.65	19.32			4.63	100

Kangaroo Lake Soil: depth interval below 41 cm

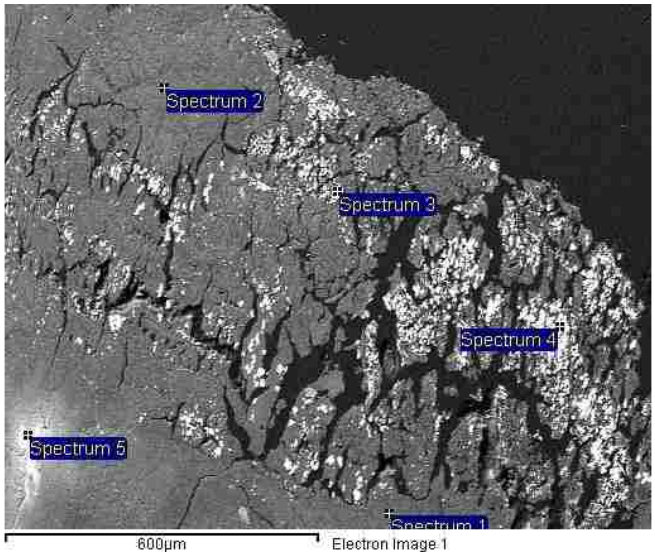

	(values in wt. %; if box is blank, it was below detection)					
Spectrum	**O**	**Mg**	**Si**	**Cl**	**Fe**	**Total**
Spectrum 1	48.08	25.76	23.28	0.28	2.61	100
Spectrum 2	49.77	25.06	22.66		2.51	100
Spectrum 3	18.64	0.78	1.65		78.93	100
Spectrum 4	30.84		0.42		68.74	100
Spectrum 5	54.17	23.01	20.72		2.09	100

Kangaroo Lake Soil: depth interval below 41 cm

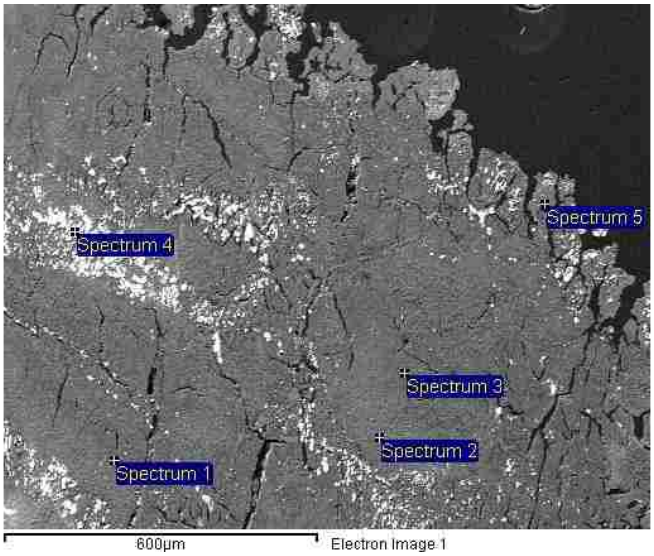

	(values in wt. %; if box is blank, it was below detection)						
Spectrum	**O**	**Mg**	**Al**	**Si**	**Cl**	**Fe**	**Total**
Spectrum 1	45.76	23.64		25.84	0.53	4.22	100
Spectrum 2	49.01	23.83	0.37	23.32		3.47	100
Spectrum 3	46.7	23.4	0.41	25.22		4.27	100
Spectrum 4	30.05			0.44		69.51	100
Spectrum 5	37.52	17.54	0.88	22.96		21.1	100

Kangaroo Lake Soil: depth interval below 41 cm

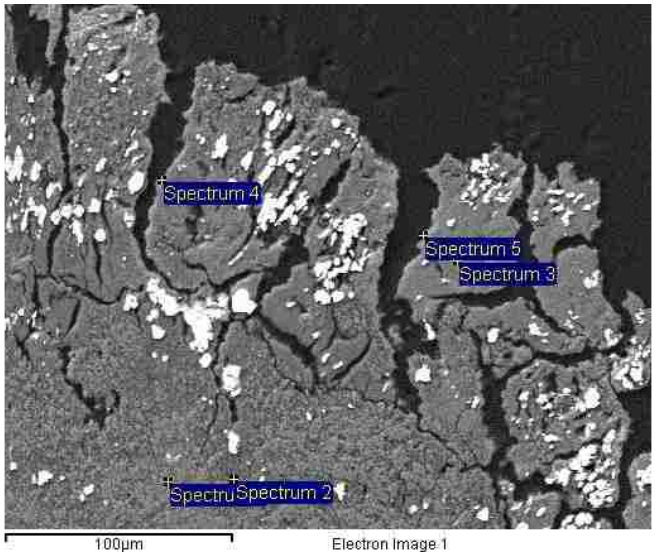

	(values in wt. %; if box is blank, it was below detection)						
Spectrum	**O**	**Mg**	**Al**	**Si**	**Cl**	**Fe**	**Total**
Spectrum 1	51.27	25.71		21.97		1.05	100
Spectrum 2	44.92	22.71	0.51	26.48		5.37	100
Spectrum 3	46.85	18.24	1.06	25.94		7.9	100
Spectrum 4	44.31	11.87	3.44	24.24		16.15	100
Spectrum 5	66.74			6.48	18.69	8.08	100

Kangaroo Lake Soil: depth interval below 41 cm

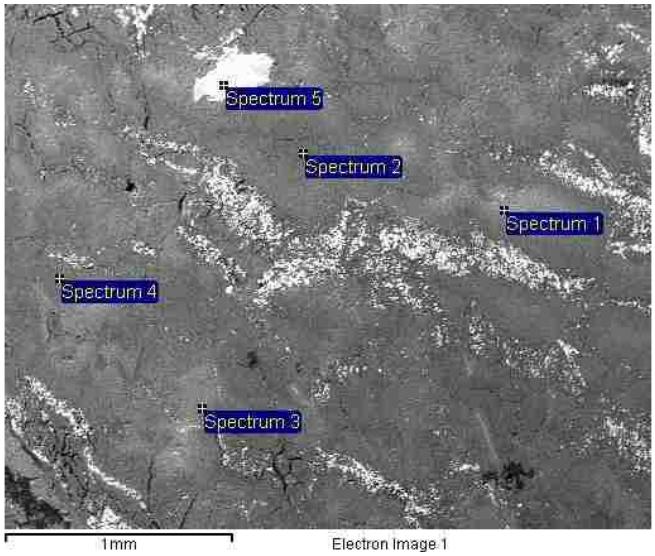

	(values in wt. %; if box is blank, it was below detection)							
Spectrum	**O**	**Mg**	**Al**	**Si**	**Cl**	**Cr**	**Fe**	**Total**
Spectrum 1	65.42	20.73		13.85				100
Spectrum 2	47.98	23.71		23.94	0.59		3.79	100
Spectrum 3	61.14	21.84		16.54			0.48	100
Spectrum 4	49.38	24.95		23.35			2.32	100
Spectrum 5	38.88	8.31	15.57	0.6		22.31	14.33	100

Kangaroo Lake Soil: depth interval below 41 cm

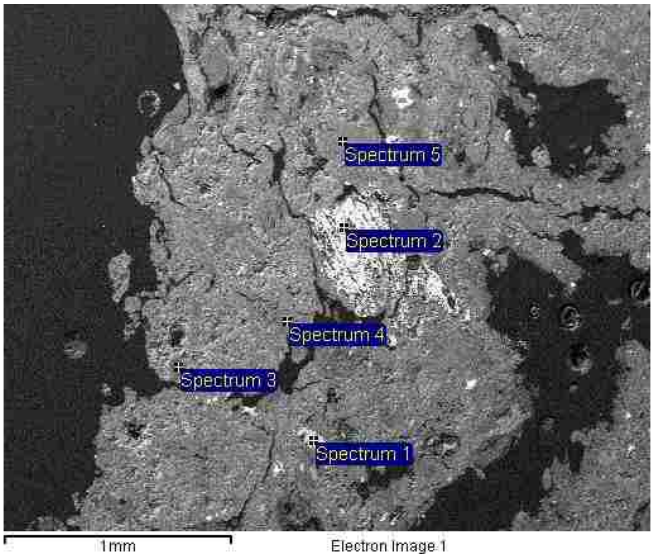

	(values in wt. %; if box is blank, it was below detection)							
Spectrum	**O**	**Mg**	**Al**	**Si**	**K**	**Ca**	**Fe**	**Total**
Spectrum 1	39.93		0.53	16.76		22.69	20.09	100
Spectrum 2	29.07						70.93	100
Spectrum 3	48.7	24.26		22.64			4.4	100
Spectrum 4	46.45	9.47	7.08	23.42	1.19	0.82	11.56	100
Spectrum 5	49.82	19.79	9.58	16.64			4.17	100

Kangaroo Lake Rock Core: depth interval 27-41 cm

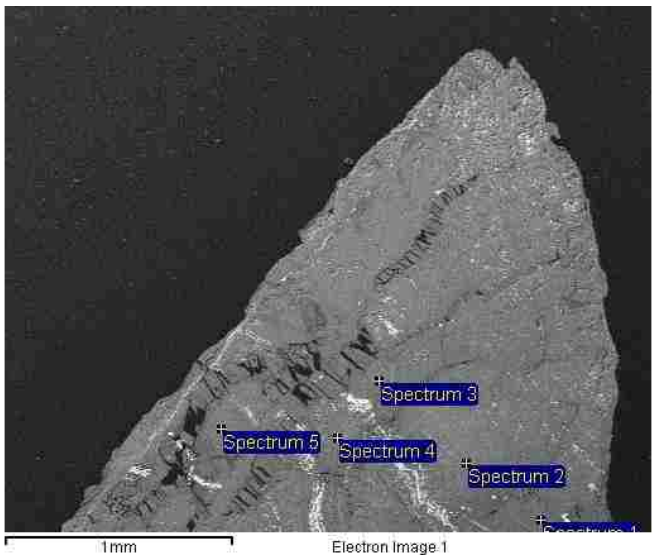

	(values in wt. %; if box is blank, it was below detection)					
Spectrum	**O**	**Mg**	**Si**	**Ca**	**Fe**	**Total**
Spectrum 1	49.74	22.1	21.97		6.19	100
Spectrum 2	60.15	21.53	16.87		1.46	100
Spectrum 3	49.84	23.07	21.01		6.08	100
Spectrum 4	49.88	22.75	21.57		5.8	100
Spectrum 5	47.88	20.77	23.22	0.25	7.88	100

Kangaroo Lake Rock Core: depth interval 27-41 cm

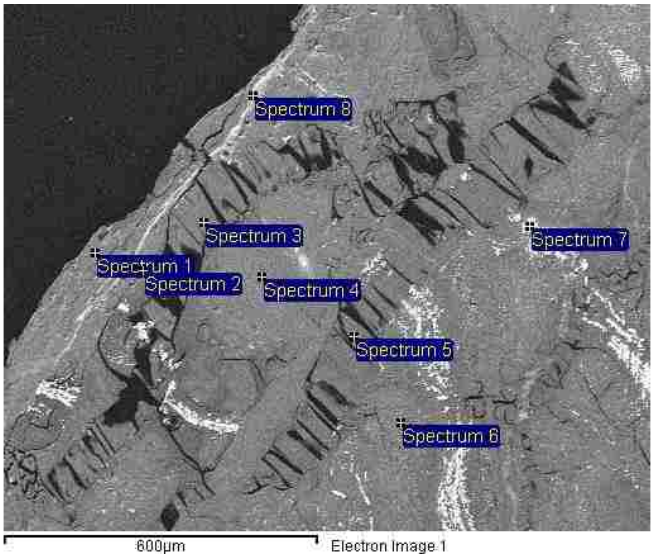

(values in wt. %; if box is blank, it was below detection)

Spectrum	O	Mg	Al	Si	Ca	Mn	Fe	Co	Ni	Total
Spectrum 1	49.62	19.06	0.77	23.91	0.26		6.38			100
Spectrum 2	50.84	22.03		20.58			6.56			100
Spectrum 3	46.31	16.14	0.59	26.48			10.48			100
Spectrum 4	50.14	22.75		21.49			5.63			100
Spectrum 5	47.45	16.89	0.55	25.79			9.31			100
Spectrum 6	53.81	22.38		19.99			3.82			100
Spectrum 7	34.46	6.18		5.78			53.58			100
Spectrum 8	39.62	9.78	0.53	15.61	0.64	11.77	18.41	1.14	2.48	100

Kangaroo Lake Rock Core: depth interval 27-41 cm

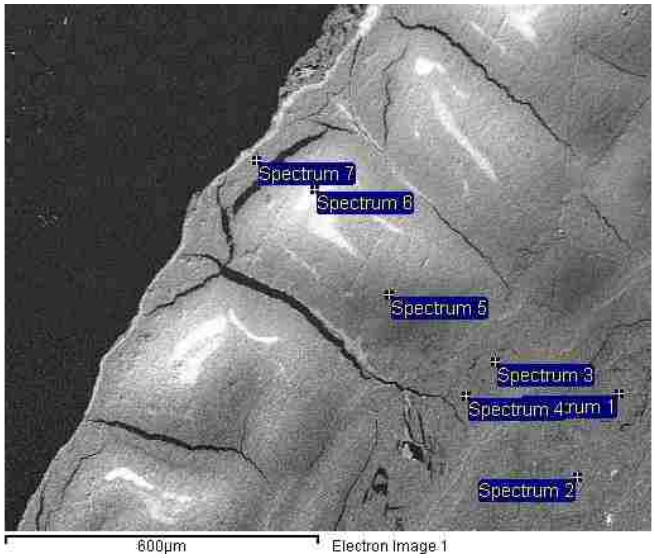

(values in wt. %; if box is blank, it was below detection)

Spectrum	O	F	Mg	Al	Si	Ca	Fe	Ni	Total
Spectrum 1	46.09		19.21	0.69	23.6	0.35	9.46	0.59	100
Spectrum 2	49.1		22.97		22.27		5.65		100
Spectrum 3	44.5		19.41	0.89	25.83		9.37		100
Spectrum 4	48.79		18.45	0.73	24.51	1.15	6.37		100
Spectrum 5	62.32	8.3	15.98		13.4				100
Spectrum 6	74.9		14.45		10.65				100
Spectrum 7	48.42		19.47	0.69	24.13		7.3		100

Kangaroo Lake Rock Core: depth interval 27-41 cm

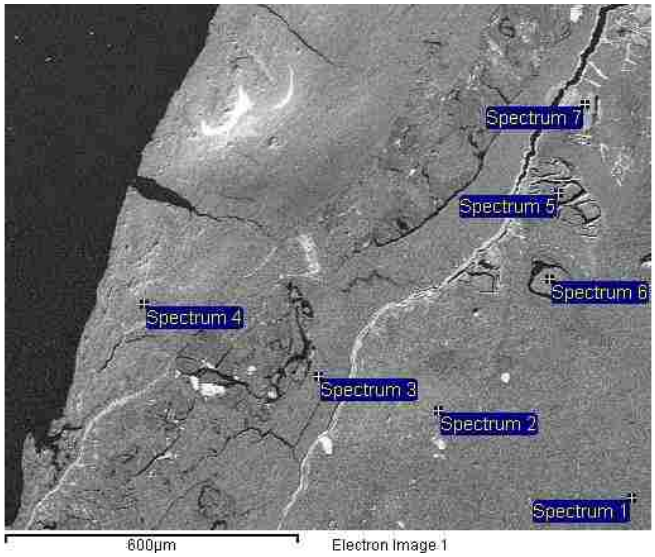

(values in wt. %; if box is blank, it was below detection)

Spectrum	O	Mg	Al	Si	Ca	Cr	Fe	Ni	Total
Spectrum 1	48.19	21.17	0.95	22.48			7.2		100
Spectrum 2	58.93	20	0.93	17.84			2.3		100
Spectrum 3	49.84	19.85	0.69	23.55			6.07		100
Spectrum 4	62.08	17.42	0.69	18.5	0.24		1.06		100
Spectrum 5	44.5	9.06	1.48	27.75	0.33		16.13	0.74	100
Spectrum 6	44.95	6.7	1.4	27.78	0.56		17.88	0.72	100
Spectrum 7	44.42	9.74	1.78	25.17	16.07	0.63	2.19		100

Kangaroo Lake Rock Core: depth interval 27-41 cm

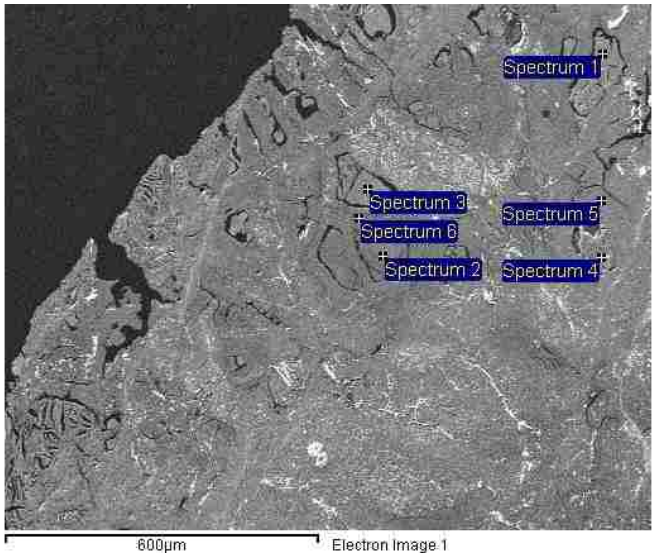

(values in wt. %; if box is blank, it was below detection)

Spectrum	O	Mg	Al	Si	Cl	Ca	Cr	Fe	Ni	Total
Spectrum 1	45.45	10.14	1.5	26.63		0.61		15.68		100
Spectrum 2	45	17.16	0.94	24.31	0.44	0.36	0.33	11.47		100
Spectrum 3	46.13	9.55	1.37	26.65		0.78		15.53		100
Spectrum 4	47.27	12.47	1.36	27.99		0.74		9.63	0.54	100
Spectrum 5	48.81	21.63	0.49	22.59				6.49		100
Spectrum 6	47.88	22.65		22.84	0.52			6.11		100

Kangaroo Lake Rock Core: depth interval 27-41 cm

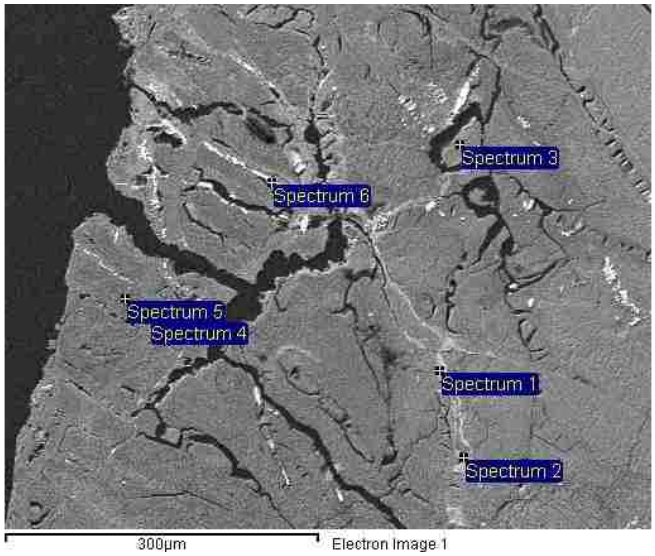

	(values in wt. %; if box is blank, it was below detection)					
Spectrum	**O**	**Mg**	**Al**	**Si**	**Fe**	**Total**
Spectrum 1	48.39	21.68	0.43	22.3	7.2	100
Spectrum 2	44.63	13.58	1.12	20.89	19.77	100
Spectrum 3	42.31	9.96	1.98	28.02	17.74	100
Spectrum 4	44.58	18.54	1.53	26.46	8.89	100
Spectrum 5	43.14	21.32	0.9	25.74	8.89	100
Spectrum 6	29.39				70.61	100

Kangaroo Lake Rock Core: depth interval 27-41 cm

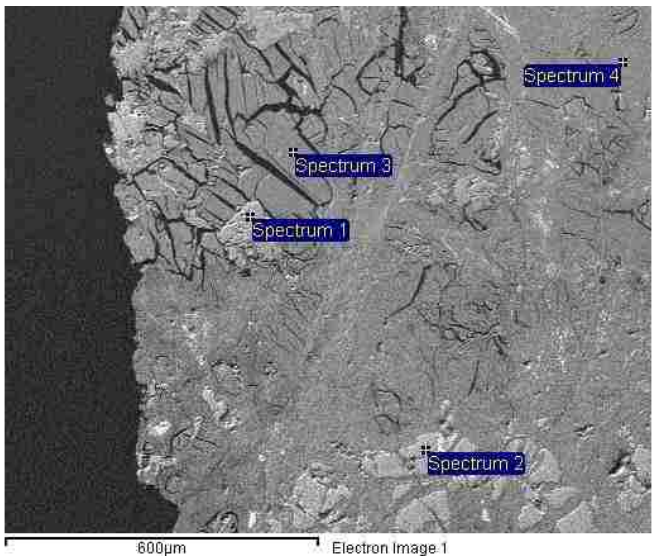

(values in wt. %; if box is blank, it was below detection)

Spectrum	O	Na	Mg	Al	Si	Ca	Ti	Cr	Fe	Total
Spectrum 1	47.07	0.53	12.77	2.15	25.36	8.83	0.32	0.73	2.25	100
Spectrum 2	44.7		9.76	1.68	25.34	16.21		0.38	1.94	100
Spectrum 3	44.75		14.66	2.21	26.69			0.74	10.94	100
Spectrum 4	50.3		22.85		21.45				5.4	100

Kangaroo Lake Rock Core: depth interval 27-41 cm

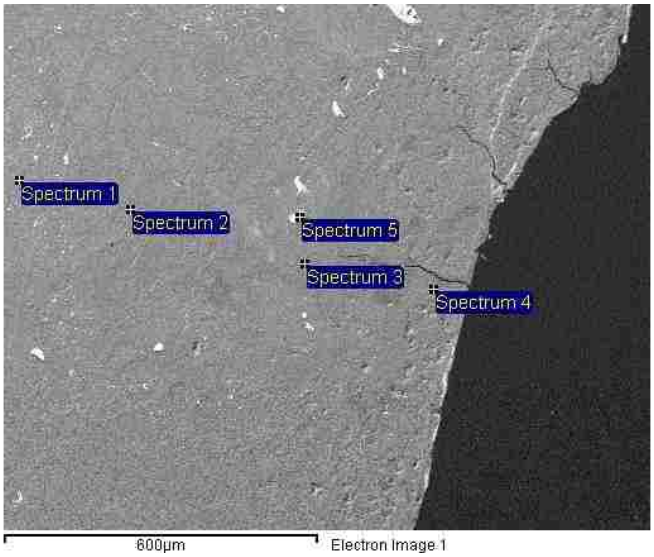

	(values in wt. %; if box is blank, it was below detection)								
Spectrum	**O**	**Mg**	**Al**	**Si**	**Ca**	**Cr**	**Fe**	**Zn**	**Total**
Spectrum 1	50.35	21.88	1.14	20.35		0.9	5.38		100
Spectrum 2	47.67	22.06	1.2	23.16			5.91		100
Spectrum 3	50.69	21.67	3.18	19.16		0.54	4.75		100
Spectrum 4	46.17	20.42	0.75	24.92	0.26		7.49		100
Spectrum 5	35.58	5.83	13.44			24.6	19.69	0.86	100

Kangaroo Lake Rock Core: depth interval 27-41 cm

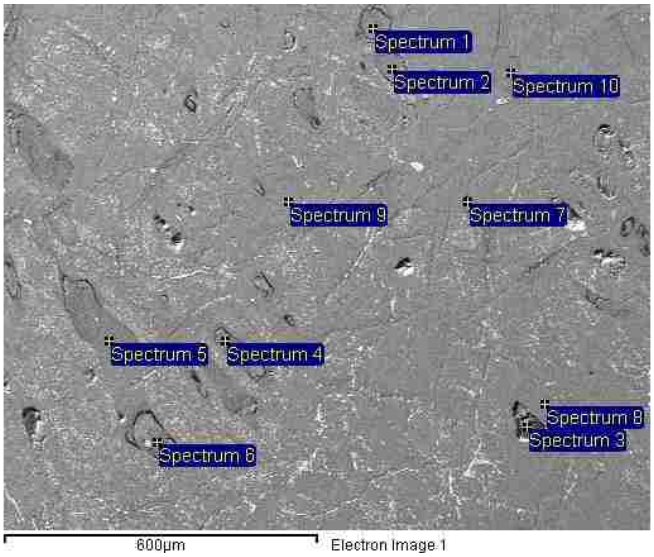

(values in wt. %; if box is blank, it was below detection)

Spectrum	O	Mg	Al	Si	S	Cl	K	Ca	Fe	Ni	Total
Spectrum 1	46.04	15.61	0.77	25.88					11.71		100
Spectrum 2	44.48	13.5	0.97	27.09					13.21	0.74	100
Spectrum 3	36.14	5.49	3.59	30.94	4.72	1.03	1.13	5.46	11.5		100
Spectrum 4	45.92	12.28	0.91	25.61		0.78		0.71	13.79		100
Spectrum 5	44.55	15.23	1.06	27.36		0.56		0.61	10.62		100
Spectrum 6	45.72	12.93	0.81	26.1		0.73		1.38	12.35		100
Spectrum 7	45.43	9.65	0.93	25.74		0.32		0.39	17.54		100
Spectrum 8	49.7	22.74		21.37					6.19		100
Spectrum 9	50.88	23.15		20.95					4.6	0.42	100
Spectrum 10	49.53	22.96	0.86	21.74					4.9		100

Kangaroo Lake Rock Core: depth interval 122-135 cm

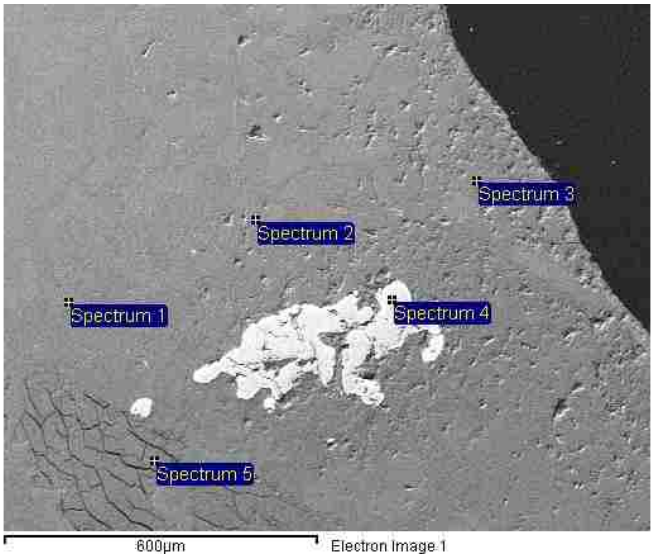

(values in wt. %; if box is blank, it was below detection)

Spectrum	O	Mg	Al	Si	Ca	Cr	Mn	Fe	Total
Spectrum 1	51.34	20.27	9.49	15.79				3.12	100
Spectrum 2	51.58	20.28	5.75	18.66				3.73	100
Spectrum 3	50.54	21.19	0.43	21.53				6.31	100
Spectrum 4	36.31	6.64	13.95			24.53	0.8	17.77	100
Spectrum 5	47.57	16.98	1.39	25.57	0.28			8.21	100

Kangaroo Lake Rock Core: depth interval 122-135 cm

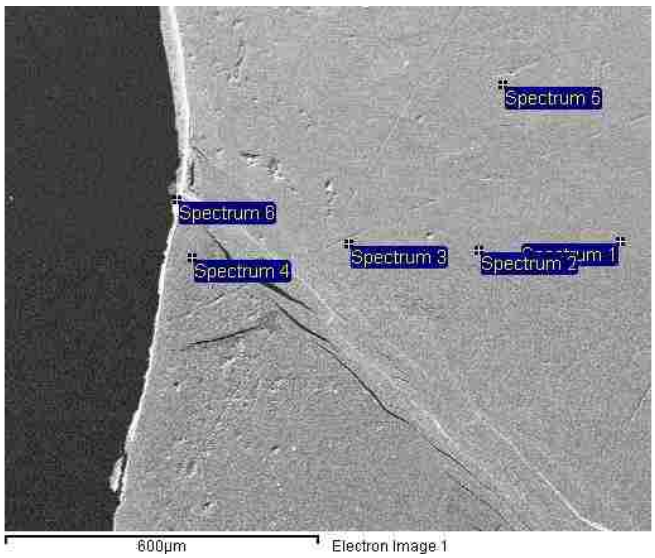

(values in wt. %; if box is blank, it was below detection)

Spectrum	O	Mg	Al	Si	Ca	Mn	Fe	Co	Ni	Total
Spectrum 1	51.63	21.77		20.86			5.75			100
Spectrum 2	51.15	22.23		21.05			5.57			100
Spectrum 3	50.58	21.87	0.36	21.19			6.01			100
Spectrum 4	50.09	22.76		22.28			4.87			100
Spectrum 5	47.2	18.6	1.04	23.17	0.22		9.76			100
Spectrum 6	42.65	3.34	1.92	0.63	0.34	33.68	2.07	7.7	7.67	100

Kangaroo Lake Rock Core: depth interval 122-135 cm

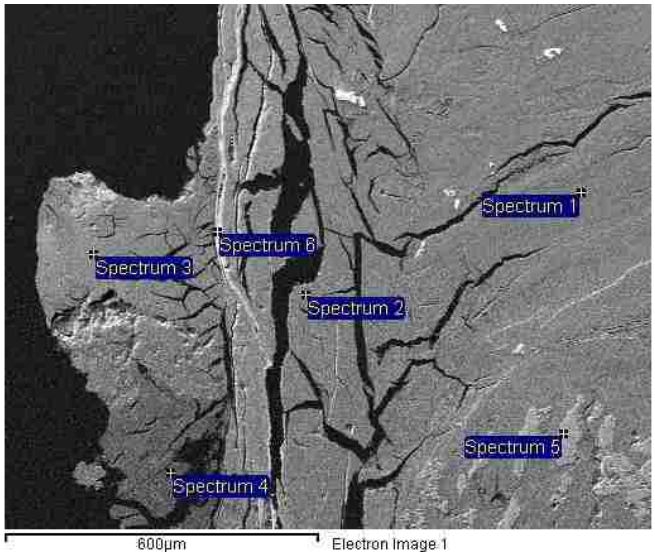

(values in wt. %; if box is blank, it was below detection)

Spectrum	O	Mg	Al	Si	Cl	Ca	Cr	Mn	Fe	Co	Ni	Total
Spectrum 1	47.43	16.62	2.04	25.08		0.27			8.57			100
Spectrum 2	46.77	14.46	2.04	25.72		0.29			10.71			100
Spectrum 3	48.48	14.23	1.04	24.55		0.29			11.41			100
Spectrum 4	44.55	22.55	0.59	26.44	0.42				5.46			100
Spectrum 5	45.12	9.55	1.61	24.85		16.07	0.74		2.06			100
Spectrum 6	34.42	2.94	1.14	2.16		0.62		39.82	5.23	5.9	7.77	100

Kangaroo Lake Rock Core: depth interval 122-135 cm

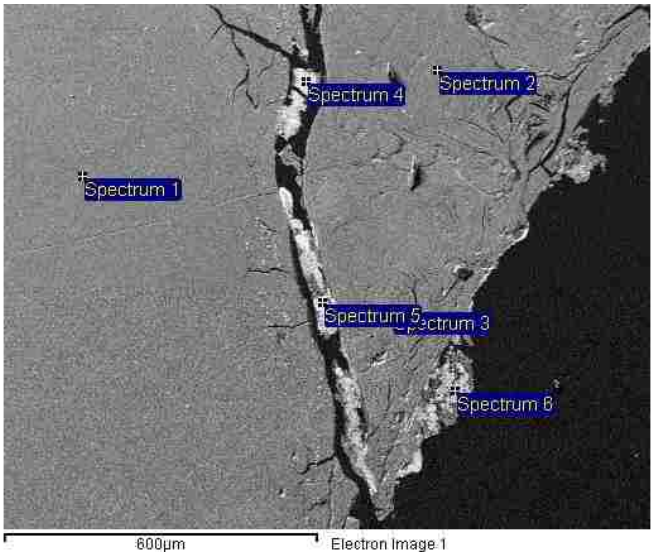

(values in wt. %; if box is blank, it was below detection)

Spectrum	O	Mg	Al	Si	Ca	Mn	Fe	Co	Ni	Total
Spectrum 1	50.08	21.9	0.64	22.4			4.97			100
Spectrum 2	51.13	23.29	0.44	21.52			3.62			100
Spectrum 3	49.02	20.07	2.32	22.68	0.27		5.65			100
Spectrum 4	41.7	5.67	1.88	6.26	0.54	24.82	6.54	6.52	6.07	100
Spectrum 5	42.28	4.81	2.33	3.83	0.46	26.07	4.58	7.23	8.4	100
Spectrum 6	38.36	6.7	1.69	10.01	0.57	23.91	5.63	6.72	6.4	100

Kangaroo Lake Rock Core: depth interval 122-135 cm

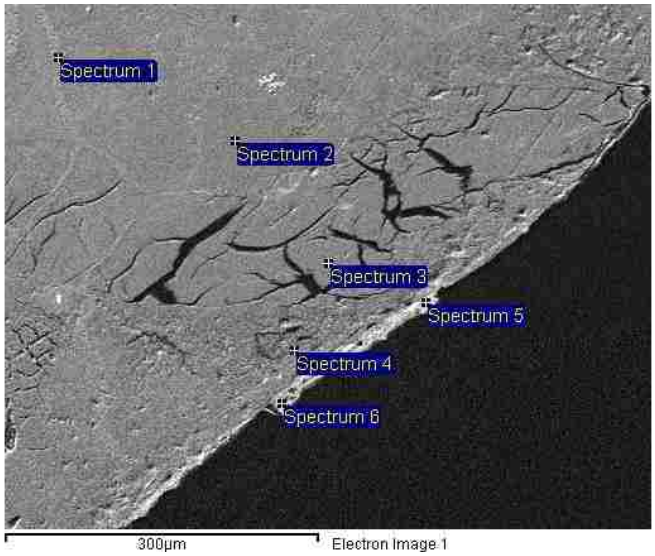

(values in wt. %; if box is blank, it was below detection)

Spectrum	O	Mg	Al	Si	Ca	Mn	Fe	Co	Ni	Total
Spectrum 1	48.8	21.36	1.73	22.56			5.55			100
Spectrum 2	52	23.94	0.34	20.86			2.86			100
Spectrum 3	46.33	15.17	1.58	26.95			9.98			100
Spectrum 4	49.01	21.58	0.98	23.13			5.3			100
Spectrum 5	39.65	5.67	2.29	7.72	0.79	24.4	6.2	7.12	6.15	100
Spectrum 6	39.21	5.41	1.86	9.27	0.74	23.25	6.85	7.23	6.18	100

Kangaroo Lake Rock Core: depth interval 122-135 cm

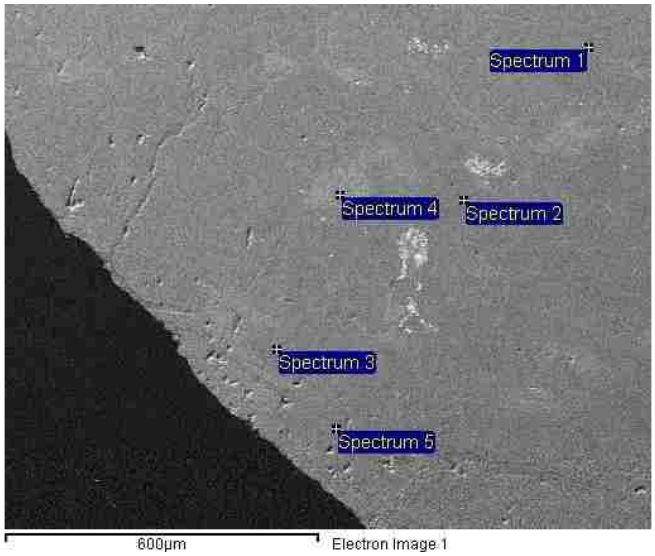

	(values in wt. %; if box is blank, it was below detection)					
Spectrum	**O**	**Mg**	**Al**	**Si**	**Fe**	**Total**
Spectrum 1	51.49	23.73		21	3.78	100
Spectrum 2	51.99	24.31		20.78	2.92	100
Spectrum 3	50.58	23.8	0.35	21.74	3.52	100
Spectrum 4	50.97	20.18	0.43	19.32	9.1	100
Spectrum 5	48.1	19.57	0.76	24.6	6.97	100

Kangaroo Lake Rock Core: depth interval 122-135 cm

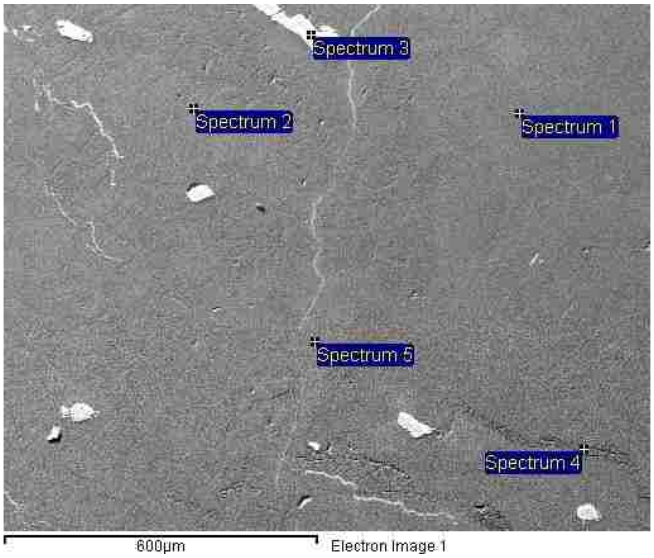

	(values in wt. %; if box is blank, it was below detection)							
Spectrum	**O**	**Mg**	**Al**	**Si**	**Cl**	**Cr**	**Fe**	**Total**
Spectrum 1	52.13	24.03		21.32			2.52	100
Spectrum 2	49.39	19.55	0.89	22.21			7.96	100
Spectrum 3	35.92	5.79	13.23			24.3	20.77	100
Spectrum 4	47.57	15.99	1.11	26.06	0.46		8.82	100
Spectrum 5	49.78	20.25	0.72	21.65			7.6	100

APPENDIX B

KLAMATH MOUNTAINS SIDEROPHORE STANDARDS DATA

This appendix contains the measurements for UV-absorbance of DFAM (commercially available siderophore, deferoxamine mesylate) standards measured at 630 nm on a Thermo Scientific Geneys 10S UV-Vis photospectrometer. Samples contained standard concentrations of DFAM and chrome azurol S, which was prepared according to the methods of Schwyn and Neilands (1987). The UV-absorbance of the standards was measured at 2-hour intervals for 6 hours (Table B.1). A standard curve for UV-absorbance versus siderophore concentration was made (Figure B.1) in order to estimate concentration of possible siderophores in soil pore waters collected from the Klamath Mountains (See Chapter 2). This assumes a siderophore similar in strength to DFAM.

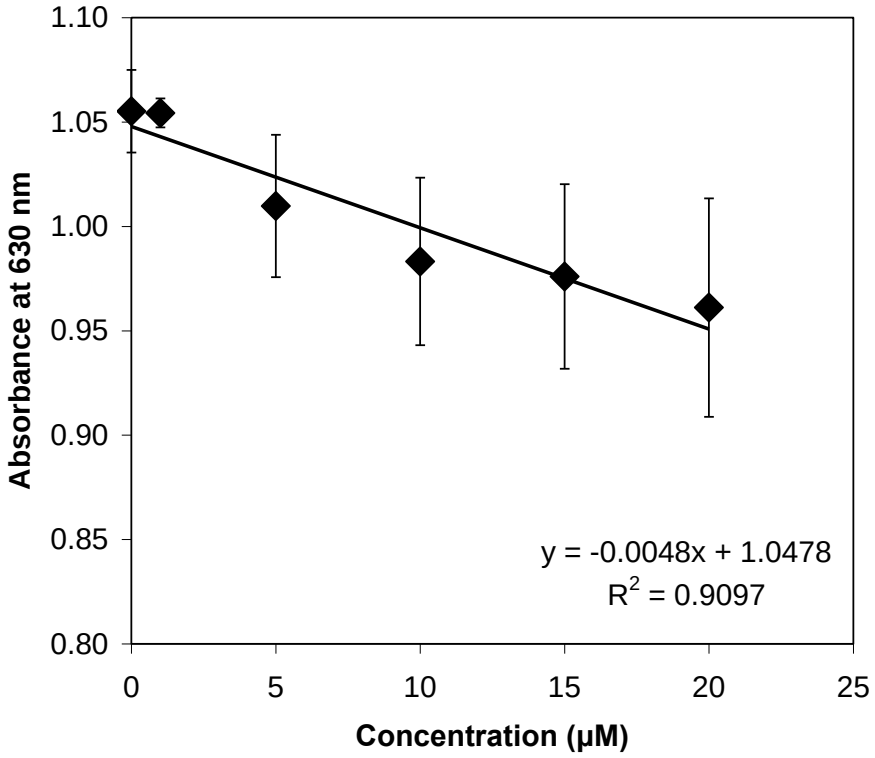

Figure B.1. Standard curve for siderophore concentration produced from the average absorbance values at 630 nm of DFAM standards measured over a 6-hour period. Error bars represent the standard deviation of all the absorbance measurements. The standard deviation increases with concentration of siderophore because higher concentrations of siderophores will complex with the iron in the chrome azurol S assay. This reaction causes CAS dye to be released, which is accompanied by a decrease in absorbance at this wavelength.

Table B.1. UV-absorbance of DFAM standards measured at 630 nm

DFAM	0 hours			2 hours		
(μM)	Run #1	Run #2	Run #3	Run #1	Run #2	Run #3
0	1.027	1.062	1.062	1.053	1.051	1.068
1	1.047	1.054	1.062	1.058	1.062	1.055
5	1.056	1.069	1.042	1.014	1.016	1.015
10	1.039	1.067	1.012	0.987	0.994	0.996
15	1.011	1.032	1.041	1.001	0.998	1.002
20	1.013	1.035	1.033	0.991	0.984	0.989

Table B.1 (*continued*). UV-absorbance of DFAM standards measured at 630 nm

DFAM	4 hours			6 hours			All	
(μM)	Run #1	Run #2	Run #3	Run #1	Run #2	Run #3	Average	St. Dev.
0	1.054	1.057	1.008	1.075	1.070	1.075	1.055	0.020
1	1.046	1.040	1.052	1.056	1.060	1.060	1.054	0.007
5	1.000	1.001	0.996	0.976	0.947	0.985	1.010	0.034
10	0.953	0.952	0.951	0.948	0.950	0.949	0.983	0.040
15	0.954	0.960	0.959	0.918	0.914	0.922	0.976	0.044
20	0.936	0.920	0.935	0.900	0.899	0.898	0.961	0.052

APPENDIX C

KLAMATH MOUNTAINS ORGANIC CONSTITUENT DATA

Although the method used in Chapter 2 (American Public Health Association, 1998; Strauss and Lamberti, 2002; Weishaar et al., 2003) for organic constituents is not meant to obtain concentrations of specific organic acids, standards were also prepared for general comparison of the following organic acids: oxalate (10, 30, 50 mM), formate (10, 30, 50, 70 mM), propionate (10, 30, 50 mM), salicylate (10, 30, 50 mM), succinate (1, 5, 10 mM), citrate (1, 5, 10 mM), and acetate (1, 5, 10 mM).

Ultraviolet absorbance of standards for oxalate, formate, propionate, salicylate, succinate, citrate, and acetate were also measured at 253.7 nm on a Thermo Scientific Genesys 10S UV-Vis spectrophotometer (Figure C.1). Blanks consisted of DI water. The relationship between absorbance and concentration was linear for acetate (R^2=0.8772; Figure C.1a), succinate (R^2=0.9999; Figure C.1a), and oxalate (R^2=0.9998; Figure C.1b). The remaining organic acid standards showed poor linear correlations with $R^2 < 0.56$ (Figure C.1).

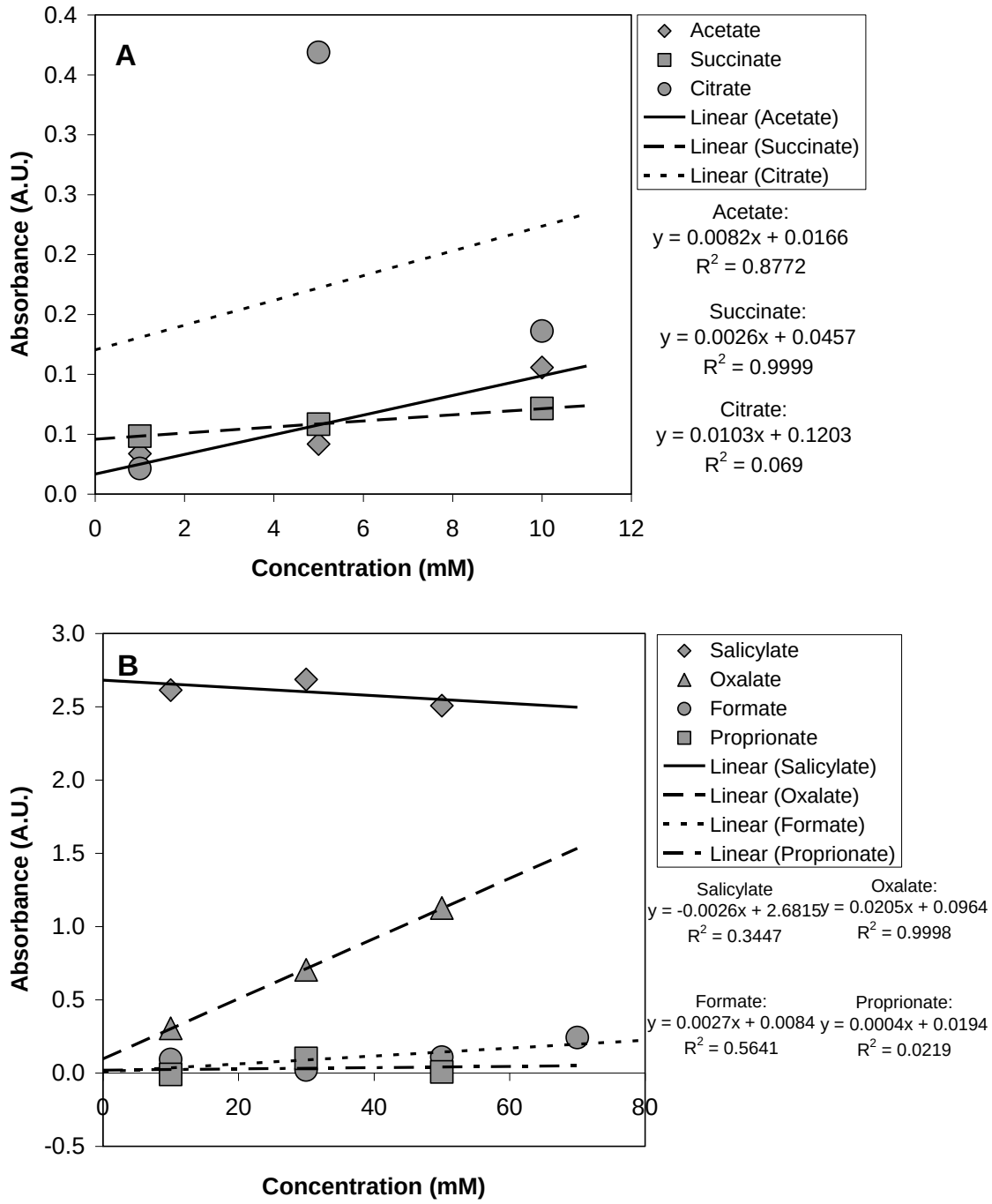

Figure C.1. Ultraviolet absorbance of organic acids standards measured at 253.7 nm. A) Ultraviolet absorbance of acetate, succinate, and citrate standards showing linear fits. B) Ultraviolet absorbance of salicylate, oxalate, formate, and propionate showing linear fits.

REFERENCES

Alexander, E.B., 2004, Serpentine soil redness, differences among peridotite and serpentinite materials, Klamath Mountains, California: International Geology Review, v. 46, p. 754-764.

Alexander, E.B., Coleman, R.G., Keeler-Wolf, T., and Harrison, S.P., 2007, Serpentine geoecology of western North America: New York, Oxford University Press, 512 p.

Alexander, E.B., and DuShey, J., 2011, Topographic and soil differences from peridotite to serpentinite: Geomorphology, v. 135, p. 271-276.

American Public Health Association, 1998, UV-Absorbing organic constituents: Ultraviolet absorpion method, *in* Clesceri, L.S., Greenberg, A.E., and Eaton, A.D., eds., Standard Methods for the Examination of Water and Wastewater, 20th Edition, Washington, DC.

April, R., Newton, R., and Coles, L.T., 1986, Chemical weathering in two Adirondack watersheds: Past and present day rates: Geological Society of Americal Bulletin, v. 97, p. 1232-1238.

Bales, R.C., and Morgan, J.J., 1985, Dissolution kinetics of chrysotile at pH 7 to 10: Geochimica et Cosmochimica Acta, v. 49, p. 2281-2288.

Bandstra, J.Z., and Brantley, S.L., 2008, Data fitting techniques with applications to mineral dissolution kinetics, *in* Brantley, S. L., Kubicki, J.D., and White, A.F., eds., Kinetics of water-rock interaction: New York, Springer, p. 211–258.

Béarat, H., McKelvy, M.J., Chizmeshya, A.V.G., Gormley, D., Nunez, R., Carpenter, R.W., Squires, K., and Wolf, G.H., 2006, Carbon sequestration via aqueous olivine mineral carbonation: Role of passivating layer formation: Environmental Science and Technology, v. 40, p. 4802-4808.

Bergman, S.C., Foland, K.A., and Spera, F.J., 1981, On the origin of an amphibole-rich vein in a peridotite inclusion from Lunar Crater Volcanic Field, Nevada, U.S.A.: Earth and Planetary Science Letters, v. 56, p. 343-361.

Blum, A.E., and Lasaga, A.C., 1988, Role of surface speciation in the low-temperature dissolution of minerals: Nature, v. 331, p. 431-433.

Brady, P.V., and Walther, J.V., 1989, Controls on silicate dissolution rates in neutral and basic pH solutions at 25°C: Geochimica et Cosmochimica Acta, v. 53, p. 2823-2830.

Brady, N.C., and Weil, R.R., 2002, The nature and properties of soils: Prentice Hall, Upper Saddle River, NJ, 960 p.

Brady, K.U., Kruckeberg, A.R., and Bradshaw, H.D.Jr., 2005, Evolutionary ecology of plant adaptation to serpentine soils: Annual Review of Ecology Evolution and Systematics, v. 36, p. 243-266.

Brantley, S., 2003, Reaction kinetics of primary rock-forming minerals under ambient conditions., *in*: Drever, J., ed., Treatise on geochemistry, surface and groundwater, weathering and soils, vol. 5: Elsevier, Amsterdam, p. 73–118.

Brantley, S.L., and White, A.F., 2009, Approaches to modeling weathered regolith: Reviews in Mineralogy and Geochemistry, v. 70, p. 435-484.

Buss, H.L., Bruns, M.A., Schultz, M.J., Moore, J., Mathur, C.F., and Brantley, S.L., 2005, The coupling of biological iron cycling and mineral weathering during saprolites formation, Luquillo Mountains, Puerto Rico: Geobiology, v. 3, p. 247-260.

Buss, H.L., Lüttge, A., and Brantley, S.L., 2007, Etch pit formation on iron silicate surfaces during siderophore-promoted dissolution: Chemical Geology, v. 240, p. 326-342.

Caillaud, J., Proust, D., Righi, D., and Martin, F., 2004, Fe-rich clays in a weathering profile developed from serpentinite: Clays and Clay Minerals, v. 52, p. 779-791.

Caillaud, J., Proust, D., and Righi, D., 2006, Weathering sequences of rock-forming minerals in a serpentinite: Influence of microsystems on clay mineralogy: Clays and Clay Minerals, v. 54, p. 87-100.

Caillaud, J., Proust, D., Phillipe, S., Fontaine, C., and Fialin, M., 2009, Trace metals distribution from a serpentinite weathering at the scales of the weathering profile and its related weathering microsystems and clay minerals: Geoderma, v. 149, p. 199-208.

Carey, J.W., Lichtner, P.C., Rosen, E.P., Ziock, H.J., Guthrie, G.D.Jr., 2003, Geochemical mechanisms of serpentine and olivine carbonation: 2nd Annual Conference on Carbon Sequestration.

Casey, W.H., and Westrich, H.R., 1992, Control of dissolution rates of orthosilicate minerals by divalent metal-oxygen bonds: Nature, v. 355, p. 157-159.

Chen, Y., and Brantley, S.L., 1998, Diopside and anthophyllite dissolution at 25° and 90°C and acid pH: Chemical Geology, v. 147, p. 233-248.

Cleaves, E.T., Fisher, D.W., and Bricker, O.P., 1974, Chemical weathering of serpentinite in the eastern Piedmont of Maryland: Geological Society of America Bulletin, v. 85, p. 437-444.

Daghino, S., Turci, F., Tomatis, M., Favier, A., Perotto, S., Douki, T., and Fubini, B., 2006, Soil fungi reduce the iron content and the DNA damaging effects of asbestos fibers: Environmental Science and Technology, v. 40, p. 5793-5798.

Daghino, S., Martino, E., Vurro, E., Tomatis, M., Girlanda, M., Fubini, B., and Perotto, S., 2008, Bioweathering of chrysotile by fungi isolated in ophiolitic sites: FEMS Microbiology Letters, v. 285, p. 242-249.

Daghino, S., Turci, F., Tomatis, M., Girlanda, M., Fubini, B., and Perotto, S., 2009, Weathering of chrysotile asbestos by the serpentine rock-inhabiting fungus *Verticillium leptobactrum*: FEMS Microbiology Ecology, v. 69, p. 132-141.

Daniels, M.L., Anderson, S., Whitlock, C., 2005, Vegetation and fire history since the Late Pleistocene from the Trinity Mountains, northwestern California, USA: The Holocene, v. 15, p. 1062-1071.

Dessert, C., Dupré, B., Gaillardet, J., François, L.M., and Allègre, C.J., 2003, Basalt weathering laws and the impact of basalt weathering on the global carbon cycle: Chemical Geology, v. 202, p. 257-273.

Dickson, L.D., 1997, Volcanology and geochemistry of Pliocene and Quaternary basalts on Citadel Mountain, Lunar Crater Volcanic Field, Pancake Range, Nevada [M.S. thesis]: University of Nevada, Las Vegas, 146 p.

Dohrenwend, J.C., Abrahams, A.D., and Turrin, B.D., 1987, Drainage development on basaltic lava flows, Cima volcanic field, southeast California, and Lunar Crater volcanic field, south-central Nevada: Geological Society of America Bulletin, v. 99, p. 405-413.

Drever, J.I., and Stillings, L.L., 1997, The role of organic acids in mineral weathering: Colloids and Surfaces, A: Physiochemical and Engineering Aspects, v. 120, p. 167-181.

Droycon Bioconcepts Inc., 2004, Biological Activity Reaction Test BART™ User Manual: Droycon Bioconcepts Inc., Saskatchewan, Canada.

Eggleston, C.M., Hochella, M.F. Jr., and Parks, G.A., 1989, Sample preparation and aging effects on the dissolution rate and surface composition of diopside: Geochimica et Cosmochimica Acta, v. 53, p. 797-804.

Fletcher, R.C., Buss, H.L., and Brantley, S.L., 2006, A spheroidal weathering model coupling porewater chemistry to soil thickness during steady-state denudation: Earth and Planetary Science Letters, v. 244, p. 444-457.

Freyssinet, P., and Farah, A.S., 2000, Geochemical mass balance and weathering rates of ultramafic schists in Amazonia: Chemical Geology, v. 170, p. 133-151.

Goff, F., and Lackner, K.S., 1998, Carbon dioxide sequestering using ultramafic rocks: Environmental Geosciences, v. 5, p. 89-101.

Goldich, S. S., 1938, A study of rock weathering: The Journal of Geology, v. 46, p. 17-58.

Golubev, S.V., Pokrovsky, O.S., Schott, J., 2005, Experimental determination of the effect of dissolved CO_2 on the dissolution kinetics of Mg and Ca silicates at 25C: Chemical Geology, v. 217, p. 227-238

Gordon, S.J., and Brady, P.V., 2002, In situ determination of long-term basaltic glass dissolution in the unsaturated zone: Chemical Geology, v. 190, p. 113-122.

Grandstaff, D.E., 1980, The dissolution of forsteritic olivine from Hawaiian beach sand: Third International Symposium on Water-Rock Interaction, WRI-3, p. 72-74.

Grandstaff, D.E., 1986, The dissolution rate of forsteritic olivine from Hawaiian beach sand, *in* Colman, S.M., and Dethier, D.P., eds., Rates of chemical weathering of rocks and minerals: Academic Press, Inc., p. 41-59.

Gudbrandsson, S., Wolff-Boenisch, D., Gislason, S.R., and Oelkers, E.H., 2011, An experimental study of crystalline basalt dissolution from $2 \leq pH \leq 11$ and temperatures from 5 to 75 °C: Geochimica et Cosmochimica Acta, v. 75, p. 5496-5509.

Guthrie, G.D.Jr., Carey, J.W., Bergfeld, D., Byler, D., Chipera, S., Ziock, H.-J., and Lackner, K., 2001, Geochemical aspects of the carbonation of magnesium silicates in an aqueous medium: 1st National Conference on Carbon Sequestration. National Energy Technology Laboratory, Washington D.C.

Harris, T.B., Olday, F.C., and Rajakaruna, N., 2007, Lichens of Pine Hill, a peridotite outcrop in eastern North America: Rhodora, v. 109, p. 430-447.

Haselwandter, K., 1995, Mycorrhizal fungi: Siderophore production: Critical Reviews in Biotechnology, v. 15, p. 287-291.

Hausrath, E.M., Liermann, L.J., House, C.J., Ferry, J.G., and Brantley, S.L., 2007, The effect of methanogen growth on mineral substrates: will Ni markers of

methanogen-based communities be detectable in the rock record?: Geobiology, v. 5, p. 49-61.

Hausrath, E.M., Navarre-Sitcher, A.K., Sak, P.B., Steefel, C.I., and Brantley, S.L., 2008, Basalt weathering rates on Earth during the duration of liquid water on the plains of Gusev Crater, Mars: Geology, v. 36, p. 67-70.

Hausrath, E.M., Treiman, A.H., Vicenzi, E., Bish, D.L., Blake, D., Sarrazin, P., Hoehler, T., Midtkandal, I., Steele, A., and Brantley, S.L., 2008, Short- and long-term olivine weathering in Svalbard: Implications for Mars: Astrobiology, v. 8, p. 1079-1092.

Hausrath, E.M., Neaman, A., and Brantley, S.L., 2009, Elemental release rates from dissolving basalt and granite with and without organic ligands: American Journal of Science, v. 309, p. 633-660.

Hausrath, E.M., Navarre-Sitchler, A.K., Sak, P.B., Williams, J.Z., and Brantley, S.L., 2011, Soil profiles as indicators of mineral weathering rates and organic interactions for a Pennsylvania diabase: Chemical Geology, v. 290, p. 89-100.

Hersman, L., Lloyd, T., and Sposito, G., 1995, Siderophore-promoted dissolution of hematite: Geochimica et Cosmochimica Acta, v. 59, p. 3327-3330.

Hoch, A.R., Reddy, M.M., and Drever, J.I., 1996, The effect of iron content and dissolved O_2 on dissolution rates of clinopyroxene at pH 5.8 and 25C: preliminary results: Chemical Geology, v. 132, 151-156.

Hume, L.A., and Rimstidt, J.D., 1992, The biodurability of chrysotile asbestos: American Mineralogist, v. 77, p. 1125-1128.

Irwin, W.P., 1966, Geology of the Klamath Mountains province, *in*: Bailey, E.H., ed., Geology of northern California: California Division of Mines and Geology Bulletin 190, p. 19-38.

Jenny, H., 1980, The soil resource, origin and behaviour: Springer-Verlag, Berlin, 377 p.

Jin, L., Ravella, R., Ketchum, B., Bierman, P.R., Heaney, P., White, T., and Brantley, S.L., 2010, Mineral weathering and elemental transport during hillslope evolution at the Susquehanna/Shale Hills Critical Zone Observatory: Geochimica et Cosmochimica Acta, v. 74, p. 3669-3691.

Kalinowski, B.E., Liermann, L.J., Brantley, S.L., Barnes, A., and Pantano, C.G., 2000, X-ray photoelectron evidence for bacteria-enhanced dissolution of hornblende: Geochimica et Cosmochimica Acta, v. 64, p. 1331-1343.

Keleman, P.B., and Matter, J., 2008, In situ carbonation of peridotite for CO_2 storage: Proceedings of the National Academy of Sciences, v. 105, p. 17295-17300.

Knauss, K.G., Nguyen, S.N., and Weed, H.C., 1993, Diopside dissolution kinetics as a function of pH, CO_2, temperature, and time: Geochimica et Cosmochimica Acta, v. 57, p. 285-294.

Kruckeberg, A.R., 2004, Geology and plant life: The effects of landforms and rock types on plants: University of Washington Press.

Lee, B.D., Graham, R.C., Laurent, T.E., Amrhein, C., and Creasy, R.M., 2001, Spatial distributions of soil chemical conditions in a serpentinitic wetland and surrounding landscape: Soil Science Society of America Journal, v. 65, p. 1183-1196.

Lee, B.D., Sears, S.K., Graham, R.C., Amrhein, C., and Vali, H., 2003, Secondary mineral genesis from chlorite and serpentine in an ultramafic soil toposequence: Soil Science Society of America Journal, v. 67, p. 1309-1317.

Liermann, L.J., Kalinowski, B.E., Brantley, S.L., and Ferry, J.G., 2000, Role of bacterial siderophores in dissolution of hornblende: Geochimica et Cosmochimica Acta, v. 64, p. 587-602.

Lin, F.-C., and Clemency, C.V., 1981, The dissolution kinetics of brucite, antigorite, talc, and phlogopite at room temperature and pressure: American Mineralogist, v. 66, p. 801-806.

Luce, R.W., Bartlett, R.W., and Parks, G.A., 1972, Dissolution kinetics of magnesium silicates: Geochimica et Cosmochimica Acta, v. 86, p. 35-50.

Navarre-Sitchler, A., and Brantley, S., 2007, Basalt weathering across scales: Earth and Planetary Science Letters, v. 261, p. 321-334.

Neilands, J.B., 1993, Perspectives in biochemistry and biophysics: siderophores: Archives of Biochemistry and Biophysics, v. 302, p. 1-3.

Neilands, J.B., 1995, Siderophores: structure and function of microbial iron transport compounds: The Journal of Biological Chemistry, v. 270, p. 26723-26726.

Nowicki, M.A., and Velbel, M.A., 2011, Preliminary quantification of a shape model for etch-pits formed during natural weathering of olivine: Applied Geochemistry, v. 26, p. S112-114.

Oelkers, E.H., 2001, An experimental study of forsterite dissolution rates as a function of temperature and aqueous Mg and Si concentrations: Chemical Geology, v. 175, p. 485-494.

Oelkers, E.H., Gislason, S.R., and Matter, J., 2008, Mineral carbonation of CO_2: Elements, v. 4, p. 333-337.

O'Hanley, D.S., and Dyar, M.D., 1993, The composition of lizardite 1T and the formation of magnetite in serpentinites: American Mineralogist, v. 78, p. 391-404.

Olsen, A.A., and Rimstidt, J.D., 2008, Oxalate-promoted forsterite dissolution at low pH: Geochimica et Cosmochimica Acta, v. 72, p. 1758-1766.

Orlando, A., Borrini, D., and Marini, L., 2011, Dissolution and carbonation of a serpentinite: Inferences from acid attack and high P-T experiments performed in aqueous solutions at variable salinity: Applied Geochemistry, v. 26, p. 1569-1583.

Park, A.-H. A., and Fan, L.-S., 2004, CO_2 mineral sequestration: physically activated dissolution of serpentine and pH swing process: Chemical Engineering Science, v. 59, p. 5241-5247.

Pavich, M.J., Leo, G.W., Obermeier, S.F., and Estabrook, J.R., 1989, Investigations of the characteristics, origin, and residence time of the upland residual mantle of the Piedmont of Fairfax County, Virginia: U.S. Geological Survey Professional Paper 1352, 58 p.

Peacock, S.M., 1987, Serpentinization and infiltration metasomatism in the Trinity peridotite, Klamath province, northern California: Implications for subduction zones: Contributions to Mineralogy and Petrology, v. 95, p. 55-70.

Pokrovsky, O.S., and Schott, J., 2000, Kinetics and mechanism of forsterite dissolution at 25°C and pH from 1 to 12: Geochimica et Cosmochimica Acta, v. 64, p. 3313-3325.

Quick, J.E., 1981, The origin and significance of large, tabular dunite bodies in the Trinity peridotite, northern California: Contributions to Mineralogy and Petrology, v. 78, p. 413-422.

Rimstidt, J.D., Brantley, S.L., and Olsen, A.A., Systematic review of forsterite dissolution rate data: Geochimica et Cosmochimical Acta (in press).

Rosso, J.J., and Rimstidt, J.D., 2000, A high resolution study of forsterite dissolution rates: Geochimica et Cosmochimica Acta, v. 64, p. 797-811.

Sak, P.B., Fisher, D.M., Gardner, T.W., Murphy, K., and Brantley, S.L., 2004, Rates of weathering rind formation on a Costa Rican basalt: Geochimica et Cosmochimica Acta, v. 68, p. 1453-1472.

Santelli, C.M., Welch, S.A., Westrich, H.R., and Banfield, J.F., 2001, The effect of Fe-oxidizing bacteria on Fe-silicate mineral dissolution: Chemical Geology, v. 180, p. 99-115.

Schnoor, J.L., 1990, Kinetics of chemical weathering: A comparison of laboratory and field weathering rates, *in* Stumm, W., ed., Aquatic Chemical Kinetics. Wiley, New York, N.Y., p. 475-504.

Schott, J., and Berner, R.A., 1983, X-ray photoelectron studies of the mechanism of iron silicate dissolution during weathering: Geochimica et Cosmochimica Acta, v. 47, p. 2233-2240.

Schott, J., Berner, R.A., and Sjöberg, E.L., 1981, Mechanism of pyroxene and amphibole weathering—I. Experimental studies of iron-free minerals: Geochimica et Cosmochimica Acta, v. 45, p. 2123-2135.

Schwyn, B., and Neilands, J.B., 1987, Universal chemical assay for the detection and determination of siderophores: Analytical Biochemistry, v. 160, p. 47-56.

Shallari, S., Schwartz, C., Hasko, A., and Morel, J.L., 1998, Heavy metals in soils and plants of serpentine and industrial sites of Albania: The Science of the Total Environment, v. 209, p. 133-142.

Sharp, R.P., 1960, Pleistocene glaciation in the Trinity Alps of northern California: American Journal of Science, v. 258, p. 305-340.

Shepard, M.K., Arvidson, R.E., Caffee, M., Finkel, R., and Harris, L., 1995, Cosmogenic exposure ages of basalt flows: Lunar Crater volcanic field, Nevada: Geology, v. 23, p. 21-23.

Shopka, H.H., Derry, L.A., and Arcilla, C.A., 2011, Chemical weathering, river geochemistry and atmospheric carbon fluxes from volcanic and ultramafic regions on Luzon Island, the Philippines: Geochimica et Cosmochimica Acta, v. 75, p. 978-1002.

Siegel, D.I., and Pfannkuch, H.O., 1984, Silicate mineral dissolution at pH 4 and near standard temperature and pressure: Geochimica et Cosmochimica Acta, v. 48, p. 197-201.

Skinner, C.N., Taylor, A.H., and Agee, J.K., 2006, Klamath mountains bioregion, *in*: Van Wagtendonk, J.W., Shaffer, K.E., Fites-Kaufman, J., and Thode, A.E., eds., Fire in California's ecosystems: University of California Press, Berkeley, p. 170-194.

Spaulding, W.G., 1985, Vegetation and climates of the last 45,000 years in the vicinity of the Nevada Test Site, south-central Nevada: U.S. Geological Survey Professional Paper 1329, 83 p.

Stemmer, M., Gerzabek, M.H., and Kandeler, E., 1998, Organic matter and enzyme activity in particle-size fractions of soils obtained after low-energy sonication: Soil Biology and Biochemistry, v. 30, p. 9-17.

Stickney, E.K., 2004, The volcanology and petrogenesis of the northern Lunar Crater Volcanic Field, Nye County, Nevada [M.S. thesis]: University of Nevada, Las Vegas, 93 p.

Strauss, E.A., and Lamberti, G.A., 2002, Effect of dissolved organic carbon quality on microbial decomposition and nitrification rates in stream sediments: Freshwater Biology, v. 47, p. 65-74.

Sverdrup, H.U., 1990, The kinetics of base cation release due to chemical weathering: Lund University Press, 246 p.

Teir, S., Kuusik, R., Fogelholm, C.-J., and Zevenhoven, R., 2007a, Production of magnesium carbonates from serpentinite for long-term storage of CO_2: International Journal of Mineral Processing, v. 85, p. 1-15.

Teir, S., Revitzer, H., Eloneva, S., Fogelholm, C.-J., and Zevenhoven, R., 2007b, Dissolution of natural serpentinite in mineral and organic acids: International Journal of Mineral Processing, v. 83, p. 36-46.

Velbel, M.A., 1993, Constancy of silicate-mineral weathering-rate ratios between natural and experimental weathering: implications for hydrologic control of differences in absolute rates: Chemical Geology, v. 105, p. 89-99.

Velbel, M.A., 2009, Dissolution of olivine during natural weathering: Geochimica et Cosmochimica Acta, v. 73, p. 6098-6113.

Velbel, M.A., and Ranck, J.M., Etch pits on naturally altered olivine from dunites of the Appalachian Blue Ridge Mountains, North Carolina, USA: Mineralogical Magazine, v. 72, p. 145-148.

Wegner, W.W., and Ernst, W.G., 1983, Experimentally determined hydration and dehydration reaction rates in the system MgO-SiO_2-H_2O: American Journal of Science, v. 283, p. 151-180.

Weishaar, J.L., Aiken, G.R., Bergamaschi, B.A., Fram, M.S., Fujii, R., and Mopper, K., 2003, Evaluation of specific ultraviolet absorbance as an indicator of the chemical composition and reactivity of dissolved organic carbon: Environmental Science and Technology, v. 37, p. 4702-4708.

Welch, S.A., and Banfield, J.F., 2002, Modification of olivine surface morphology and reactivity by microbial activity during chemical weathering: Geochimica et Cosmochimica Acta, v. 66, p. 213-221.

White, A.F., 2002, Determining mineral weathering rates based on solid and solute weathering gradients and velocities: application to biotite weathering in saprolites: Chemical Geology, v. 190, p. 69-89.

White, A.F., and Brantley, S.L., 2003, The effect of time on the weathering of silicate minerals: why do weathering rates differ in the laboratory and field?: Chemical Geology, v. 202, p. 479-506.

Whitney, D.L., and Evans, B.W., 2010, Abbreviations for names of rock-forming minerals: American Mineralogist, v. 95, p. 185-187.

Wildman. W.E., Jackson, M.L., and Whittig, L.D., 1968, Iron-rich montmorillonite formation in soils derived from serpentinite: Soil Science Society of America Journal, v. 32, p. 787-794.

Wogelius, R.A., and Walther, J.V., 1991, Olivine dissolution at 25°C: effects of pH, CO_2, and organic acids: Geochimica et Cosmochimica Acta, v. 55, p. 943-954.

Wogelius, R.A., and Walther, J.V., 1992, Olivine dissolution kinetics at near-surface conditions: Chemical Geology, v. 97, p. 101-112.

Yardley, E., 2011, Enhancing the dissolution of lizardite with oxalate [M.S. thesis]: The University of Maine, 149 p.

VITA

Graduate College
University of Nevada, Las Vegas

Julie Lynn Baumeister

Degree:

Bachelor of Arts, Geology, 2009
University of Minnesota, Morris

Special Honors and Awards:

Second Place in the Science & Engineer Poster Session, UNLV Graduate & Professional Student Association Annual Research Forum, 2011
Bernada E. French Scholarship, 2010
Geological Society of Nevada Scholarship, 2010
UNLV Graduate & Professional Student Association Grant, 2010

Abstracts and Presentations:

Baumeister, J.L., Tu, V., Evert, M.H., Metcalf, R.V., Olsen, A.A., and Hausrath, E.M., 2011, Chemical weathering of serpentinite in the Klamath Mountains, California: Geological Society of America Abstracts with Programs, v. 43, no. 5, p. 63.

Evert, M.H., Baumeister, J.L., and Hausrath, E.M., 2011, Biological effects on serpentinite weathering: UNLV College of Sciences Undergraduate Research Opportunities Program Poster Session, Aug. 9, 2011, Las Vegas, Nevada.

Hausrath, E.M., Olsen, A.A., Baumeister, J.L., Tu, V., Yardley, E., 2011, Biogeochemical weathering of serpentine minerals from bedrock to soil: Critical Zone Observatory All Hands Meeting, Invited Keynote Talk, May 9, 2011, Tucson, Arizona.

Baumeister, J.L., Tu, V., Olsen, A.A., and Hausrath, E.M., 2011, Chemical weathering rates of olivine and serpentine in natural environments: UNLV Graduate College and Graduate & Professional Student Association Annual Research Forum, Mar. 26, 2011, Las Vegas, Nevada.

Tu, V., Baumeister, J., Metcalf, R., Olsen, A., and Hausrath, E., 2011, Serpentinite weathering with implications for Mars: 42nd Lunar and Planetary Science Conference, Abstract #2303, Mar. 7-11, 2011, The Woodlands, Texas.

Baumeister, J.L., Tu, V., Olsen, A.A., and Hausrath, E.M., 2010, Chemical weathering rates of olivine and serpentine in natural environments: Geological Society of America Abstracts with Programs, v. 42, no. 5, p. 83.

Tu, V., Baumeister, J., and Hausrath, E., 2010, Chemical weathering of serpentinite rocks and implications for atmospheric CO2 carbonation: UNLV College of Sciences Undergraduate Research Opportunities Program (UROP) Poster Session, p. 42, Aug. 3, 2010, Las Vegas, Nevada

Ameluxen, A.M., and Baumeister, J.L., 2008, The nature of Glacial River Warren flow: a study of the characteristics of boulders and bedrock in the Big Stone

National Wildlife Refuge, western Minnesota, to determine outlet flow rates: Geological Society of America Abstracts with Programs, v. 40, no. 5, p. 16.

Thesis Title:

Chemical Weathering of the Mafic Minerals Serpentine and Olivine in Natural Environments

Thesis Examination Committee:

Chairperson, Elisabeth Hausrath, Ph. D.
Committee Member, Rodney Metcalf, Ph. D.
Committee Member, Zhongbo Yu, Ph.D.
Graduate Faculty Representative, Brian Hedlund, Ph.D.